Thermal Equivalence Networks for Analysis of Transient Thermography

DISSERTATION

zur Erlangung des Grades eines Doktors

der Naturwissenschaften

vorgelegt von

Nils J. Ziegeler

eingereicht bei der Naturwissenschaftlich-Technischen Fakultät

der Universität Siegen

Siegen 2022

gedruckt auf alterungsbeständigem holz- und säurefreiem Papier

Betreuer und erster Gutachter

Prof. Dr. rer. nat. Stefan Schweizer

Universität Siegen

Zweiter Gutachter

Prof. Dr. rer. nat. Dr. h. c. Ullrich Pietsch

Universität Siegen

Tag der mündlichen Prüfung

11.07.2022

Contents

Abstract

In recent years, advances in high-speed infrared camera technology have opened up many new fields of application. One area which benefited greatly is the field of thermal testing. Increased sensitivity and faster sampling rates have opened a bridge to thermal testing techniques that could previously only be performed via electrical contacts or thermocouples. An example is the method network identification by deconvolution, which is investigated here. This work begins with an extensive collection of the mathematical theory, established practices as well as modern research results. Detailed descriptions of all procedures implemented in this work are given. To evaluate the established algorithms systematically, test series on theoretical thermal transients are conducted. Special measures of accuracy are developed to rate the performance of each method. Building on these results, a new method for network identification is presented, which is called optimization-based network identification. The method achieves a greatly enhanced accuracy and noise resistance. Tests on thermal transient measurement data confirm these findings by improving established analysis techniques such as the transient dual interface method. The combination of network identification and infrared thermography resulted in the invention of a new non-destructive testing technique, which was patented as a result. The work concludes with three application examples using this thermographic network identification.

Zusammenfassung

In den letzten Jahren haben technologische Fortschritte bei Hochgeschwindigkeits-Infrarotkameras zahlreiche neue Anwendungsbereiche eröffnet. Ein Bereich, der stark davon profitiert hat, ist die experimentelle thermische Analyse. Höhere Messgenauigkeiten und schnellere Abtastraten ermöglichen neuartige thermische Prüftechniken, die vorher nur mit Hilfe von elektrischen Kontakten oder Thermoelementen möglich waren. Ein Beispiel hierfür ist die Methode der Netzwerkidentifizierung durch Entfaltung. Diese Arbeit beginnt mit einem umfassenden Überblick über den mathematischen Hintergrund, etablierte Algorithmen sowie neuste Forschungsergebnisse. Alle in dieser Arbeit implementierten Verfahren werden detailliert beschrieben. Um die verwendeten Algorithmen systematisch zu bewerten, werden Testreihen auf Grundlage theoretischer thermischer Transienten durchgeführt. Es werden spezielle Genauigkeitsmaße entwickelt, um die Leistungsfähigkeit der einzelnen Verfahren objektiv zu bewerten. Basierend auf diesen Analysen wird eine neue Methode zur Netzwerkidentifikation entwickelt, die als optimierungsbasierte Netzwerkidentifikation bezeichnet wird. Die Methode erreicht eine stark verbesserte Genauigkeit und Rauschresistenz. Tests an thermischen transienten Messdaten bestätigen diese Erkenntnis, indem sie etablierte Analysetechniken wie die transiente Dual-Interface-Methode verbessern. Die Kombination von Netzwerkidentifikation und Infrarot-Thermografie führte zur Erfindung einer neuen zerstörungsfreien Prüftechnik, die in der Folge patentiert wurde. Die Arbeit schließt mit drei Anwendungsbeispielen, die die Möglichkeiten der thermografischen Netzwerkidentifikation aufzeigen.

Introduction

To be successful in the international market for electronic components, many companies strive to have cheaper, faster or more reliable products than their competitors. In addition, a growing awareness of global systemic crises is pushing companies to respect the Sustainable Development Goals set by the United Nations, for example by making their products sustainable and recyclable [1, 2]. While these goals are not necessarily in conflict, they can push and pull the development process in many directions at once. When new designs, processes and suppliers are constantly being introduced, things occasionally go wrong. One case that attracted a lot of attention in the media were the burning batteries in Samsung Galaxy Note 7 smartphones in 2016 [3, 4]. Not only do such accidents pose a major safety risk to consumers, but they are also extremely damaging to a company's reputation, both among consumers and industry partners. Highly qualified personnel, well-organized procedures, and a receptive mistake culture can help prevent these incidents.

A well-developed inspection scheme will identify problems ahead of time, saving both time and money. As part of a production process, quality assurance inspection can be conducted. This involves examining a fully or partially manufactured product to determine whether it conforms to a list of predefined specifications. In the case of a printed circuit board (PCB), for instance, this means confirming that the electronic layout is correct or looking for external signs of damage. In the easiest case, this is done via manual visual inspection. Once a system is in operation, maintenance inspections are performed. They aim to extend the uptime of a system, monitor its status, and prevent total breakdowns. As an example, in large photovoltaic systems, a short circuit in a single module is efficiently detected by infrared imaging [5]. In the development phase, accelerated life tests are a valuable tool to detect long-term problems at an early stage [6]. For these tests, devices are subjected to extreme conditions that artificially accelerate degradation processes. A detailed failure mode analysis helps to develop a precise knowledge of the physical processes involved and enables better engineering decisions to be made. By combining all of these concepts, a high level of reliability can be achieved.

The development of modern printed circuit boards is a complex process. Typically, the assembly includes subcomponents from many manufacturers. It is the responsibility of the thermal system designer to manage the temperature and power specifications of each of these components. As part of this process, one must choose a suitable layout, account for component interactions and decide on a cooling strategy. Before thermal management became a prominent issue, detailed information about the thermal properties of each component was not widely available. In the simplest case, only a single thermal resistance is

specified for an electronic component, for example an integrated circuit package. With only limited data available, much of the design process relies on previous experience gained through trial and error. Over time, it became clear that more detailed information was needed to improve quality and reliability while reducing overly cautious safety margins. In light of these challenges, joint research projects were launched that led to the development of extensive industry standards, as is discussed later in this work.

As a part of a modern thermal design processes, computer simulations are indispensable for electronic components. In complex finite element models (FEM), a component is simulated with the highest possible level of detail. The goal of a multiphysics simulation is to combine all relevant physical aspects in a single simulation, revealing their interdependencies. In this way, the design is optimized without the need for physical prototypes. Thermal simulations often involve coupled heat conduction and fluid flow simulations to obtain steady-state or transient temperature distributions. In addition, thermally coupled phenomena such as the mechanical behavior or the radiative properties are investigated.

To verify the result of a thermal simulation, measurements are required, which are carried out on first prototypes. In other cases, it might be impossible or infeasible to perform accurate simulations, for example if material parameters are unknown. For isolated components, transient thermal tests are a suitable approach. To perform such a test, the method of network identification by deconvolution is discussed in this work. The method provides a direct solution to one-dimensional heat conduction problems given the transient thermal behavior. As a result, the thermal parameters along the entire heat path are recovered. The values of the thermal resistances and capacities are captured by the thermal structure function, which is the end result of network identification by deconvolution.

In practice, thermal structure functions help the designer by providing thermal models without the need to perform detailed simulations. Examples of tasks that are hard to analyze solely via simulations include the testing of new material compositions or the tuning of process parameters in a production process. In combination with detailed simulations, features of thermal structure functions can be attributed to specific elements of a device. In this way, they can help with failure analysis and provide additional insight during the design process. As these thermal models belong to specific devices, they can also serve as part of a quality inspection scheme. Routinely performed transient thermal testing in combination with detailed simulations allows to detect and to categorize irregularities in the thermal behavior of each device. When providing thermal structure functions as part of the data-sheet, detailed information about the thermal behavior of a device can be communicated without disclosing its inner structure.

The goal of this work is to analyze the potential of network identification by deconvolution when conducted via infrared thermography. In addition, this work aims to contribute to thermal analysis using thermal structure functions in general. This includes the algorithms and methodology of network identification by deconvolution as well as its experimental application. To this end, it is necessary

to first gather a comprehensive overview of the mathematical theory, established practices as well as modern research results of network identification and thermal structure functions. No similar compendium is available currently. In particular, the aim of this work is to investigate, which are the most suitable algorithms for network identification by deconvolution. Such systematic analysis has not been conducted yet. The limits of accuracy of established algorithms are explored as well as the possibilities for new approaches to compute structure functions. Tests are conducted using theoretical test cases as well as real-world examples. Building on this, the work strives to expand the field of application for transient thermal analysis using network identification. For this, infrared thermography is a promising candidate as it offers contactless temperature measurements with spatial resolution and high sensitivity. The potential of thermographic network identification as a non-destructive testing technique is explored and discussed in comparison to other non-destructive testing techniques. The ultimate goal is to develop a contactless test procedure for the thermal performance of a device under test employing the thermographic network identification. The merit of such a system is that the analysis is based on the thermal resistances and capacitances of the heat path, which are the fundamental quantities when evaluating thermal performance.

For network identification by deconvolution, a wide range of recommended algorithms exist in the literature. The actual deconvolution is often performed using Fourier or Bayesian deconvolution. When using Fourier deconvolution, several different window functions are recommended such as the Fermi-Dirac [7] or the Gaussian window [8]. However, no specific motivation for these filters is given and no systematic evaluation of their performance is conducted. For Bayesian deconvolution, a common recommendation is to use 1000 steps [9], which is generally followed [10]. Pareek *et al.* [11] analyzes Bayesian iteration with a higher number of steps, but concludes that 1000 to 2000 is well suited for experimental data. While these results indicate that Bayesian deconvolution is better than Fourier deconvolution, the conclusion is not based on thorough investigation and quantitative criteria.

The reason that these recommendations for algorithmic parameters have an anecdotic character is that no procedure for systematic evaluation has been recommended prior to this work. Closest to such a procedure is a well-known work by Szalai and Székely [12]. There, the concept of a practical maximum tolerance is introduced. It is defined as a maximum allowed relative deviation from the ideal result. Algorithms are gauged based on whether they conform to this test. While this approach allows a classification of different algorithms and implementations, it is not sufficient to perform a systematic comparison between candidates and to work on their continued refinement. Therefore, in this work several measures of accuracy are developed. Together with a set of test structures and test conditions they provide a standardized performance criterion. Based on this methodology, the questions raised above about optimal parameters and implementations are visited anew in this work.

Given a well-performing algorithm, the network identification can be applied to thermographic measurement data for non-destructive testing. Other approaches

in non-destructive testing such as the thermographic signal reconstruction set a high bar in terms of sensitivity towards defect recognition. Nevertheless, these techniques have several shortcomings, where the thermographic network identification has the potential to find a niche and surpass them. A network identification by deconvolution follows a well-documented procedure and is based on an extensive theoretical background. With the right experimental setup, well-defined thermal resistances and thermal capacitances are obtained, which directly describe the structure of the sample. In addition, the time-resolved behavior is available via the time constant spectrum. Other non-destructive testing techniques are often only qualitative in nature or are based on artificial parameters. An example of this is the popular method of thermographic signal reconstruction, which uses images of fitting coefficients of polynomials for defect recognition [13]. This leaves much room for interpretation as to how exactly the fitting should be conducted. As a consequence, a range of different recommendation exist, for example for the degree of the polynomial [14, 15, 16]. As a consequence, thermographic signal reconstruction involves at least a certain amount of trial and error to find a suitable coefficient and polynomial degree. Based on these observations, the potential of the thermographic network identification is explored in this work.

The work is divided into three chapters. In Chapter 1, a complete description of the mathematical-physical formalism necessary to understand the method of network identification by deconvolution is compiled. Currently, a similarly comprehensive theoretical treatise on this topic cannot be found in the literature. After an introduction to heat conduction phenomena, the modeling of thermal systems via the lumped system approximation is covered. For the case of the electronics industry, it is shown how thermal equivalence circuits are constructed using the electro-thermal analogy. To describe one-dimensional heat conduction phenomena, the Foster- and Cauer-type RC ladders are introduced. A system theoretic description of these circuits is developed using the transfer function. Then, the formalism is applied to thermal response measurements, from where the method of network identification by deconvolution is derived. A brief history of network identification by deconvolution follows together with an overview of current research topics in the field is given. Finally, all steps of the algorithm are explained in detail and variations of their implementation are compiled as described in the literature.

Chapter 2 analyses the performance of these algorithms based on specifically developed test cases and introduces improvements based on this analysis. The chapter starts with a detailed explanation of the implementations developed as a part of this work. Then, a new network identification method called "optimization-based network identification" is presented, which is superior to conventional network identification by deconvolution methods in terms of accuracy and noise susceptibility. Subsequently, a procedure specifically developed to evaluate the accuracy of network identification results is presented. The goal is to measure the accuracy of the different variants as objectively and accurately as possible. Using these measures of accuracy, the methods are optimized to achieve their best possible performance. All methods, including

the implementations reported in the literature, the implementations developed for this work, as well as the newly developed optimization-based network identification are evaluated on various test cases. Then, an extensive analysis of the accuracy of the results obtained is conducted.

In Chapter 3, network identification is applied to infrared thermographic transient measurements. The chapter begins with an overview of non-destructive testing techniques as reported in the literature. Then, a newly developed and patented non-destructive testing technique named "thermographic network identification" is introduced [17]. First, its accurate experimental realization using infrared thermographic measurements is verified. Then, the performance of network identification by deconvolution as well as the newly developed optimization-based network identification is compared on the example of transient thermographic measurements on LEDs. The chapter is concluded with three examples of increasing complexity which demonstrate the capabilities of thermographic network identification as a non-destructive testing technique. The thesis ends with a conclusion and a brief outlook.

Chapter 1

Theoretical background

1.1 Heat conduction

In this chapter, the physics of heat conduction are developed. Starting from fundamental equations a discretized description is derived, which is suitable for digital calculations.

1.1.1 Basics of heat conduction

Consider a closed homogeneous thermodynamic system, such as a metal block. Its temperature is defined by the average kinetic energy of its microscopic degrees of freedom. If it is in internal thermodynamic equilibrium, its temperature is constant throughout the system. A dynamic is induced when two such systems with different temperatures come in thermal contact with each other. They will exchange energy until equilibrium is reached once again.

Fundamentally, there are three mechanisms by which the metal blocks could exchange energy. These are radiation, convection, and conduction. Radiative transfer involves the exchange of heat via electromagnetic radiation. Photons are emitted and absorbed by most objects, as described by the Stefan-Boltzmann law. This effect is strongly temperature-dependent due to its T^4-scaling and typically not dominant at room temperature. Nevertheless, if given enough time, the two systems would reach thermal equilibrium by radiation exchange alone.

If the two metal blocks were surrounded by a third medium, for example water, they could exchange energy via a convective process. In this case, the heat is transported to and through the water. Conduction is also possible. Changes in water temperature in the vicinity of the metal blocks lead to fluid flow, which forms an additional contribution to the heat transport. This process is called advection. Convective heat transfer thus consists of two parts, a diffusive and an advective part.

When they are in direct contact, molecular vibrations, the phonons, can propagate directly from block to block. Heat conduction is a purely diffusive process and analyzed in detail below. The following calculations are based on David W. Hahn and M. Necati Özişik, "Heat Conduction" [18]. Fourier's law of heat conduction states that a spatially inhomogeneous temperature field, $T(x,t)$, induces a heat flow, $q(x,t)$, per unit time and per unit area such that the temperature gradient is opposed. The magnitude of the heat flow is determined

by the temperature gradient, $\nabla T(x,t)$, and the thermal conductivity, k,

$$q(x,t) = -k \, \nabla T(x,t) \, . \tag{1.1}$$

Here, a dependence on x stands short for all three spatial coordinates. In general, the thermal conductivity, k, can also have a spatial dependence, $k = k(x)$, which is not explicitly noted here. When the amount of energy, $U(x,t)$, in a small volume, dV, changes, it can either flow into the volume at a certain rate $\delta\dot{Q}$, flow out of it, or be generated in it at a rate $\delta\dot{E}_{\text{gen}}$, for example in the form of Joule heating. Additionally, it could perform work, $\delta\dot{W}$, at a certain rate. Together this leads to a conservation of energy in the form

$$\delta\dot{Q} + \delta\dot{E}_{\text{gen}} - \delta\dot{W} = \frac{dU(x,t)}{dt} \, . \tag{1.2}$$

The heat flow, $\delta\dot{Q}$, in and out of this volume is the sum of the heat flows in the three coordinate directions, $\delta\dot{Q} = \delta\dot{Q}_x + \delta\dot{Q}_y + \delta\dot{Q}_z$. In the following, only the x-component is treated. The y- and z-components follow analogously. To derive from this the general heat equation, the differential, $\delta\dot{Q}_x$, is expressed as the local heat flow difference.

$$\delta\dot{Q}_x = q_x(x,t) - q_x(x + dx,t) \tag{1.3a}$$

The second term in (1.3a) is expanded in a Taylor series to first order. Then, (1.1) is applied to the third term in (1.3b).

$$\delta\dot{Q}_x = q_x(x,t) - q_x(x,t) - \frac{\partial q_x(x,t)}{\partial x} \, dx \tag{1.3b}$$

$$= \frac{\partial}{\partial x} \left(k \frac{\partial T(x,t)}{\partial x} \right) dV \tag{1.3c}$$

The local rate of energy generation, $\delta\dot{E}_{\text{gen}}$, is expressed via its density, $g(x,t)$,

$$\delta\dot{E}_{\text{gen}} = g(x,t) \, dV \, . \tag{1.4}$$

In addition, it is assumed that no work is performed by the system, i. e. $\delta\dot{W} = 0$. If the total kinetic and potential energy content of the volume dV does not change and mass flow across the boundary is negligible, the energy of the system, $U(x,t)$, has the form

$$U(x,t) = u(x,t) \, \rho \, dV \, , \tag{1.5}$$

where ρ denotes the mass density and $u(x,t)$ is an energy density (per mass). Using the constant volume specific heat capacity, c, the energy density is expressed via the temperature field $u(x,t) = c \cdot T(x,t)$,

$$\frac{\partial U(x,t)}{\partial t} = \rho \cdot c \, \frac{\partial T(x,t)}{\partial t} \, dV \, . \tag{1.6}$$

Combining all the above transformations yields the general heat equation,

$$\nabla \cdot \big(k\, \nabla T(x,t) \big) - \rho \cdot c\, \frac{\partial T(x,t)}{\partial t} = -g(x,t)\,. \tag{1.7}$$

1.1.2 Lumped system approximation

To solve a heat diffusion problem, one way is to analytically or numerically solve the heat equation with appropriate initial and boundary conditions. For complex problems, a formulation using partial differential equations is often very difficult or impossible. Similarly, for very simple problems, stating and solving a differential equation is too time-consuming.

One possible solution, using the above notation, is to keep the small volume, dV, finite. Each of the volumes, also called "lumps", is assigned a temperature and a thermal capacity. The thermal capacity, C_{th}, of the lump is the integrated thermal capacity in the volume, while the temperature belonging to the lump is defined as the average temperature, $\overline{T}$, within the volume.

The accuracy of the approximation depends on the nature of the thermal system and the size of the lump. For practical purposes, it is reasonable to make the lumps as large as possible while maintaining a minimum accuracy of the approximation. However, this requires a measure of the quality of the approximation. The Biot number answers this need [19].

$$\text{Bi} = \frac{h\,\delta}{k} = \frac{\delta/k}{1/h} \tag{1.8}$$

Here, h is the heat transfer coefficient, which is a measure for the ease of heat transfer over system boundaries. The characteristic length of the volume, δ, is dependent on the shape of the element and k is the thermal conductivity. Intuitively, the Biot number is best understood as the ratio of internal resistance against heat flow, δ/k, to the resistance against heat flow over the system boundaries, $1/h$. Thus, the Biot number is a dimensionless quantity and in principle different for each element.

For small values of the Biot number, $\text{Bi} \ll 1$, the lumped system approximation is justified. In this case, temperature deviations, σ, within the lump are small and because of that the average temperature, $\overline{T}$, is a good representation of the true distribution. As a guideline, the following rule is widely used [19]. For Biot numbers $\text{Bi} \leq 0.1$, the relative temperature deviation is $\sigma/\overline{T} \leq 5\%$. If the Biot number for a system is too large, for example because temperature variations within the element are too high, a possible solution is to choose a smaller volume. This will reduce the Biot number, because it is proportional to the characteristic system length, δ.

On the other hand, it is more difficult to argue which thermal resistance, R_{th}, should be assigned between the elements such that it has a well-defined meaning and a clear physical representation. The following definition seems intuitive. When a steady state heat flow, $\dot{Q}$, passes over a boundary from one volume to another it encounters a temperature drop, ΔT, that arises due to the different average temperatures in the two volumes. Consequently, the thermal resistance should be

$$R_{\text{th}} = \frac{\Delta T}{\dot{Q}}\,. \tag{1.9}$$

However, there are some issues with this definition that make it difficult to apply in practice. It must be ensured that no heat flows through other surfaces of the element. Otherwise, the exact amounts of energy flowing through each surface have to be known. Alternatively, Rosten and Lasance argue for the following definition [20]:

> *The temperature difference between two isothermal surfaces divided by the heat that flows between them is the thermal resistance of the materials enclosed between the two isothermal surfaces and the heat flux tube originating and ending on the boundaries of the two isothermal surfaces.*

In any case, using the above definitions it is possible to construct a lumped thermal system. Each lump has a temperature, a thermal capacity, and a thermal resistance to neighboring elements. The constructed networks are similar to electrical networks in the sense shown in Table 1.1. Using thermal equivalence networks opens up the possibility to apply theorems and techniques from electrical engineering to thermal analysis.

Table 1.1: *Equivalent quantities in the electro-thermal analogy*

Thermal Quantity		Electric Quantity	
T	temperature	P	potential
ΔT	temperature difference	V	voltage
R_{th}	thermal resistance	R	electrical resistance
C_{th}	thermal capacity	C	electrical capacity
$\dot{Q}$	heat transfer rate	I	current

It has to be kept in mind that due to the underlying physics, the lumped element approximation is a better model for electric circuits than for thermal systems. An extensive discussion of the issue and its implications in practice are given in [21]. In summary, the systematic difference lies in the fact that a true one-dimensional heat flow in thermal systems is very difficult to achieve. This is because electrical conductivities span a much wider range than thermal conductivities. Practically, there are no true thermal isolators. Consequently, lumped thermal models have to be constructed and analyzed with much care.

1.1.3 Modeling thermal systems

In the electronics industry, modeling of thermal systems has become common in the last decades. Today, thermal management is an essential aspect in the development of semiconductor components and gains further importance with increasing power densities in modern devices. Historically, the groundwork for present-day thermal modeling was laid with three major European projects. The findings of the DELPHI, SEED and PROFIT projects, which started in 1993, 1996 and 2000 respectively [20, 22], are summarized in the following. They

are complemented by more recent results, which extend the range of commonly applied techniques and make them more sophisticated. The combined efforts are standardized by the Joint Electron Device Engineering Council (JEDEC) [23, 24]. Today, thermal management has become an established field of research.

The following brief overview of the development of thermal modeling in the electronic industry is based on [21]. For a long time, the cooling performance of electronic components has only been characterized by a single parameter such as the steady-state junction-to-ambient resistance. Over time, however, it became apparent that more detailed information is required for conclusive product documentation and more accurate temperature predictions. Therefore, the simple one-resistor model has been extended to a resistor network, which is able to represent more complex relationships. These type of models are called compact thermal models and typically contain on the order of ten resistors.

While steady-state junction-to-ambient resistances can readily be obtained by measuring the respective temperatures, compact thermal models are derived from detailed finite element method (FEM) models. Such simulations allow access to the temperature distribution and heat flows within the device. One way to obtain a compact thermal model is to optimize its thermal resistances in such a way that specific temperature match the FEM model as close as possible. In this process, the nodes that make up the thermal network are defined first. Then, the values of the resistances between them are numerically optimized using an objective function that ensures an accurate prediction of the (junction) temperature. In this way, the enormous amount of elements and temperatures that make up an FEM model is reduced to a small number.

In practice, however, the application of this method encounters some difficulties. In a typical IC package, for example, the main heat paths are the leadframe, the direct contact with the board, and convection cooling at the top of the package. Depending on the environmental conditions, either natural or forced convection, the relative contributions of the different heat paths change and with it the junction temperature. When developing a compact thermal model, great care must be taken to determine which boundary conditions should be used in the detailed model. To combat this issue, the notion of a boundary condition independence is introduced. The idea is to use a wide variety of boundary conditions when optimizing the compact thermal model. The resulting resistances should have only little to no dependence on the boundary conditions imposed, making the compact model boundary condition independent.

All networks presented above are purely resistive and therefore describe only steady-state temperatures. However, there are many reasons to include the time-dependent behavior. One process that cannot be covered by a purely static analysis and which has a massive impact on the lifetime of a device is thermo-mechanical fatigue. It is caused by different thermal expansion coefficients at contact points that are exposed to repeated temperature changes. For example, solder joints are typically affected by this process. If a thermal designer has data available describing the time-resolved behavior of a component, it is possible to make an informed design decision in this context in an attempt to minimize the effects of thermal cycling. Dynamic thermal properties also affect the

interactions between components at the system level, which are particularly important at higher component densities. The development of dynamic compact thermal models was one of the goals of the PROFIT project. One way to generate dynamic models is to retrofit an existing stationary model with capacities so that it matches the transient behavior of a detailed model.

Modern techniques are no longer based on objective function-based optimization. Instead, in state-of-the-art dynamic compact thermal model generation, the large number of degrees of freedom that comprise the detailed model is iteratively reduced in model order reduction techniques. They do not rely on a predefined network to model the junction temperature, but instead coarsen the entire finite element simulation while maintaining a predefined accuracy [25]. The resulting dynamic thermal models typically have on the order of a few hundred nodes, depending on the complexity of the detailed model. Model order reduction has become an established procedure and several tools have been developed for commercial application [26, 27, 28]. The resulting thermal equivalent networks are integrated into circuit solvers such as SPICE or coupled into multiphysics simulations to achieve substantial time savings.

Sophisticated thermal modeling is not only of interest for applications in the electronics industry. There are many scientific and engineering applications that make use of thermal models, resulting in a multitude of different approaches and applications. In geothermal engineering, Pasquier and Marcotte used a lumped thermal model to describe the heat flow dynamics of a borehole heat exchanger [29, 30]. The lumped thermal model they developed is shown in Figure 1.1. The model is used to predict and analyze the temperature behavior of the heat carrier fluid during exploration, setup, and operation. Most notably, the properties of the soil surrounding the borehole and its interaction with the heat exchanger are captured. The values of thermal resistances and heat capacities in the heat exchanger model are manually determined based on experience and using established analytical equations. Once a model of the heat exchanger is developed, several methods are available to evaluate the measurement data [31, 32]. To solve the lumped thermal model for the heat exchanger shown in Figure 1.1, linear time-invariant system theory is applied.

From a theoretical perspective, one-dimensional systems are well understood. They describe a point heat source from which heat is conducted via a single heat path to a heat sink. It is possible to solve these systems both forwards and backwards. If the parameters of the heat path and a thermal load are given, the temperatures along the heat path are available analytically. Alternatively, if the temperature response and the associated thermal load are known, it is possible to reconstruct the thermal conductivities and heat capacities along the heat path. For this reason, this kind of system description is attractive. Possible applications are, for instance, the thermal design of heat paths for LEDs or other isolated electronic components. Regardless of application, great care must be taken to ensure that the assumption of a one-dimensional heat flow is not violated too much. The nature of heat conduction makes it difficult to achieve well-defined one-dimensional heat paths.
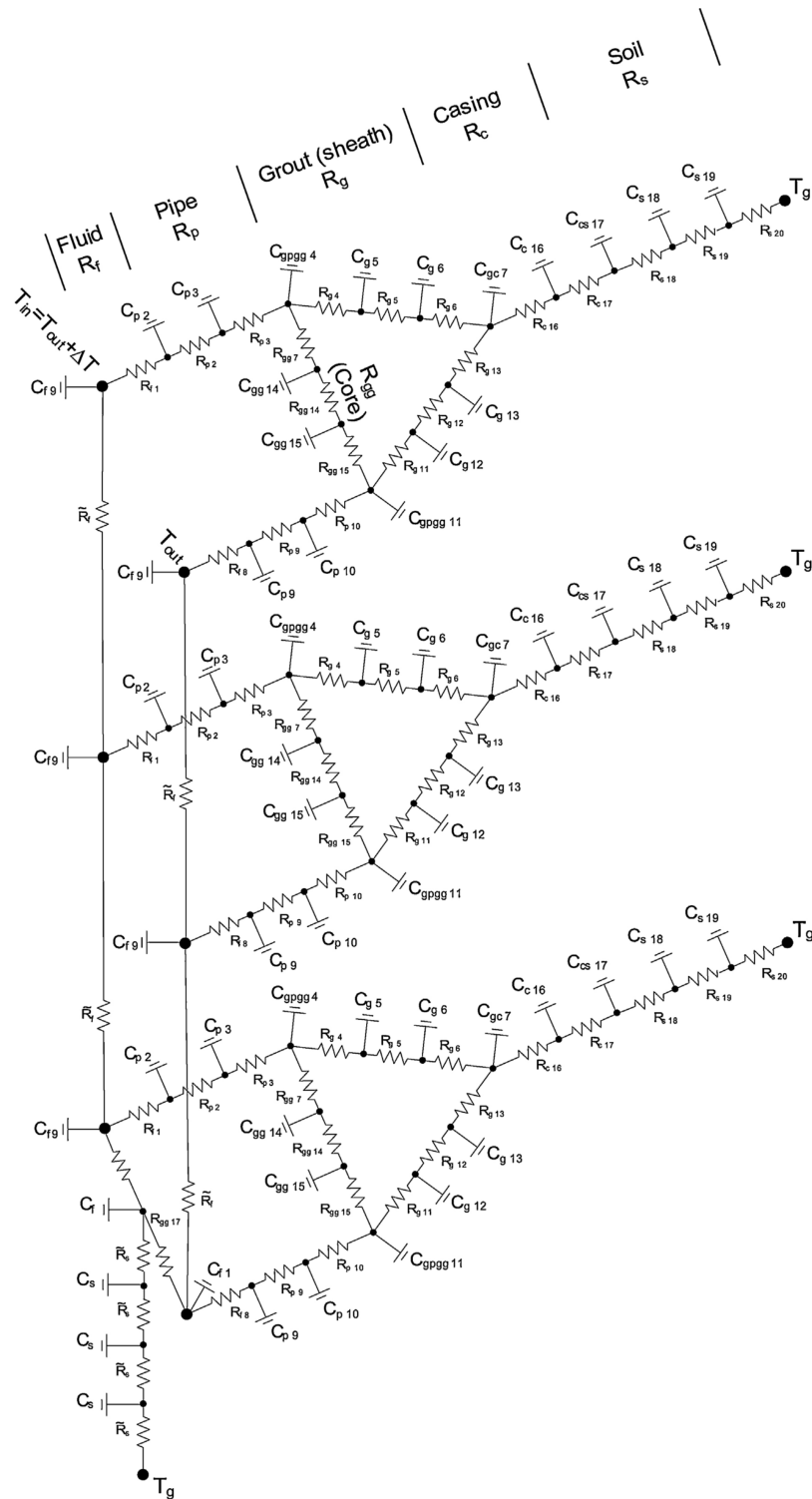
Figure 1.1: *Example of a thermal resistance and capacitance model for a borehole heat exchanger. Reprinted from "Joint use of quasi-3D response model and spectral method to simulate borehole heat exchanger", Philippe Pasquier and Denis Marcotte, Geothermics, Volume 51, pp. 281-299, Copyright (2014), with permission from Elsevier.*

1.2 System descriptions

1.2.1 Linear time-invariant systems

Even without detailed information about the inner workings of a system, it can be modeled as a black box and the effect of the system described solely by the relationship between input and output. In this context, the term *system* is quite general and can include anything that can be interacted with and has a specific response depending on the input. In the context of this work, system theory is used to solve the heat equation using a lumped element approach. Therefore, it suffices to imagine the systems discussed here as thermal models with lumped elements or equivalent electrical circuits. For the analysis of such systems, it is sufficient to restrict oneself to linear time-invariant systems. A powerful set of analytical descriptions is available for these systems. A comprehensive overview of system theory is found in [33, 34].

The effect of a system, $\mathcal{S}$, that takes $x(t)$ as an input function and produces an output, $y(t)$, is formalized as

$$y(t) = \mathcal{S}[x(t)] . \tag{1.10}$$

Linearity means that if $y_1(t) = \mathcal{S}[x_1(t)]$ and $y_2(t) = \mathcal{S}[x_2(t)]$ are two reactions of the system, then $y(t) = ay_1(t) + by_2(t) = \mathcal{S}[ax_1(t) + bx_2(t)]$ is also a reaction of the system. Time invariance, on the other hand, implies that the properties of the system do not change over time and the same reaction is observed at a later time, $y(t + T) = \mathcal{S}[x(t + T)]$.

For linear time-invariant systems, the effect of $\mathcal{S}$ is described as a convolution of the input with a function called the impulse response, $h(t)$,

$$y(t) = (x * h)(t) := \int_{-\infty}^{\infty} x(t - t') \cdot h(t') \, dt' . \tag{1.11}$$

The impulse response is defined as the system response to the idealized delta input $x(t) = \delta(t)$,

$$\mathcal{S}[\delta(t)] = (\delta * h)(t) = \int_{-\infty}^{\infty} \delta(t - t') \cdot h(t') \, dt' = h(t) . \tag{1.12}$$

In practice, it might be easier to provide a step function as input to the system instead of a delta function. For this case, the step response, $a(t)$, is defined as the reaction of the system to an input in the form of a Heavyside function, $x(t) = \Theta(t)$,

$$\mathcal{S}[\Theta(t)] = (\Theta * h)(t) = \int_{-\infty}^{\infty} \Theta(t - t') \cdot h(t') \, dt' = a(t) . \tag{1.13}$$

Analogous to the relationship between the Heavyside and delta functions, the impulse response, $h(t)$, and the step response, $a(t)$, are connected via a derivative,

$$h(t) = \frac{\mathrm{d}}{\mathrm{d}t} a(t) \,. \tag{1.14}$$

Since it is possible to express convolutions as multiplication by means of the Laplace transform, $\mathcal{L}$, linear time-invariant systems are usually considered in the Laplace domain. The impulse response corresponds to the transfer function, $H(s)$, which is defined as

$$H(s) = \mathcal{L}[h(t)](s) = \int_0^\infty h(t)\, \mathrm{e}^{-st}\, \mathrm{d}t \,. \tag{1.15}$$

In the same way, the input function, $X(s) = \mathcal{L}[x(t)](s)$, and the output function, $Y(s) = \mathcal{L}[y(t)](s)$, are converted to the Laplace domain. This allows to restate the convolution as

$$Y(s) = X(s) \cdot H(s) \,. \tag{1.16}$$

In the Laplace domain, functions are defined on the s-plane of the complex frequency, s. This is a generalization of the real-valued frequency, ω, which is commonly found in descriptions of periodic behavior. To describe arbitrary functions, the complex frequency is defined as

$$s = \sigma + \mathrm{i}\omega \,, \tag{1.17}$$

where ω reappears as the imaginary part. The real part, σ, is used to express non-periodic behavior such as damping.

In general, any system whose dynamics obey a linear differential equation with constant coefficients represents a linear time-invariant system. In addition, any system of ordinary differential equations of first order is equivalent to an ordinary differential equation of higher order and consequently also equivalent to a linear time-invariant system. To see the relation between differential equations and the transfer function, a system of the type (1.18) is considered. A comprehensive treatment of such systems is found in [35].

$$\sum_{i=0}^N a_i \frac{\mathrm{d}^i y}{\mathrm{d}t^i} = \sum_{i=0}^M b_i \frac{\mathrm{d}^i x}{\mathrm{d}t^i} \tag{1.18}$$

For real physical systems, $N > M$ must hold. Initial conditions for the derivatives of the output function, $y_0^{(k)}$, and the input function, $x_0^{(l)}$, are accounted for in the form

$$\left.\frac{\mathrm{d}^k y}{\mathrm{d}t^k}\right|_{t=0} = y_0^{(k)} \quad \text{and} \quad \left.\frac{\mathrm{d}^l x}{\mathrm{d}t^l}\right|_{t=0} = x_0^{(l)} \quad \text{for} \quad \begin{matrix} k = 0,\, 1,\, \ldots,\, N-1 \\ l = 0,\, 1,\, \ldots,\, M-1 \end{matrix}\,. \tag{1.19}$$

In this most general case, the solution has the form (1.20) [35]. By comparison with (1.16), the term in the first brackets in (1.20) is identified as $H(s)$. Consequently, (1.16) is only accurate when all initial conditions are equal to zero. If

the initial conditions are non-zero, the terms in the second bracket have to be added to receive the correct response.

$$Y(s) = \left[\frac{\displaystyle\sum_{i=0}^{M} b_i s^i}{\displaystyle\sum_{i=0}^{N} a_i s^i} \right] X(s) + \left[\frac{\displaystyle\sum_{i=0}^{N}\sum_{k=0}^{i-1} a_i s^{i-1-k} y_0^{(k)}}{\displaystyle\sum_{i=0}^{N} a_i s^i} - \frac{\displaystyle\sum_{i=0}^{M}\sum_{l=0}^{i-1} b_i s^{i-1-l} x_0^{(l)}}{\displaystyle\sum_{i=0}^{N} a_i s^i} \right] \tag{1.20}$$

Either way, the transfer function of such a linear differential equation with constant coefficients, or an equivalent linear time-invariant system, is represented by a rational function. The numerator polynomial, $N(s)$, has the order M and the denominator polynomial, $D(s)$, has the order N.

$$H(s) = \frac{N(s)}{D(s)} = \frac{\displaystyle\sum_{i=0}^{M} b_i s^i}{\displaystyle\sum_{i=0}^{N} a_i s^i} = \frac{b_0 + b_1 s + \ldots + b_{N-1} s^{N-1} + b_M s^M}{a_0 + a_1 s + \ldots + a_{N-1} s^{N-1} + a_N s^N} \tag{1.21}$$

Alternatively, the polynomials $N(s)$ and $D(s)$ are factorized according to the poles, $\sigma_{p,i}$, and zeros, $\sigma_{z,i}$ of the transfer function,

$$H(s) = \frac{N(s)}{D(s)} = k \cdot \frac{\displaystyle\prod_{i=1}^{M}(s - \sigma_{z,i})}{\displaystyle\prod_{i=1}^{N}(s - \sigma_{p,i})} . \tag{1.22}$$

Here, a common factor, k, has been extracted from the fraction. In an electronic context, it is interpreted as an amplifier gain. Among other things, the poles and zeros of the transfer function provide information about the stability of the system.

For translation back into the time domain, the inverse Laplace transform, $\mathcal{L}^{-1}$, is calculated by solving the curve integral in (1.23). The integration path in the complex plane runs parallel to the imaginary axis shifted by a constant γ, which must be chosen larger than the largest real part of all poles of the transfer function.

$$h(t) = \mathcal{L}^{-1}[H(s)](t) = \frac{1}{2\pi i} \int_{\gamma - i\infty}^{\gamma + i\infty} H(s)\, e^{st}\, ds \tag{1.23}$$

In practice, inverse Laplace transformations are usually calculated using transformation tables or using the residue theorem.

1.2.2 Two-port networks

Two-port networks are circuit elements that have four terminals which meet the port condition pairwise. The latter requires that the current, I_i, flowing into one terminal and out of the other is the same. The voltages measured at the ports 1 and 2 are denoted V_1 and V_2 respectively, as shown in Figure 1.2.

Figure 1.2: *Representation of a system, $\mathcal{S}$, as a two-port network with port voltages V_1 and V_2*

While the inner workings of a two-port network can be arbitrarily complex, it can also be of elementary simplicity and contain only a single electronic component. For the description of a thermal equivalent circuit, as exemplarily shown in Figure 1.1, it is sufficient to use resistors and capacitors. In principle, the formalism allows the description of any component as long as the port condition is not violated.

In a two-port network with a single component, such as a resistor, either a series connection (Figure 1.3a) or a shunt connection (Figure 1.3b) is possible.


(*a*) *Series impedance*   (*b*) *Shunt admittance*
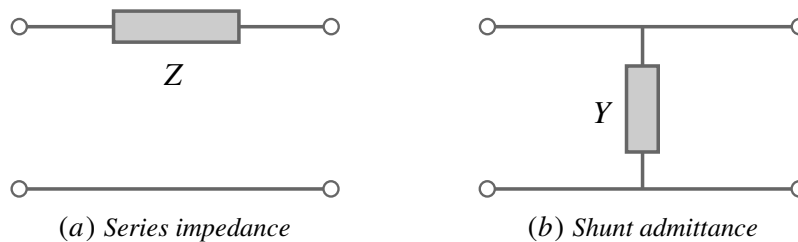
Figure 1.3: *Two elementary two-port networks*

The action of a two-port network is described by a complex 2×2 matrix that links input and output voltages and currents. The components A, B, C and D of the matrix are name-giving for this kind of description of a two-port network, the ABCD-parameters,

$$\begin{pmatrix} V_1 \\ I_1 \end{pmatrix} = \begin{pmatrix} A & B \\ C & D \end{pmatrix} \begin{pmatrix} V_2 \\ -I_2 \end{pmatrix} . \tag{1.24}$$

The series impedance and shunt admittance above correspond to the matrices shown in (1.25).

$$a_{\text{Series impedance}} = \begin{pmatrix} 1 & Z \\ 0 & 1 \end{pmatrix} \qquad a_{\text{Shunt admittance}} = \begin{pmatrix} 1 & 0 \\ Y & 1 \end{pmatrix} \tag{1.25}$$

From these elementary matrices, more complex structures are built by appropriate matrix multiplications. In addition, by combining several two-port networks

(*a*) *Series RC element* (*b*) *Two cascaded series RC elements*
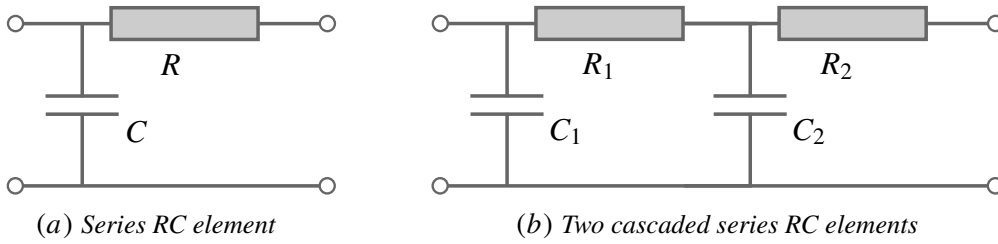
Figure 1.4: *Example of building more complicated networks from elementary two-port networks*

into a single circuit any desired network follows. There are several ways to connect two two-port networks, such as in series, parallel, or cascaded. An example of a cascaded circuit is shown in Figure 1.4. However, attention must be paid to ensure that the port condition is not violated during combination.

Yet, ABCD-parameter notation is only one of several available descriptions, each of which is best suited for a different application. Another perspective on the effect of a two-port network is available through the z-parameter matrix, Z_{ij}, which takes the form (1.26).

$$\begin{pmatrix} V_1 \\ V_2 \end{pmatrix} = \begin{pmatrix} Z_{11} & Z_{12} \\ Z_{21} & Z_{22} \end{pmatrix} \begin{pmatrix} I_1 \\ I_2 \end{pmatrix} \tag{1.26}$$

Here, the matrix elements are defined as

$$Z_{ij} = \left. \frac{V_i}{I_j} \right|_{I_k=0} \qquad \text{where } k \neq j \,. \tag{1.27}$$

Using z-parameters, it is straightforward to collapse a two-port network to a one-port network by applying a load, Z_L, on one of the ports or short-circuiting it. This is equivalent to imposing the condition

$$V_2 = -Z_\mathrm{L} I_2 \,. \tag{1.28}$$

The remaining input impedance, Z_in, of the leftover one-port network is

$$Z_\mathrm{in} = Z_{11} - \frac{Z_{12} Z_{21}}{Z_{22} + Z_\mathrm{L}} \,. \tag{1.29}$$

The series RC element in Figure 1.4a comprises a shunt capacitor and a series resistor. In a lumped element thermal model, it corresponds to a single lump and is therefore the most basic form of a thermal equivalent circuit. In the associated circuit diagram, the lower connection is grounded to represent the environment. This has the effect that all capacitors are connected to ground. To simplify the diagram, the lower connection is often omitted, see Figure 1.1. The temperature at each node corresponds to the voltage across the capacitors. Only voltages measured across the capacitors to ground correspond to temperature differences. The electrical resistance, R, corresponds to the thermal resistance as defined in (1.9), with all the caveats discussed in that section. By cascading series RC

elements, as shown in Figure 1.4b, a one-dimensional heat path is modeled. For this, the far side is short-circuited. The voltage across the remaining port typically corresponds to the junction temperature.

Owing to the importance of the case, the series RC circuit is analyzed in more detail below. When the port on the right side in Figure 1.4a is short-circuited, the differential equation for the voltage, V_C, across the capacitor reads as

$$RC\,\frac{\mathrm{d}V_C}{\mathrm{d}t} + V_C = V_{\text{in}}\,. \tag{1.30}$$

Here the time constant, τ, can be identified as $\tau = RC$. By comparing (1.30) with (1.18), the transfer function, $Z(s)$, is seen to be

$$Z(s) = \frac{1}{1 + RCs}\,. \tag{1.31}$$

The voltage response of a single series RC element has a pole on the negative real axis at

$$s = -\sigma_p = -\frac{1}{RC} = -\frac{1}{\tau}\,. \tag{1.32}$$

The step response for the capacitor voltage is

$$a(t) = 1 - \mathrm{e}^{-t/\tau}\,, \tag{1.33}$$

whereas the response to a delta pulse at $t = 0$ is

$$h(t) = \frac{1}{\tau}\,\mathrm{e}^{-t/\tau}\,. \tag{1.34}$$

A circuit like the one shown in Figure 1.4b is created by cascading two individual RC elements. Applying an appropriate matrix description and using (1.29), it is possible to show that two cascaded series RC networks have a transfer function, $Z(s)$, which takes the form of a continuous fraction of the type

$$Z(s) = \cfrac{1}{sC_1 + \cfrac{1}{R_1 + \cfrac{1}{sC_2 + \cfrac{1}{R_2}}}}\,. \tag{1.35}$$

Another type of RC circuit that will be useful for upcoming calculations is the parallel RC circuit depicted in Figure 1.5a. Here, the input function is the current, I, and the resulting voltage is the output. The differential equation connecting these quantities has the following form

$$C\,\frac{\mathrm{d}V}{\mathrm{d}t} + \frac{V}{R} = I\,. \tag{1.36}$$

The impedance for such a circuit is derived similarly as for the series RC circuit

(*a*) *Parallel RC element*   (*b*) *Two parallel RC elements connected in series*
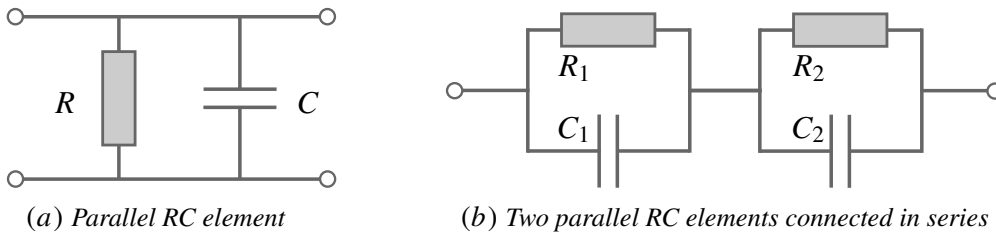
Figure 1.5: *RC elements as basic building blocks for thermal equivalent circuits*

and amounts to

$$Z(s) = \frac{R}{1 + RCs} \, . \tag{1.37}$$

The series connection of two such circuits takes the form shown in Figure 1.5b. The combined impedance of a series connection is the sum of the impedances and thus the total impedance of the circuit is

$$Z(s) = \frac{R_1}{1 + R_1 C_1 s} + \frac{R_2}{1 + R_2 C_2 s} \, . \tag{1.38}$$

1.3 Distributed RC lines

1.3.1 Transmission lines

In the previous section, the circuit-theoretical basics for lumped thermal models are treated. Sometimes, however, a description based on a distributed-element circuit is also appropriate. In contrast to lumped elements, distributed elements assume the impedance or admittance to be smeared over a finite section of space. The transmission line is such a one-dimensional distributed circuit element. The following remarks are based on [36].

A transmission line is a two-port network with a shunt admittance and a series impedance that are distributed over its length. In Figure 1.6, an infinitesimal section of such a circuit is shown. It has an admittance density, $y(x)$, and an impedance density, $z(x)$, on a section of length dx.
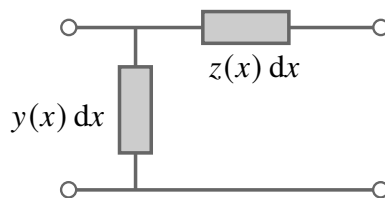

Figure 1.6: *Infinitesimal element of a general transmission line*

A typical application for the transmission line is the modeling of signal behavior on copper wires. In this case, the impedance, z, consists of a resistance density, r, and an inductance density, l. The admittance comprises a conductance density, g, and a capacitance density, c, each per unit length. This implies the

following form for y and z,

$$z = r + sl \quad \text{and} \quad y = g + sc \, . \tag{1.39}$$

The voltage, $V(x,s)$, between the two wires of the transmission line as a function of the position along the line, x, is governed by the Telegrapher's equation in the Laplace domain,

$$\frac{\mathrm{d}^2 V}{\mathrm{d}x^2} - z\, y \cdot V = 0 \, . \tag{1.40}$$

The time derivatives are implicit via the factors of s in (1.39). The densities are assumed to be independent of x, i. e. constant along the transmission line.

The general solution to this differential equation involves one solution running to the left and one running to the right with amplitudes V_1 and V_2

$$V(x) = V_1\, \mathrm{e}^{-\gamma x} + V_2\, \mathrm{e}^{\gamma x} \, . \tag{1.41}$$

The nature of the propagation is implicit in the propagation constant, γ. Due to s being a complex variable, see (1.17), γ is also complex. Its real part, α, is the attenuation constant and describes damping effects. The imaginary part, β, is called the phase constant.

$$\gamma = \sqrt{zy} \tag{1.42a}$$
$$= \alpha + \mathrm{i}\beta \, . \tag{1.42b}$$

When no resistive elements are present in the transmission line, it is said to be lossless and $\alpha = 0$. In the example of a lossless copper wire, this corresponds to $r = 0$ and $g = 0$.

The characteristic impedance, Z_0, describes the ratio of voltage amplitude to current amplitude in the transmission line and is given by

$$Z_0 = \sqrt{\frac{z}{y}} \, . \tag{1.43}$$

When a load, Z_L, or another transmission line is attached to the original transmission line with a differing Z_0, reflection will occur. It is possible to show that the input impedance in presence of a load, Z_L, which is driven via a transmission line of length Δx is

$$Z_\mathrm{in} = \overline{Z}_0 \frac{Z_\mathrm{L} \cosh(\gamma \Delta x) + \overline{Z}_0 \sinh(\gamma \Delta x)}{Z_0 \cosh(\gamma \Delta x) + Z_\mathrm{L} \sinh(\gamma \Delta x)} \, , \tag{1.44}$$

where $\overline{Z}_0$ is the complex conjugate of Z_0.
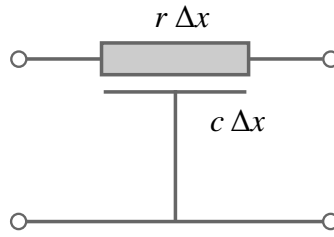
Figure 1.7: *Distributed RC line of length Δx*

1.3.2 Uniform RC lines

The uniformly distributed RC line is a transmission line where the shunt admittance corresponds to a capacitance while the series impedance is purely resistive. The distributed resistance, r, and the distributed capacity, c are constant along the transmission line. A finite length Δx is assumed, which means that $R = r \cdot \Delta x$ is the total resistance and the total capacity is $C = c \cdot \Delta x$. Figure 1.7 illustrates the situation.

When moving a distance dx along the RC line, the voltage, $V(x,t)$, between the two wires decreases by an amount proportional to the resistance density, r, and the current, $I(x,t)$, flowing along the line.

$$dV(x,t) = -r\, I(x,t)\, dx \tag{1.45}$$

At the same time, the shunt capacity causes a current change dI when moving dx along the line according to

$$dI(x,t) = -c\, \frac{dV(x,t)}{dt}\, dx\,. \tag{1.46}$$

Combining (1.45) and (1.46) gives

$$\frac{dV(x,t)}{dt} = \frac{1}{rc}\, \frac{d^2V(x,t)}{dx^2}\,. \tag{1.47}$$

This equation is structurally similar to the heat equation already derived in (1.7), if the source term is omitted. In this comparison, the term $1/rc$ corresponds to the thermal diffusivity $\alpha = k/c\rho$.

Consequently, the solution of an infinitely long distributed RC line has the same form as a solution of the related heat equation. For the RC line, if a charge, Q, is injected at the origin, the result is a voltage distribution according to

$$V(x,t) = \frac{Q/c}{2\sqrt{\pi t/rc}}\, \exp\left(-\frac{x^2}{4t/rc}\right)\,. \tag{1.48}$$

Solutions for arbitrary excitations or for the semi-infinite or finite RC line are constructed from this point using superposition and mirroring techniques. For a treatment of these cases, see [36].

The complex impedance, $Z(s)$, of a load Z_L driven via an RC line is constructed by using the general solution (1.44). The propagation constant for the RC line shown in Figure 1.7 is

$$\gamma = \sqrt{src}\,, \tag{1.49}$$

whereas the characteristic impedance amounts to

$$Z_0 = \sqrt{\frac{r}{sc}}\,. \tag{1.50}$$

1.3.3 Non-uniform RC lines

In the previous section, the resistance density, r, and capacitance density, c, are assumed to be constant along the transmission line. In this section, the problem of the non-uniform RC line is explored, although a general solution is not known. Here, the spatially dependent densities $r(x)$ and $c(x)$ amount to a total resistance, R, and total capacity, C, along an RC line of length Δx. Additional background and more detailed treatments on non-uniform RC lines are given in [36, 37, 38].

In a first step, the cumulative resistance, $R_\Sigma(x)$, and the cumulative capacitance, $C_\Sigma(x)$, are defined as the antiderivatives of the respective densities

$$R_\Sigma(x) = \int_0^x r(\xi)\,\mathrm{d}\xi\,, \tag{1.51a}$$

$$C_\Sigma(x) = \int_0^x c(\xi)\,\mathrm{d}\xi\,. \tag{1.51b}$$

This implies that at the beginning of the transmission line $C_\Sigma(0) = 0$ and $R_\Sigma(0) = 0$ holds true and therefore at the end $C_\Sigma(\Delta x) = C$ and $R_\Sigma(\Delta x) = R$ must apply.

The differential structure function is defined as the ratio of the resistance and the capacitance densities expressed as a function of cumulative resistance. It is referred to here as $\sigma(R_\Sigma)$. As a function of x, it reads

$$\sigma\big(R_\Sigma(x)\big) = \frac{c(x)}{r(x)}\,. \tag{1.52}$$

The cumulative structure function, also called the Protonotarious-Wing function, measures the cumulative capacitance as a function of the cumulative resistance.
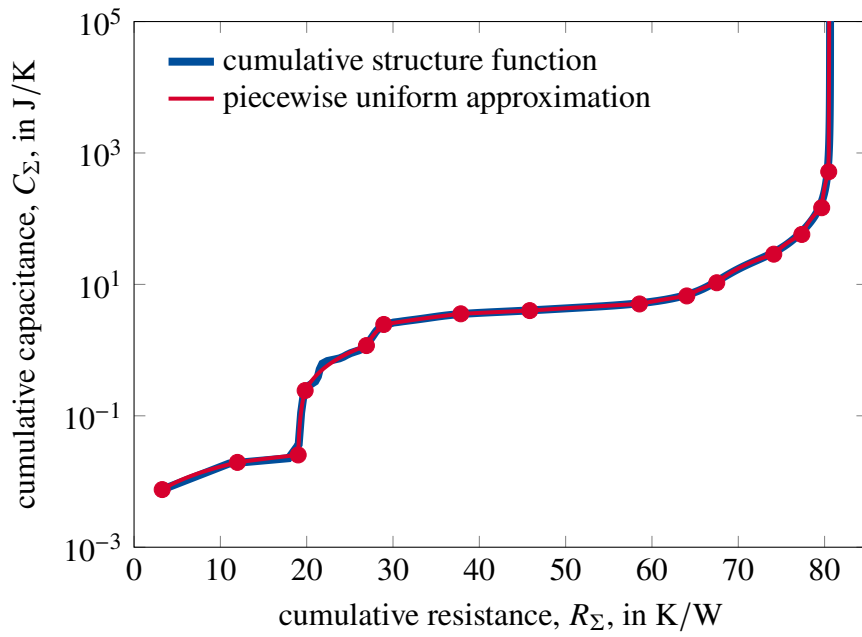
Figure 1.8: *Example of a typical cumulative structure function and its approximation via a piecewise uniform RC line. The red dots correspond to the end of each piecewise uniform section.*

It is calculated as

$$C_\Sigma(R_\Sigma) = \int_0^{R_\Sigma} \sigma(R'_\Sigma) \, dR'_\Sigma \tag{1.53a}$$

$$= \int_0^{x(R_\Sigma)} \frac{c(x)}{r(x)} \frac{dR_\Sigma}{dx} \, dx \tag{1.53b}$$

$$= \int_0^{x(R_\Sigma)} c(x) \, dx \, . \tag{1.53c}$$

In the following, the differential equation for the voltage in the case of spatially dependent densities is derived. Locally, the behavior of voltage and current is similar to the uniform case,

$$dV(x,t) = -r(x) \, I(x,t) \, dx \tag{1.54a}$$

$$dI(x,t) = -c(x) \frac{dV(x,t)}{dt} \, dx \, . \tag{1.54b}$$

Combining these two equations yields,

$$\frac{dV(x,t)}{dt} = \frac{1}{c(x)} \frac{d}{dx} \frac{1}{r(x)} \frac{dV(x,t)}{dx} \, . \tag{1.55}$$

A simplification is achieved by reformulating the differential equation using the

cumulative resistance, R_Σ, as the spatial variable,

$$\frac{dV(x,t)}{dt} = \frac{1}{\sigma(R_\Sigma)} \frac{d^2V(x,t)}{dR_\Sigma^2} . \tag{1.56}$$

As a general solution to (1.56) is not possible, a workable solution is to approximate a general cumulative structure function with a piecewise uniform RC line. A piecewise uniform RC line is a concatenation of uniform RC lines, which each have different r and c. In Figure 1.8, a typical cumulative structure function together with a piecewise approximation comprising 15 segments is shown. Note that due to the logarithmic scaling of the cumulative capacitance the piecewise uniform segments do not appear linear. A solution is available in the form of cascaded of uniform transmission lines according to (1.44).

1.4 Lumped element RC lines

1.4.1 Representations of RC lines

While non-uniform RC transmission lines are analytically described by any two positive integrable functions $r(x)$ and $c(x)$, in digital calculations discretization is obligatory. To generate a solution numerically, the behavior of a non-uniform RC line is approximated by a suitable circuit, as for example by cascaded series RC elements as shown in Figure 1.4. In this case, the values of the resistors and capacitors have to approximate $r(x)$ and $c(x)$ while maintaining the total resistance, R, and total capacitance, C, of the line. For an infinite number of elements, $n \to \infty$, the exact behavior of the original RC line is recovered. The topic of infinite-length distributed RC one-ports is covered by Vladimír Székely in [39].

For the treatment of a series RC circuit with n elements, the relations established in previous sections are used. The pole–zero representation introduced in (1.22) adapted to the current case reads

$$Z(s) = R \frac{(1 + s/\sigma_{z,1})(1 + s/\sigma_{z,2}) \dots (1 + s/\sigma_{z,n-1})}{(1 + s/\sigma_{p,1})(1 + s/\sigma_{p,2}) \dots (1 + s/\sigma_{p,n})} . \qquad (1.57)$$

Here, the poles lie at locations $s = -\sigma_{p,i} = -1/\tau_i$ with τ_i as defined in (1.32). The pole–zero representation allows to characterize a circuit by the knowledge of the locations of the poles and zeros as well as the total resistance, R.

The expression (1.57) is rearranged via partial fraction decomposition into a sum

$$Z(s) = \sum_{i=1}^{n} \frac{R_i}{1 + s/\sigma_{p,i}} . \qquad (1.58)$$

This is a generalization of (1.38) and can thus be interpreted as n parallel RC circuits in series. The corresponding step response, $a(t)$, is

$$a(t) = \sum_{i=1}^{n} R_i \left(1 - \exp(-t/\tau_i)\right) . \qquad (1.59)$$

This result is calculated analogous to the series RC circuit, see (1.31), in which case the step response is (1.33).

To facilitate a later generalization of the expressions to the infinite case, $n \to \infty$, (1.59) is rewritten as an integral in (1.60).

$$a(t) = \int_{-\infty}^{\infty} \rho(\tau)\left(1 - \exp(-t/\tau)\right) d\tau \qquad (1.60)$$

Here, the time constant spectrum, $\rho(\tau)$, is introduced, which for finite n is a
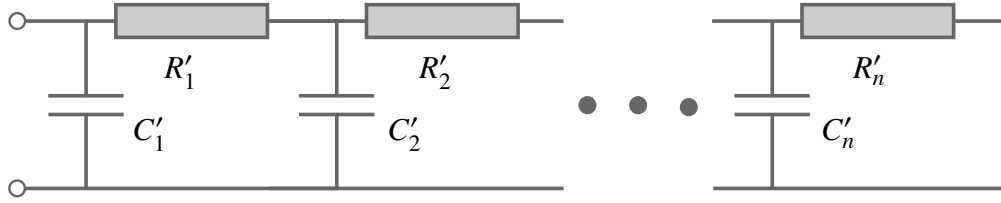
Figure 1.9: *Cauer network with n elements*

sum of delta peaks at locations τ_i with intensity R_i,

$$\rho(\tau) = \sum_{i=1}^{n} R_i \, \delta(\tau - \tau_i) \, . \tag{1.61}$$

In the limit $n \to \infty$, the time constant spectrum, $\rho(\tau)$, becomes a continuous density. In practice, the time constant spectrum is often formulated in logarithmic time, $\zeta = \ln(\tau)$. The logarithmic time constant spectrum is denoted $R(\zeta)$. The logarithmic relations are covered in detail below.

Similar to the case of finite n, in the limit $n \to \infty$ the distribution of poles and zeros on the negative real axis characterizes the RC line. The dipole intensity function, I_{d}, is the appropriate description in the continuous case. The information is not carried by the number and location of the poles and zeros, but by their relative distance in the limit. For convenience, the logarithmic negative real axis is denoted $\Sigma = \ln(-\sigma)$ (compare (1.17)). In this notation, $\Delta\Sigma$ is the distance between two adjacent poles and $\delta\Sigma$ measures the distance between a zero and the pole left from it. The dipole intensity function is defined as

$$I_{\mathrm{d}}(\Sigma) = \lim_{\Delta\Sigma \to 0} \frac{\delta\Sigma}{\Delta\Sigma} \tag{1.62}$$

and lies between zero and one.

1.4.2 Foster and Cauer synthesis

Network synthesis deals with the design of circuits based on a predefined impedance. Its goal is to derive the numerical values of the components that make up the circuit in such a way that the resulting impedance matches the predefined impedance. For a given one-port impedance, many network geometries are possible, which approximate or exactly realize the impedance.

In the present case, the objective is to relate a Foster-type network, which has the form shown in Figure 1.10, to a Cauer-type network, see Figure 1.9. Both networks are generalizations of simpler forms discussed previously in the context of Figures 1.4 and 1.5.

To distinguish the components in the respective networks, resistances and capacitances in Foster networks are denoted with R_n and C_n, respectively, while resistances belonging to Cauer networks are denoted as R'_n and capacitors as C'_n, using a prime. Note that only the resistances and capacitances of the Cauer network correspond to the thermal resistances and thermal capacitances.
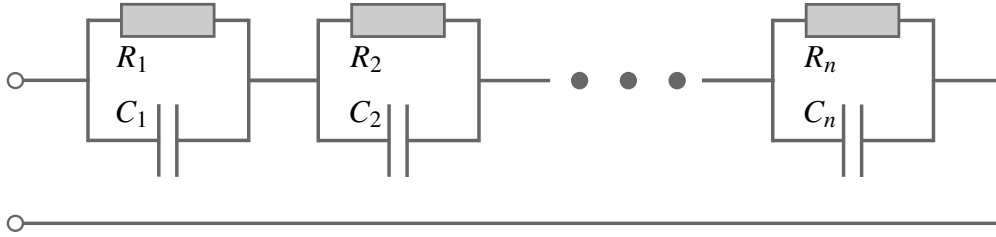
Figure 1.10: *Foster network with n elements*

An algorithm for the Foster-to-Cauer transformation is described below in subsection 1.6.3. The transformation from a Cauer network to a Foster network is not discussed here, since a transformation in this direction is not necessary in practice.

The impedance of the Cauer network in Figure 1.9 has the form of a continued fraction, known as Stieltjes continued fraction [40]

$$Z(s) = \cfrac{1}{sC_1' + \cfrac{1}{R_1' + \cfrac{1}{sC_2' + \cfrac{1}{R_2' + \cfrac{1}{\ddots + \cfrac{1}{sC_n' + \cfrac{1}{R_n'}}}}}}} . \qquad (1.63)$$

According to (1.58) the Foster impedance is

$$Z(s) = \sum_{i=1}^{n} \frac{R_i}{1 + sR_iC_i} . \qquad (1.64)$$

Given the impedance $Z(s)$ it is possible to construct a Cauer network using polynomial long division, for example using the Euclid algorithm. In practice, $Z(s)$ is derived from the time constant spectrum, as is explained in detail below. To perform the transformation, resistors, R_n', and capacitors, C_n', are iteratively separated from $Z_n(s)$ according to

$$\frac{1}{Z_n(s)} = sC_n' + \frac{1}{R_n' + Z_{n-1}(s)} , \qquad (1.65)$$

where the starting point is the Foster impedance, $Z_n(s) = Z(s)$, which is calculated via (1.64). A division of this type is always possible because the order of the numerator polynomial is smaller than the order of the denominator polynomial, see (1.57).

1.5 Thermal analysis

1.5.1 Network identification by deconvolution

In a thermal response measurement, a system is subjected to a step in heating or cooling power and the resulting temperature change, i.e. the reaction of the system, is observed. Typically, from a system in equilibrium the impulse response or the step response is measured with the goal to reconstruct the relevant thermal properties of the system. In the one-dimensional case, this corresponds to constructing an equivalent Cauer network with known resistances and capacitances. The method laid out in this section is known as *network identification by deconvolution* [7, 9].

The thermal impedance, $Z_{th}(t)$, is the step response of a system in equilibrium due to a power step, P,

$$Z_{th}(t) = \frac{T_0 - T(t)}{P} \,. \tag{1.66}$$

From this, the impulse response, $h(t) = \partial_t Z_{th}(t)$, is calculated. In most cases in practice, it is easier to realize a step in the heating power in good approximation than a delta pulse of similar magnitude and duration. From (1.11) it follows that once $h(t)$ is known the temperature response of the system to an input heating power is calculated via

$$T(t) = T_0 + \int_0^t P(t')h(t - t') \, dt' \,. \tag{1.67}$$

If the impulse response of the system, $h(t)$, is converted to Laplace space the resulting transfer function, $Z(s)$, is the impedance of the equivalence network. Numerical knowledge of $Z(s)$, however, does not imply knowledge about the resistances and capacities of an equivalent Cauer network.

In practice, it is convenient to perform calculations on a logarithmic timeline and measure time constants logarithmically via

$$z = \ln(t / t_0) \tag{1.68a}$$
$$\zeta = \ln(\tau / \tau_0) \,. \tag{1.68b}$$

Theoretically, the response to a Heavyside function input, as in (1.13), is defined for all $t \in (0, \infty)$. Consequently, this makes $z \in (-\infty, \infty)$ and leaves no defined initial time. In practice, the finite time resolution produces a minimum measured time $t_{min} > 0$ that results in a $z_{min} > -\infty$. Thus, a constant shift, z_0, is applied to make the situation mathematically equivalent to expressions in linear time t.

In the following, it is implied that t_0 and τ_0 are equal to one second, so that z and ζ measure time relative to seconds. For clarity, the constants t_0 and τ_0 are omitted in the following. Similarly, z_{min} is assumed to exist. In practice, responses in logarithmic time will typically start at some small negative z-value and the system is assumed to show no reaction before that time.

The step response in logarithmic time, z, is denoted $a(z)$ and follows as

$$a(z) = Z_{\text{th}}(\exp(z)) \,. \tag{1.69}$$

The time constant spectrum (1.61) expressed in terms of ζ has the form (1.70) and is called the logarithmic time constant spectrum, $R(\zeta)$. In the case of finite n, it is a sum of delta peaks with magnitudes R_i,

$$R(\zeta) = \sum_{i=1}^{n} R_i \, \delta(\zeta - \ln(\tau_i)) \,. \tag{1.70}$$

The integral expression (1.71) is the step response in linear time (1.60) converted to logarithmic time.

$$a(z) = \int_{-\infty}^{\infty} R(\zeta)\big(1 - \exp(-\exp(z - \zeta))\big) \, \mathrm{d}\zeta \tag{1.71}$$

From this, the impulse response is obtained via derivation,

$$\frac{\mathrm{d}}{\mathrm{d}z} a(z) = h(z) = \int_{-\infty}^{\infty} R(\zeta) \exp(z - \zeta - \exp(z - \zeta)) \, \mathrm{d}\zeta \,. \tag{1.72}$$

This integral has the form of a convolution of $R(\zeta)$ with a function $w_z(z)$

$$h(z) = (R \otimes w_z)(z) \,, \tag{1.73}$$

which is defined as

$$w_z(z) = \exp(z - \exp(z)) \,. \tag{1.74}$$

To identify the Cauer network of the system, the convolution (1.73) is solved for $R(\zeta)$. Once the logarithmic time constant spectrum is obtained, a Foster network with resistances R_i and capacitances C_i is readily constructed. The corresponding impedance can be calculated with the help (1.58). The time constant spectrum is discretized into sections of width $\Delta\zeta_i$ which are located at the positions ζ_i. The resistances and capacitances are obtained as

$$R_i = R(\zeta_i) \cdot \Delta\zeta_i \,, \tag{1.75a}$$

$$C_i = \frac{\exp(\zeta_i)}{R(\zeta_i) \cdot \Delta\zeta_i} \,. \tag{1.75b}$$

The resistances, R_i', and capacitances, C_i', belonging to the equivalent Cauer network can then be constructed iteratively using (1.65). With the knowledge of the circuit, an approximation to the cumulative structure function, $C_\Sigma(R_\Sigma)$, can be constructed.

Note that for the purpose of network identification by deconvolution the driving-point behavior of the RC circuit is of interest and the time constant spectrum has to be non-negative. In contrast, if the transfer behavior of the RC circuit is analyzed, the time constant spectrum may also be negative [8].

If only $Z(s)$ is known, the logarithmic time constant spectrum, $R(\zeta)$, is calculated as the imaginary part of $Z(s)$ along the negative real axis,

$$R(\zeta) = \frac{1}{\pi} \, \mathrm{Im}[Z(s = -\exp(-\zeta))] \,. \tag{1.76}$$

Due to the poles on the negative real axis, (1.76) cannot be evaluated directly. As a workaround, a small angle, δ, is introduced that tilts the integration path into the complex plane, see (1.77). This has the effect of smoothing the delta peaks, making them finite as laid out in [12].

$$s = -(\cos(\delta) + \mathrm{i}\sin(\delta))\exp(-\zeta) \tag{1.77}$$

With the time constant spectrum, $R(\zeta)$, known, application of (1.73) yields the impulse response, which gives the thermal impedance, Z_{th}, via (1.69).

1.5.2 Thermal structure functions

From a numerical point of view, every step response is connected to a thermal structure function via the algorithm of network identification by deconvolution. However, the structure function is per definition a strictly one-dimensional model. The model becomes ill-defined if parasitic heat paths become significant and the one-dimensional model is not justified. In this case, the resistances and capacities of the thermal structure function from a network identification by deconvolution cannot be unambiguously assigned to the components of the device. In essence, the problem is similar to that of the proper definition of thermal resistance as discussed in Subsection 1.1.2 at the beginning of this work. Naturally, in heat conduction phenomena the one-dimensional assumption is always violated to a certain degree. The quality of the approximation depends on the specifics of each problem. In practice, the validity might depend on the environment conditions, the interactions with neighboring heat sources or the quality of a thermal isolation. In the case of a three-dimensional model, the one-dimensional approximation is suitable if thermal properties and excitation are sufficiently symmetrical. A resulting model might reflect a cylindrical, cone-like or (half) spherical heat path. Alternatively, the one-dimensional approximation might only be applicable for some parts of the device under test or only a section of the heat path. The impact of heat spreading effects on the structure functions is recognized [41, 42]. In an attempt to model the heat spreading effect induced by increasing cross-sectional areas along the heat path, an effective heat spreading angle is introduced in [43].

While this applies to the thermal structure function, the time constant spectrum is defined on a more general basis, because the resistances and capacities in the Foster network do not correspond to thermal resistances and capacities, see Section 1.4.2. As a consequence, temperature predictions based on the time constant spectrum, thermal impedance, and impulse response calculated via (1.69) are always well-defined.

It was proven by Codecasa that a three-dimensional heat conduction problem modeled with an RC one-port network still has a well-defined thermal structure function [44]. The one-dimensional approach of the network identification by deconvolution simply cannot provide this structure function. For this, the three-dimensional resistance and capacitance densities have to be known. In a three-dimensional model, the cumulative thermal resistances and the cumulative thermal capacitances of the structure function are defined in terms of spatial averages of the material parameters in expanding spatial regions. A description of the approach by Codecasa to calculate structure functions from three-dimensional models is given in [45]. In short, the approach is to solve a wave propagation problem related to original heat conduction problem. From this, an equivalent LC transmission line is constructed. By analogy, the elements of the structure function are defined in terms of spatial averages over the regions of the wave-fronts.

1.5.3 Transient thermal testing

The purpose of this section is to give a brief overview of how the method of network identification by deconvolution was developed and to explain how it is applied in practice. Additionally, recent developments in the field of compact thermal modeling are highlighted. A review encompassing the broader field of compact thermal modeling is provided by [21] and [46].

Early work in the field of transient thermal model generation, John W. Sofia in 1995 [47] and G. Oliveti *et al.* in 1997 [48], do not use network identification by deconvolution. Instead, they are based on fitting techniques. The idea of these publications is to optimize the resistances and capacitances of a low-order RC network to approximate the measurement data. The above works use three and six stage networks, respectively.

The method of network identification by deconvolution was first described by Vladimir Székely and Tran Van Bien from the Technical University of Budapest in 1988 [49]. A comprehensive summary of the theoretical background of thermal structure function and some considerations on possible implementations are given in [9].

In December 1995, a standard was released by the Electronic Industries Association and the JEDEC Solid State Technology Association establishing good practices for performing thermal measurement in electric devices [50]. Commonly, the temperature of an integrated circuit is measured via a temperature-sensitive parameter, such as the forward voltage of a diode. To that end, a K-factor calibration is performed that relates the forward voltage to the junction temperature. In diodes, the cooling curves are measured with the help of a small sensing current after the heating current is turned off. In this way, heating during the measurement process is avoided. While switching from heating to measurement current, electric transients occur masking the true temperature development for a short time. The treatment of these electric transient, for example via extrapolation, is discussed extensively in the literature [7, 51, 52].

Thermal impedance measurements on IGBTs using the VCE-method (collector-emitter voltage) are described in the JEDEC standard JESD24-12 [53].

On the basis of the transient thermal characterization procedure developed at the Department of Electron Devices at the Budapest University of Technology and Economics, a spin-off company was founded, which commercialized the measurement procedure described above. The company, called MicReD Microelectronics Research and Development, was acquired by Mentor Graphics which today (2021) is part of Siemens. Its main product, the "T3ster", comprises both the measurement hardware and software for thermal transient testing and is still being improved and updated. However, details regarding the implementation of the network identification by deconvolution in the T3ster software are not disclosed. Common practices concerning the implementation of the network identification by deconvolution are gathered below as far as they are reported in the literature.

A wide range of thermal testing practices are standardized by the JEDEC committee "JC-15 Thermal Characterization Techniques for Semiconductor Packages", including network identification by deconvolution. A case study on the use of structure functions at Infineon Technologies from 2008 is found in [41]. The publication warns of pitfalls posed by numerical artifacts and thus highlights the importance of robust algorithms and careful interpretation of the results.

Since its first release, further research has been conducted to refine the practices and to adapt network identification by deconvolution to a wide range of applications. Special mention is given to the International Workshop on Thermal Investigations of ICs and Systems, abbreviated THERMINIC, a European conference, where research related to thermal structure functions is discussed intensively. In the following, an overview over the field is given without any claim to completeness.

One area that has become a major field of application for network identification by deconvolution is the thermal characterization of LEDs. Therefore, there are several JEDEC standards dealing specifically with transient measurements on LEDs [54, 55]. Modern high-performance LEDs feature extreme power densities at the p-n junction, which is close to the phosphor. Due to the Stokes shift, this temperature sensitive component acts as an additional heat source. This makes good thermal management a priority for LEDs [56].

A paper from M. Rencz works out the importance of correcting systematic errors when the one-dimensional heat flow assumption is noticeably violated [57]. Parasitic heat flow paths such as convection, radiation losses, and conduction through secondary components can induce errors in the calculated material parameters, i. e. the thermal resistances and thermal capacitances, on the order of 20 %. As the work shows, correcting for these errors can yield a significant improvement in accuracy.

An imperfect measuring device causes inaccuracies. Examples include a finite rise time or a delay of the power step, or the finite bandwidth of an amplifier. The consequences of these effects and possible ways to correct them are discussed by Székely and Szalai in [58].

Another aspect that gives rise to extensive discussions is the long time that thermal transient measurements can take in practice. Depending on the device under test, the combined heating and cooling time can take up to an hour. A procedure by Schmid *et al.* to conduct repeated measurements on the same device without having to wait for thermal equilibrium in each repetition is discussed in [10, 59]. The idea of measuring truncated impedances, i. e., cutting the measurement before thermal equilibrium is reached again, is discussed in [52]. Other research treats thermal transient measurements in non-equilibrium conditions [60] or the use of short-pulse excitation instead of a step excitation [61], both with the goal of reducing the measurement time.

Instead of the conventional electronic temperature measurement, in another work pump-probe transient thermoreflectance was combined with network identification by deconvolution [62]. Using a delta pulse excitation the thermal parameters of very thin structures are determined. In their work, the authors highlight the importance of a sufficient temporal resolution and accurate algorithms.

An alternative approach to generate compact thermal models from the thermal response of a device is presented in [45, 63]. The method uses a multi-point moment-matching algorithm to generate structure functions without the need for deconvolution for the price of significantly increased computational time [64].

1.6 Algorithms

1.6.1 Derivation

In this section, different implementations for network identification by deconvolution found in the literature are discussed. The discussion focuses on the three most challenging tasks, namely the differentiation, the deconvolution and the Foster-to-Cauer transformation.

When a step response, $a(t)$, is recorded, it is differentiated to obtain the impulse response, $h(t)$. However, accurate differentiation is a numerically challenging task. Additionally, this issue is exacerbated by the fact that the subsequent deconvolution is a very noise sensitive procedure. For a precise differentiation, it is crucial to both limit the noise in the signal and not to introduce a significant bias into the derivative.

In statistics, this dilemma is known as the bias-variance tradeoff [65, 66]. It describes the conflict of interests between using large versus small windows. Including many data points to calculate a derivative leads to a low variance. On the other hand, larger windows are less sensitive to small and sudden changes in the signal and consequently are prone to misrepresent the derivative of such parts of the signal.

When working with real measurement data, additional challenges arise due to the conversion to logarithmic time, $z = \ln(t)$. During measurements, a signal is sampled at a constant rate in real time, t. Translating the signal to logarithmic time leaves it sparse in the beginning and dense at the end. This leads to a low accuracy, which is especially detrimental when calculating derivatives. In

classical forward-voltage-based measurements, this issue is masked to a certain extent by the electric transients. In that case, the sparse sections of the signal have to be discarded anyway [7]. For these reasons, Ezzahri and Shakouri note in their paper that ideally the sampling rate should be at least 10 to 15 times higher than the smallest time constant in the signal [62].

In the literature, it is reported that "Z_{th} curves must be extremely noise free" [56, p. 129] and that the solution is "extremely sensitive to noise" [7, p. 16]. As implementations for the derivative, the JEDEC suggests a straight line fit [7], while Schmid *et al.* found a Savitzky-Golay filter of second order to yield good results [59]. Further below, the implementation used in this work will be explained.

1.6.2 Deconvolution

Fourier deconvolution

The idea of Fourier deconvolution is to transform the convolution equation for the time constant spectrum (1.73), reproduced here,

$$h(z) = (R \otimes w_z)(z) = \int_{-\infty}^{\infty} R(\zeta) \exp(z - \zeta - \exp(z - \zeta)) \, d\zeta, \qquad (1.78)$$

to the Fourier domain, where it separates into a multiplication. In practice, the fast Fourier transform algorithm is often used.

Let $W(\Phi)$ be the Fourier transform of $w_z(z)$ and $V(\Phi)$ be the Fourier transform of $R(\zeta)$. When working with measurement data, the impulse response, $h(z)$, has a noise component, $n(z)$, superimposed onto it. To represent this, the measured signal is denoted $m(z)$,

$$m(z) = h(z) + n(z). \qquad (1.79)$$

Its Fourier transform is accordingly called $M(\Phi)$. With the addition of noise, the convolution (1.78) in Fourier space becomes

$$M(\Phi) = V'(\Phi) \cdot W(\Phi), \qquad (1.80)$$

where $V'(\Phi)$ is the actually obtained Fourier transform of the time constant spectrum. The Fourier transform of (1.79) is inserted into (1.80), where $H(\Phi)$ and $N(\Phi)$ are the Fourier transforms of $h(z)$ and $n(z)$, respectively,

$$H(\Phi) + N(\Phi) = V'(\Phi) \cdot W(\Phi). \qquad (1.81)$$

Equation (1.81) solved for the transformed time constant spectrum, $V'(\Phi)$, reads

$$\frac{M(\Phi)}{W(\Phi)} = V'(\Phi) = V(\Phi) + \frac{N(\Phi)}{W(\Phi)}. \qquad (1.82)$$

The noise component in the signal introduces an additional term to the exact time constant spectrum, $V(\Phi)$. As part of the deconvolution, noise components are enhanced greatly in parts where $W(\Phi)$ is close to zero.

Because of this, it is common to filter out high frequency components of the spectrum. To this end, $V'(\Phi)$ is multiplied by a filter function or window function. There are many filter functions available [67]. In the literature, Székely reports the use of a Gauss filter [8], while the JEDEC claims that a Fermi-Dirac function of the form

$$F_{\text{Fermi}}(\Phi) = \frac{1}{\exp\left(\frac{|\Phi| - \mu}{\beta}\right) + 1} \tag{1.83}$$

with appropriate μ and β shows good results [7]. Furthermore, Wiener optimal filtering can also be applied to the spectrum [68], but no results using it in the context of network identification by deconvolution are reported in the literature.

Inverse filtering

Another approach to solve (1.78) is inverse filtering. Its application to thermal transient measurements is discussed by Székely in [61].

The approach is to find an inverse filter function, $i(z)$, which is defined by its action on the forward filter function $w_z(z)$,

$$(w_z \otimes i)(z) = \delta(z), \tag{1.84}$$

to yield a delta function when convolved with it. Following this definition inverse filtering provides the time constant spectrum according to

$$R(\zeta) = (h \otimes i)(\zeta) = \int_{-\infty}^{\infty} h(z)\, i(\zeta - z)\, dz. \tag{1.85}$$

An algorithm to construct $i(z)$ is described in [61].

Bayesian deconvolution

A third method to solve the convolution equation (1.78) makes use of the Bayesian theorem and was introduced by Kennett *et al.* in 1978, [69, 70, 71]. Bayesian deconvolution is an iterative procedure and the iteration rule for network identification by deconvolution is derived below.

In computer-based calculations, the convolution (1.78) becomes a summation and functions are represented by vectors. Note that for Bayesian deconvolution the z-values at which the functions are evaluated have to be evenly spaced.

$$h[z] = \sum_{\zeta} w_z[z - \zeta] R[\zeta] \tag{1.86}$$

Here, square brackets are used to indicate a discrete integer dependence. Equivalently, the convolution can also be written in matrix-vector notation, where

$w_z[z - \zeta]$ becomes a Toeplitz matrix, denoted W, which has shifted versions of $w_z(z)$ as column entries. In these terms, the convolution reads

$$h = W \cdot R \,, \tag{1.87a}$$

or alternatively in index notation,

$$h_i = W_{ij} R_j \,. \tag{1.87b}$$

Starting point to derive the Bayesian deconvolution is Bayes' theorem (1.88). As the goal of the deconvolution step is to determine $R(\zeta)$ from $h(z)$, Bayes' theorem is formulated for the likelihood of R given h, commonly denoted $P(R \,|\, h)$,

$$P(R \,|\, h) = \frac{P(h \,|\, R)\, P(R)}{P(h)} \,. \tag{1.88}$$

$P(R)$ and $P(h)$ are the a priori probabilities of $R(\zeta)$ and $h(z)$. Which values should be assigned to these probabilities is discussed later.

Note that the conservation of probability (1.89) guarantees that when the conditional probability $P(R_i \,|\, h_k)$ is summed over all conditions, $P(R_i)$ is retained,

$$P(R_i) = \sum_k P(R_i \,|\, h_k)\, P(h_k) \,. \tag{1.89}$$

Because R_j is a vector, Bayes' theorem has to formulated in vector notation too and (1.88) generalizes to (1.90),

$$P(R_i \,|\, h_k) = \frac{P(h_k \,|\, R_i)\, P(R_i)}{\sum_j P(h_k \,|\, R_j)\, P(R_j)} \,. \tag{1.90}$$

Inserting (1.90) into (1.89) leads to

$$P(R_i) = P(R_i) \sum_k \frac{P(h_k)\, P(h_k \,|\, R_i)}{\sum_j P(h_k \,|\, R_j)\, P(R_j)} \,. \tag{1.91}$$

Simplifying this equation, the conditional probability, $P(h_k \,|\, R_j)$, is identified as W_{kj} from (1.87b). The a priori probability $P(h_k)$ is known and is simply h_k, while the value chosen for $P(R_j)$ is not critical, because the end result should not depend on it. For the resulting iteration (1.92), the starting point $R_j^{(0)}$ is chosen as $P(R_j) = R_j^{(0)} = h_k$,

$$R_i^{(n+1)} = R_i^{(n)} \sum_k \frac{h_k\, W_{ki}}{\sum_j W_{kj}\, R_j^{(n)}} \,. \tag{1.92}$$

The Bayesian deconvolution has two important properties that make it attractive

for the application in network identification by deconvolution. First, it preserves the area under the curve, since the area under $w_z(z)$ is equal to one. This means that the steady state thermal resistance is preserved during deconvolution to a high degree of accuracy. Secondly, since Bayesian deconvolution deals with probabilities at its core, the results are guaranteed to be non-negative.

Ezzahri and A. Shakouri report the use of Bayesian deconvolution [62]. Székely claimes that approximately 1000 iterations steps are sufficient for network identification by deconvolution [9, 72]. The use of the same number of iteration steps is reported by Schmid *et al.* [10].

1.6.3 Foster-to-Cauer transformation

Three methods for the Foster-to-Cauer transformation are reported in the literature. A method presented by Codecasa employing a tridiagonalization approach is presented in [73]. The method makes use of well-conditioned algorithms for the tridiagonalization of matrices, such as the Lanczos algorithm, to determine the elements of a Cauer network starting from a suitable system of differential equations. There exist two alternative methods for performing the Foster-to-Cauer transformation. They are described by by Khatwani in 1976 and Sobhy in 1973 [74, 75, 76]. Khatwani presents an algorithm for calculating the elements of a continued fraction via the Markov parameters of $Z(s)$.

The most commonly used algorithm for the Foster-to-Cauer transformation is based on a continued polynomial long division. A detailed algorithm for this task is described in [77] and reproduced here. As a starting point, the Foster network impedance, $Z(s)$, is calculated from the time constant spectrum. The resistances and capacitances of the network are derived from it according to (1.75a) in combination with (1.75b). Subsequently, the impedance is constructed following (1.65). To perform a polynomial division, all the terms have to be added up such that a rational function of the type (1.21) is received.

For convenience, the recurrence relation governing the Foster-to-Cauer transformation (1.65) is reproduced in (1.93).

$$\frac{1}{Z_n(s)} = sC_n' + \frac{1}{R_n' + Z_{n-1}(s)} \tag{1.93}$$

First, $Z_n(s)$ is split into a numerator polynomial $p_n(s)$ and a denominator polynomial $q_n(s)$. As the order of $q_n(s)$ is always exactly one higher than that of $p_n(s)$, the inverse of the impedance is expanded via a polynomial division into a linear part and a remainder $r_n(s)$,

$$\frac{1}{Z_n(s)} = \frac{q_n(s)}{p_n(s)} = sC_n' + \frac{1}{R_n'} + \frac{r_n(s)}{p_n(s)} \ . \tag{1.94}$$

From the coefficients of the result, the resistances, R_n, and capacitances, C_n, of

the Cauer network follow. A new impedance $Z_{n-1}(s) = \frac{p_{n-1}(s)}{q_{n-1}(s)}$ is received via

$$p_{n-1} = -R'_n \cdot r_n(s) \tag{1.95a}$$

$$q_{n-1} = \frac{p_n(s)}{R'_n} + r_n(s). \tag{1.95b}$$

In the last step, $p_0(s) = 0$ marks the end of the iteration. When the order of $q_n(s)$ and $p_n(s)$ increases, the coefficients quickly exceed the accuracy boundaries of double precision floating point arithmetic. Typically, this happens between polynomial orders of 50 to 100. Because of this, it is common practice to use arbitrary floating point precision [7, 56]. In this way, it is reported that polynomials of order 150 to 200 are possible [56].

1.6.4 Inverse calculation

The goal of network identification by deconvolution is to derive a structure function from a given step response. An inverse calculation means to derive a step response from a structure function. Information about the structure of a system can either be derived from its geometry and material properties or deduced from a structure function, if it is known.

In the latter case, as for instance shown in Figure 1.8, the structure function is approximated by piecewise uniform RC lines that each contribute a resistance, R, and capacitance, C, to the total.

If the material parameters are known, i.e. the thermal conductivity, k, the specific heat capacity, c_m, and the density, ρ, as well as the cross-sectional area, A, then the resistance density, r, and capacitance density, c, follow from

$$r = \frac{1}{k\,A}, \tag{1.96a}$$

$$c = c_m \cdot \rho \cdot A. \tag{1.96b}$$

Given the length of the section, Δx, R and C follow directly.

In either way, once R and C of each section have been determined (1.44) in combination with (1.49) and (1.50) yields the thermal impedance. The impedance of the transmission line must be calculated sequentially by using the input impedance of the previous section as the load impedance of the next, starting at the termination, i.e. at the short-circuited end with a vanishing load impedance.

Given the impedance, $Z(s)$, (1.76) is employed in combination with (1.77) to derive the time constant spectrum. It is then convolved according to (1.73) and subsequently integrated to obtain the step response, $a(z)$.

In the literature, it is reported that the angle, δ, in (1.77) should be not more than $2°$ to $5°$ [12]. The time constant spectrum is sampled at approximately 30 points per decade [61, 78]. The standard JESD 51-14 recommends a sampling rate of at least 50 points per decade [7].

Chapter 2

Network identification

Some results in this chapter have been published in [79]*,* [80] *and* [81]*.*

2.1 Implementation of network identification

In this section, the implementation of network identification used in this work is discussed. Different variants of established methods are systematically evaluated and compared against each other as well as against novel techniques developed in this work.

2.1.1 Software libraries

For all computations, python 3.7.9 is used. To perform standard computational tasks such as the fast Fourier transform or array sorting, the packages numpy 1.19.2 [82] and scipy 1.5.2 [83] are relied on. For multidimensional optimization, the implementation of the solvers provided by scipy are utilized. For accurate polynomial long division, arbitrary floating point arithmetic via gmpy2 version 2.0.8 [84] is used. The calculation times given below are gathered for a computer with an Intel Core i7-8665U CPU at 1.90 GHz and 16 GB RAM running under Windows 10.

2.1.2 Optimal regression filtering

The implementation of network identification by deconvolution used in this work relies on a regression filter to derive the impulse response from the thermal impedance. Using the logarithmic thermal impedance, $a(z) = Z_{th}(\exp(z))$, a locally weighted scatterplot smoothing, abbreviated LOWESS, is performed. The method is based on least squares local polynomial regressions on a small interval centered around each data point. From the regression, the true signal and its derivative are estimated. In this way, it is possible to calculate the derivative of the step response and reduce noise components in the signal in the same step.

As outlined in Subsection 1.6.1, it is important to choose an appropriate window length that balances the bias-variance tradeoff. Because of that, the LOWESS filter is supplemented by an adaptive window length algorithm which re-evaluates the bias-variance tradeoff for each regression individually. To decide

on the best window length, Stein's unbiased risk estimate, abbreviated SURE, is employed. The idea is based on a paper by Krishnan and Seelamantula [65]. An adaptation of the algorithm suitable for network identification by deconvolution, is presented here.

A noisy signal is described by assuming an underlying true signal, s_i, which is superimposed by (white) noise, w_i. The observed values, x_i, can be described as

$$x_i = s_i + w_i .\tag{2.1}$$

Here, i enumerates the data points in a time series measurement. Each set, $\{x_i, s_i, w_i\}$, has an associated logarithmic time z_i.

From the set of all measurement points, $\boldsymbol{X}$, a small subset, $\boldsymbol{x}$, is taken to calculate an approximation of the true value, s_i. Here, the size of the interval measured in logarithmic time, z, is called window length, L, while the window size, N, denotes the number of data points in, $\boldsymbol{x}$. To achieve a good fit, the window length must be chosen carefully. To that end, a polynomial of low order is fitted to $\boldsymbol{x}$ via a least squares regression that generates a prediction, $f_i(\boldsymbol{x})$, of s_i. Typically, x_i is located in the center of $\boldsymbol{x}$, such that $\boldsymbol{x}$ lies inside $[x_i - L/2, x_i + L/2]$. This is, however, not exactly guaranteed because of a possibly uneven spacing of the data points in logarithmic time. Additionally, at the boundaries $\boldsymbol{x}$ is evaluated off-center. A polynomial of first order has performed best in practice. The derivative of s_i can then simply be approximated by the gradient of the linear regression.

In the regression, the data points are weighted according to their distance, Δx from x_i via a tricubic weight function, $w(x_i)$. It is defined as

$$w(\Delta x) = \begin{cases} \left(1 - \dfrac{|\Delta x|^3}{L}\right)^3 & \text{for} \quad \Delta x < L \\ 0 & \text{for} \quad \Delta x \geq L \end{cases} .\tag{2.2}$$

Additionally, each data point is assigned a weight inversely proportional to the local density of points, such that sparse sections of the signal are not underrepresented. This step is necessary because the data might not be evenly spaced in z.

Statistically, the bias-variance tradeoff is quantified by the statistical risk, $\mathcal{R}$. In the present case, it measures the magnitude of the error made with the prediction, $f_i(\boldsymbol{x})$, of s_i. The goal is to choose a window length that minimizes the risk. It is calculated as the expectation value, $\mathcal{E}$, of the squared difference between true signal, s_i, and its prediction, $f_i(\boldsymbol{x})$,

$$\mathcal{R} = \mathcal{E}\left\{\frac{1}{N}\sum_{i=1}^{N}(f_i(\boldsymbol{x}) - s_i)^2\right\} .\tag{2.3}$$

As s_i is unknown, the risk cannot be calculated directly. Instead, it is estimated. Applying SURE to (2.3) simplifies it to (2.4) [65]. Here, $\mathcal{R}_i$ is the risk associated

to the approximation of each data point x_i and σ is standard deviation of the noise component w_i.

$$\mathcal{R}_i = \mathcal{E}\left\{f_i(\boldsymbol{x})^2 - 2f_i(\boldsymbol{x})x_i + 2\sigma^2\frac{\partial f_i(\boldsymbol{x})}{\partial x_i}\right\} + s_i^2 \tag{2.4}$$

While s_i still appears in this formula, it only takes the form of an additive constant. Because of this, for the goal of choosing a window length, L, which minimizes $\mathcal{R}_i$, it can be neglected.

The above described procedure quantifies the risk associated with an approximation $f_i(\boldsymbol{x})$ at z_i. In practice, however, the measurement points, z_i, are not evenly spaced. For fast Fourier transformations and Bayesian deconvolution evenly spaced data points are required. Because of this, the optimum polynomial that minimizes the risk, $\mathcal{R}_i$, is not evaluated at the logarithmic time value of x_i, i.e. z_i, but at a location nearby z_i'. The set of new logarithmic times has a constant spacing $\Delta z' = z_{i+1}' - z_i'$. Which number of points for the new grid, N_g, is optimal, is investigated below. A low number of points, N_g, reduces the computational cost, but possibly affects accuracy.

Based on (2.4), the optimum window length is chosen by searching for an L that minimizes $\mathcal{R}_i$. In practice, the search is limited to an interval, $L \in [L_-, L_+]$, within reasonable bounds. Freely choosing L at each z_i' often leads to an oscillating behavior, i.e., additional high frequency noise in the output. Because of this, the initial window length L_0 at z_0' is freely chosen in the interval $[L_-, L_+]$ and then incremented or decremented by ΔL in every subsequent step. This means, that at each z_i' the risks associated with the window lengths $L - \Delta L$, L, and $L + \Delta L$ are calculated and the window lengths adjusted accordingly. This also greatly reduces the calculation time. Appropriately choosing the values for the parameters introduced in this paragraph is critical for accurate approximation.

In this way, interpolating the data to an evenly spaced grid, damping the noise, and calculating the derivative are all performed in a single step.

2.1.3 Deconvolution

For Bayesian deconvolution, the prior probability distribution is chosen to be equal to the impulse response, $h(z)$. With an increasing number of iterations, values in some regions of the spectrum will converge to zero and eventually underflow numerical double precision. Although this is not directly an issue, it reduces the number of non-zero points that make up the spectrum. Furthermore, for wide spectra this can lead to division-by-zero errors in (1.92). To avoid this, the algorithm accounts for zeros in the denominator, $\sum_j W_{kj} R_j^{(n)}$.

For the Fourier transformation, which is calculated with a fast Fourier transformation, depending on the shape of the spectrum, padding the impulse response with zeros before deconvolution is necessary [68]. In Fourier space, the impulse response becomes a function of the logarithmic frequency, Φ.

As laid out in subsection 1.6.2, a frequency domain filer, $F[\Phi_i]$, is applied to each component, Φ_i, of the spectrum. Frequencies beyond a cut-off, Φ_c, are

suppressed, see (2.5). Frequencies between $-\Phi_c$ and Φ_c are damped according to the window function, F_{Window}, in question.

$$F[\Phi_i] = \begin{cases} 0 & \text{for} \quad |\Phi_i| > \Phi_c \\ F_{\text{Window}} & \text{for} \quad |\Phi_i| \leq \Phi_c \end{cases} \tag{2.5}$$

For the window function, many forms are possible, a selection of which is evaluated in this work [85]. In particular, this includes the Gauss window and the Fermi filter as their use is reported in the literature, see Subsection 1.6.2. Additionally, the Hann window, rectangular window, and Nuttall window are applied, following the definitions below.

The support of the filter, i. e. the non-zero components, forms an array with N_W entries, which are here numbered from zero to N_W, from negative to positive frequencies, $n = 0, 1, \ldots, N_W$. For every window function, the width of the window is controlled via Φ_c and appears in the form of N_W in the definitions below. The Nuttall window is defined as a sum of cosines with specific numerical prefactors [86],

$$F_{\text{Nuttall}}[n] = 0.355\,768 - 0.487\,396 \cdot \cos\left(\frac{2\pi n}{N_W}\right)$$

$$+ 0.144\,232 \cdot \cos\left(\frac{2\pi n}{N_W}\right) - 0.012\,604 \cdot \cos\left(\frac{2\pi n}{N_W}\right). \tag{2.6}$$

Similarly, the Hann window takes the form of a squared sine function

$$F_{\text{Hann}}[n] = \sin^2\left(\frac{\pi n}{N_W}\right). \tag{2.7}$$

The rectangular window is simply

$$F_{\text{Rectangular}}[n] = 1. \tag{2.8}$$

The Gauss window has an additional parameter, σ, that is restricted to $\sigma \leq 0.5$. Within these bounds an appropriate value has to be chosen.

$$F_{\text{Gauss}}[n] = \exp\left(-\frac{1}{2}\left(\frac{n - N_W/2}{\sigma\, N_W/2}\right)^2\right) \tag{2.9}$$

The Fermi window is a special case as it does not use a finite cut-off frequency, Φ_c. Instead, it uses two parameters, μ and β, that control its width and slope. The support is the entire spectrum. The right-hand side is more stable for small values of β.

$$F_{\text{Fermi}}[n] = \frac{1}{\exp\left(\frac{|\Phi| - \mu}{\beta}\right) + 1} = \frac{\exp\left(-\frac{|\Phi| - \mu}{\beta}\right)}{1 + \exp\left(-\frac{|\Phi| - \mu}{\beta}\right)} \tag{2.10}$$

2.1.4 Foster-to-Cauer transformation

For the Foster-to-Cauer transformation, the polynomial long division approach is used. To guarantee sufficient accuracy for polynomials of high order, arbitrary floating point arithmetic with 1000 byte precision is used. To construct the Foster network from the time constant spectrum, the Foster resistances, R_i, and capacitances, C_i, are generated directly from each pair of ζ_i and $R(\zeta_i)$ in the spectrum via (1.75a) and (1.75b). When adding the terms according to (1.64), no additional sorting is conducted.

It is possible that in the result of a Fourier deconvolution the time constant spectrum, $R(\zeta)$, comprises negative values in some sections. This effect is more pronounced with wide filters, which let through a larger proportion of high-frequency components. For Bayesian deconvolution, the spectrum often contains values that are exactly zero or very close to it. To obtain an impedance, $Z(s)$, from the spectrum, it is necessary to treat these sections and guarantee a physical time constant spectrum in all cases. Parts of the spectrum which have no significant contribution are neglected. In this way, the input values for the Foster-to-Cauer transformation are normalized and the degrees of the polynomials involved are reduced, which increases numerical stability and accuracy. All resistances in the spectrum, below a certain threshold R_{min} are set to zero and hence do not generate pairs of Foster resistances and capacitances, (R_i, C_i). Here, the cut-off is set to $R_{min} = 10^{-20}$.

2.1.5 Inverse calculation

An inverse calculation means to derive a step response from a structure function. To construct an impedance, $Z(s)$, from a structure function, one has to rely on a piecewise uniform approximation, as discussed in Subsection 1.3.3.

Some algebraic manipulations of (1.44) reveal that it is sufficient to provide the total resistance, R, and capacitance, C, of each segment instead of resistance and capacitance densities, r and c, together with the length of the segment, Δx. Additionally, reformulating (1.44) to use a $\tanh(x)$ makes it numerically more stable. Putting all this together, the resulting iteration formula reads

$$Z_{in}(s) = \sqrt{\frac{R}{sC}} \; \frac{Z_L + \sqrt{\frac{R}{sC}} \; \tanh\left(\sqrt{sRC}\right)}{\sqrt{\frac{R}{sC}} + Z_L \; \tanh\left(\sqrt{sRC}\right)} \, . \tag{2.11}$$

Here, the complex frequency, s, is slightly rotated into the complex plain by an angle, δ, according to (1.77). However, small angles of δ require a dense sampling of the complex frequency, s, to capture narrow peaks in the time constant spectrum correctly. The smaller δ is, the more the peaks in the spectrum of time constants resemble Dirac delta functions. Moreover, for accurate calculations, it is required to capture even small contributions of the time constant spectrum accurately. This means, that for small angles of δ the time constant spectrum has to sampled densely over wide range. Because of

this, calculating theoretical thermal impedances with high accuracy becomes quite time-consuming, requiring calculation time on the order of minutes.

2.2 Optimization-based network identification

In this section, an alternative method for solving the network identification problem is presented, called optimization-based network identification, which was developed as part of this work. The idea of this method is to find a structure function that has a thermal impedance matching well with the measured thermal impedance. In this way, a structure function belonging to the system is known by construction. The corresponding time constant spectrum can be readily calculated to arbitrary accuracy. Figure 2.1 shows a schematic of the optimization-based network identification.

Good initial values are essential for the success of an optimization-based network identification. One way to obtain initial values is to perform a network identification by deconvolution. The resulting structure functions usually consist
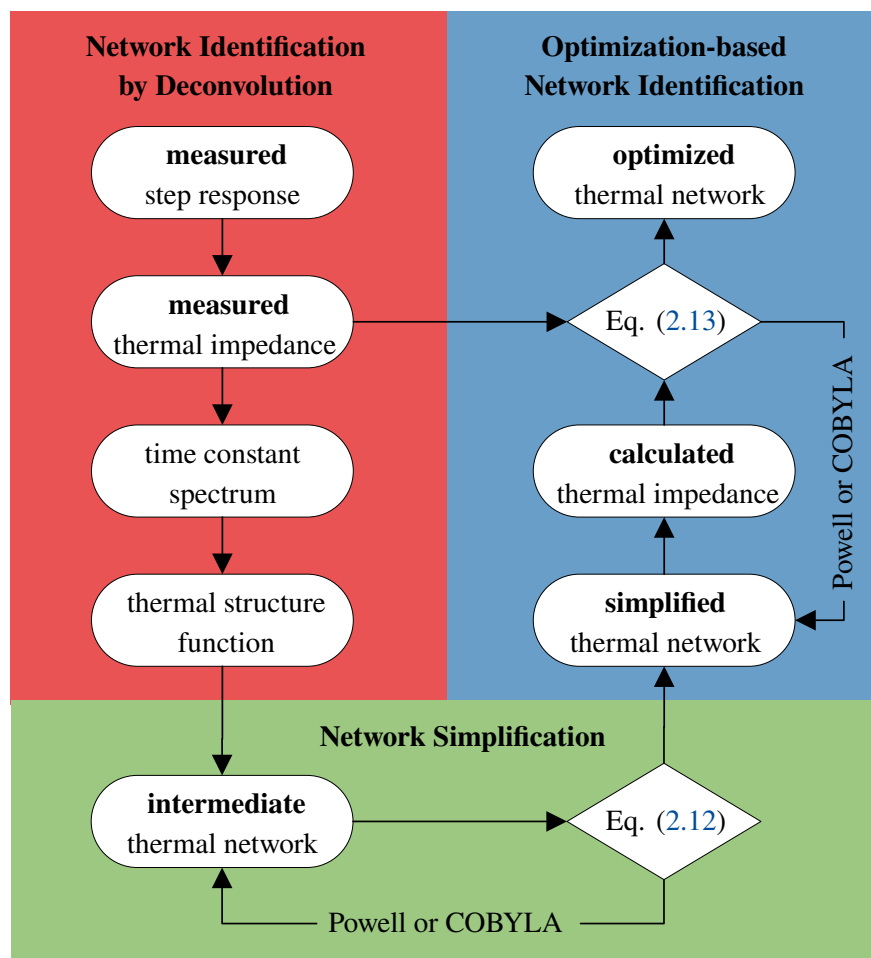
Figure 2.1: *Schematic for the optimization-based network identification. Starting from the measured step response, first, a network identification by deconvolution is performed. Then, the network simplification and optimization-based network identification follow.*
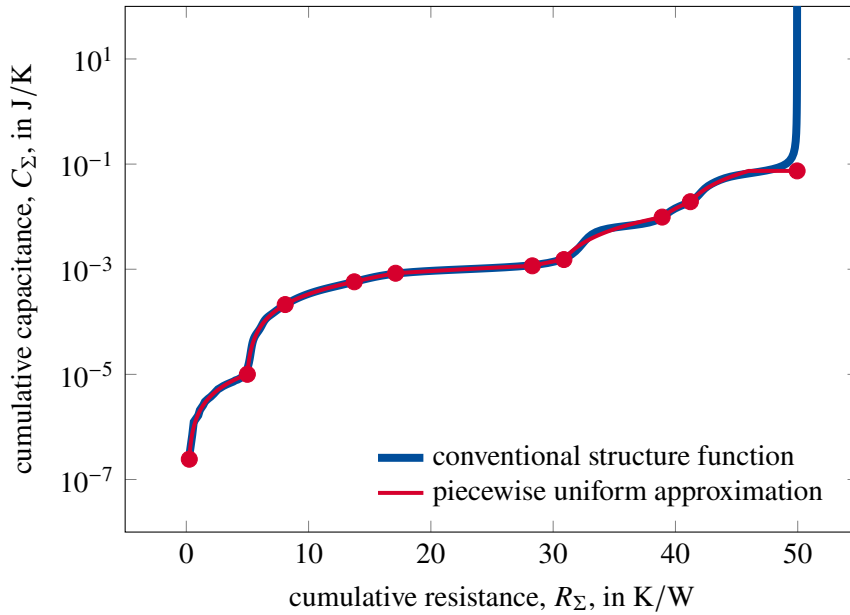
Figure 2.2: *Conventional cumulative structure function and piecewise uniform approximation with ten sections. The divergence at the end is truncated in the optimization.*

of several hundred data points. When performing an optimization using these thermal structure functions directly, several problems arise. For one, the search space during optimization is too large leading to lengthy computation times and suboptimal convergences. In addition, inverse calculations with several hundred sections are computationally too laborious to be used during an optimization.

Because of this, the number of degrees of freedom is reduced in the step of network simplification. Here, the thermal structure function is approximated with a piecewise uniform RC line, as shown in Figure 2.2. The relevant information is captured by a significantly reduced number of data points. For this step, the number of sections, N_S, in the piecewise uniform RC line must be defined manually. Typically, the number of sections that achieves a good fit and is computationally feasible lies between 2 and 20. Each section is completely defined by the total thermal resistance, R_i, and the thermal capacitance, C_i, it contributes to the structure function. Good initial values for the optimization-based network identification consist of N_S resistances and capcitances, $(R_1, \ldots, R_{N_S}, C_1, \ldots, C_{N_S})$, which match the measured thermal impedance at least approximately. In addition, each point should contribute significantly to the outcome.

Finally, a multidimensional optimization is performed on the resistances and capacitances with the goal of minimizing the discrepancy between the measured thermal impedance and the thermal impedance belonging to the optimized structure function, which is here called the optimized thermal impedance. For a valid solution, it is important to ensure that the optimized thermal impedance is actually in good agreement with the measured data.

To guarantee a good fit of the piecewise uniform structure function, which provides the initial values for the main optimization, it is itself optimized to
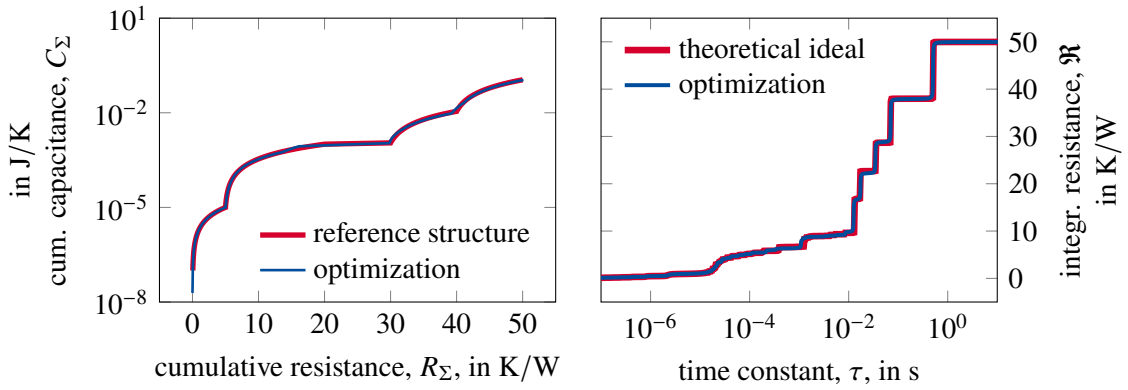
Figure 2.3: *Result of an optimization-based network identification (Powell) with ten sections. The initial values are generated with the help of a conventional network identification, see Figure* 2.2. *The measures of accuracy are* $m_R = 1.98\,\text{K/W}$ *and* $m_S = 2.06\,\text{K/W}$ *for structure* 1, *see Subsection* 2.3.1.

match closely with the thermal structure function, see Figure 2.1. For this initial value optimization, the objective function that performed best in practice is the square root of the integral of the squared logarithmic deviations,

$$o_{\text{struc}} = \sqrt{\int_0^R \left[\ln\big(C_{\Sigma,\text{conv}}(R_\Sigma)\big) - \ln\big(C_{\Sigma,\text{opt}}(R_\Sigma)\big)\right]^2 \, dR_\Sigma} \, . \qquad (2.12)$$

The initial values for the initial value optimization, $(R_{\Sigma,i}, C_{\Sigma,i})$, are evenly spaced along the arc length of the structure function. In addition, truncating the divergence at high R_Σ, which is a typical artifact of the Foster-to-Cauer transformation, has been shown to increase the accuracy and the stability of the convergence. To obtain a good fit, the overall thermal resistance represented by the initial values should match the measured thermal impedance.

The objective function employed for the main optimization is shown in (2.13). It has the form of an L^2-norm, i. e., it is the square root of the integral of the squared difference between optimized and measured step response,

$$o_{\text{imp}} = \sqrt{\int_{z_{\text{min}}}^{z_{\text{max}}} \big(a_{\text{measured}}(z) - a_{\text{opt}}(z)\big)^2 \, dz} \, . \qquad (2.13)$$

To compare the fit of the optimized thermal impedance with that of a conventional algorithm, a time constant spectrum which was computed via Fourier deconvolution or Bayesian deconvolution is reconvolved according to (1.73) and integrated to reproduce the thermal impedance it represents. Here, this impedance is called "backwards thermal impedance". To have a valid solution, the discrepancy between the optimized thermal impedance and the measured thermal impedance must be comparable to or smaller than the discrepancy between the optimized thermal impedance and a good backwards thermal impedance.

For the optimization shown exemplarily in Figures 2.2 and 2.3, the value of

the objective function resulting directly from the initial values, see Figure 2.2, is $o_{\mathrm{imp, initial}} = 1.0582\,\mathrm{K/W}$. After the main optimization, the value of the objective function is reduced, in this example, to $o_{\mathrm{imp, optimized}} = 0.0182\,\mathrm{K/W}$. For comparison, the value of the objective function for the backwards thermal impedance is $o_{\mathrm{imp, backwards}} = 0.0170\,\mathrm{K/W}$. Note that for the goal of calculating accurate structure functions, a low value of o_{imp} is an important sanity check and suitable to validate solutions. However, it is not a measure of the actual accuracy of the solution. Comparing the accuracy of various methods is the topic of Subsection 2.3.1.

For both optimizations, the actual degrees of freedom provided to the solver are the *cummulative* resistances and *cummulative* capcitances of the piecewise uniform structure function, $(R_{\Sigma,1}, \ldots, R_{\Sigma,N_{\mathrm{S}}}, C_{\Sigma,1}, \ldots, C_{\Sigma,N_{\mathrm{S}}})$. In each function evaluation, an inverse calculation is performed as described in Subsection 2.1.5. As a physical constraint, it is demanded that the structure function is a monotonically increasing function. This means that the list of resistances, $(R_{\Sigma,1}, \ldots, R_{\Sigma,N_{\mathrm{S}}})$, and capacitances, $(C_{\Sigma,1}, \ldots, C_{\Sigma,N_{\mathrm{S}}})$, should be strictly monotonically increasing, i. e., each $R_{\Sigma,i}$ and $C_{\Sigma,i}$ are greater than their left neighbor and smaller than their right neighbor. However, during the optimization the solvers cannot be relied on to uphold this condition. Because of that, there is a mechanism to repair unphysical structure functions that appear during the optimization. A problem arises, for example, if the solver modifies the resistance of one data point, $(R_{\Sigma,i}, C_{\Sigma,i})$, such that its resistance comes close to or exceeds the resistance of a neighboring data point, $(R_{\Sigma,i+1}, C_{\Sigma,i+1})$. Here, the conflict is solved by sorting the $R_{\Sigma,i}$ and $C_{\Sigma,i}$ independently before each function evaluation. This corresponds to virtually moving the resistance of the other data point, once the data points have the same resistance, $R_{\Sigma,i} = R_{\Sigma,i+1}$. This is a difference because of the associated thermal capacitances, which are not equal in general, $C_{\Sigma,i} \neq C_{\Sigma,i+1}$. Additionally, a minimum size for $R_{\Sigma,i} - R_{\Sigma,i+1}$ and $C_{\Sigma,i} - C_{\Sigma,i+1}$ is set to avoid numerical instability.

For the purpose of the actual optimization, two solvers yield good results. The first is Powell's conjugate direction method [87]. As a second method, Constrained Optimization BY Linear Approximations, abbreviated COBYLA, is also suitable [88]. A common feature of both solvers is that they do not calculate derivatives of the objective function. This makes them particularly suitable for problems with a complicated objective function and problems where the derivative is not directly available.

Moreover, both solvers are able to respect boundary conditions which is used to limit the search space to physically plausible values, such as the restriction to cumulative resistances and capacitances. The total thermal resistance, $R_{\mathrm{th},\Sigma}$, is unlikely to significantly exceed $Z_{\mathrm{th}}(t \to \infty)$. In addition, the COBYLA solver is able to accept relative constraints, which is used to force the parameters to remain in certain bounds. This is used to restrict the parameters to always remain sorted in the sense explained above. Still, physicality should be checked at every function evaluation because of possible constraint violations. Furthermore, significant speed increases are achieved in calculations of (2.11) by using an LRU (Least Recently Used) cache. In summary, the Powell solver has been

shown in practice to be faster, but less reliable because it fails to converge on rare occasions. The COBYLA solver is slower but more stable due to more stringent constraints. The accuracy is similar for both methods, possibly slightly better for the Powell solver as is analyzed in the following section.

2.3 Performance comparison

2.3.1 Methodology

The purpose of this section is to systematically compare the accuracy of different methods to perform a network identification. The methods examined here are network identification via Fourier deconvolution as well as Bayesian deconvolution, and the optimization-based network identification as presented in the previous section. Moreover, the influence of parameters appearing in these algorithms is systematically analyzed, such as the window length increment, ΔL, or the number of points in the derivative, N_g, which were introduced in the subsection 2.1.2.

For this purpose, three test structures are defined via the thermal resistances and capacitances of their piecewise uniform structure functions as summarized in Table 2.1. The theoretical thermal impedances are constructed using (2.11). The thermal resistances and capacitances are chosen to be roughly similar to real electronic devices of varying complexity. While the time constant spectrum of structure 3 consists essentially of a single peak and has only three sections, structure 1 includes many smaller and larger peaks resulting from five sections. An illustration of the corresponding structure functions as well as their time constant spectra, impulse responses, and thermal impedances is given in Figure 2.4.

The basic principle for comparing the accuracy of the different methods of network identification is to derive the theoretical thermal impedances of the structures with high accuracy and then use them as input for a network identification. The difference between the original and the recovered time

Table 2.1: *For the purpose of comparison, three test structures are defined as piecewise uniform structure functions. The total thermal resistances (in* K/W*) and the total capacitances (in* J/K*) of each section are given below.*

|	STRUCTURE 1		STRUCTURE 2		STRUCTURE 3	
SECTIONS	R_th	C_th	R_th	C_th	R_th	C_th
Section 1	5	10^{-5}	10	10^{-4}	20	10^{-1}
Section 2	15	10^{-3}	10	10^{-1}	20	10^{-4}
Section 3	10	10^{-4}	10	10^{-4}	10	10^{-3}
Section 4	10	10^{-2}	10	10^{-3}	-	-
Section 5	10	10^{-1}	10	10^{0}	-	-
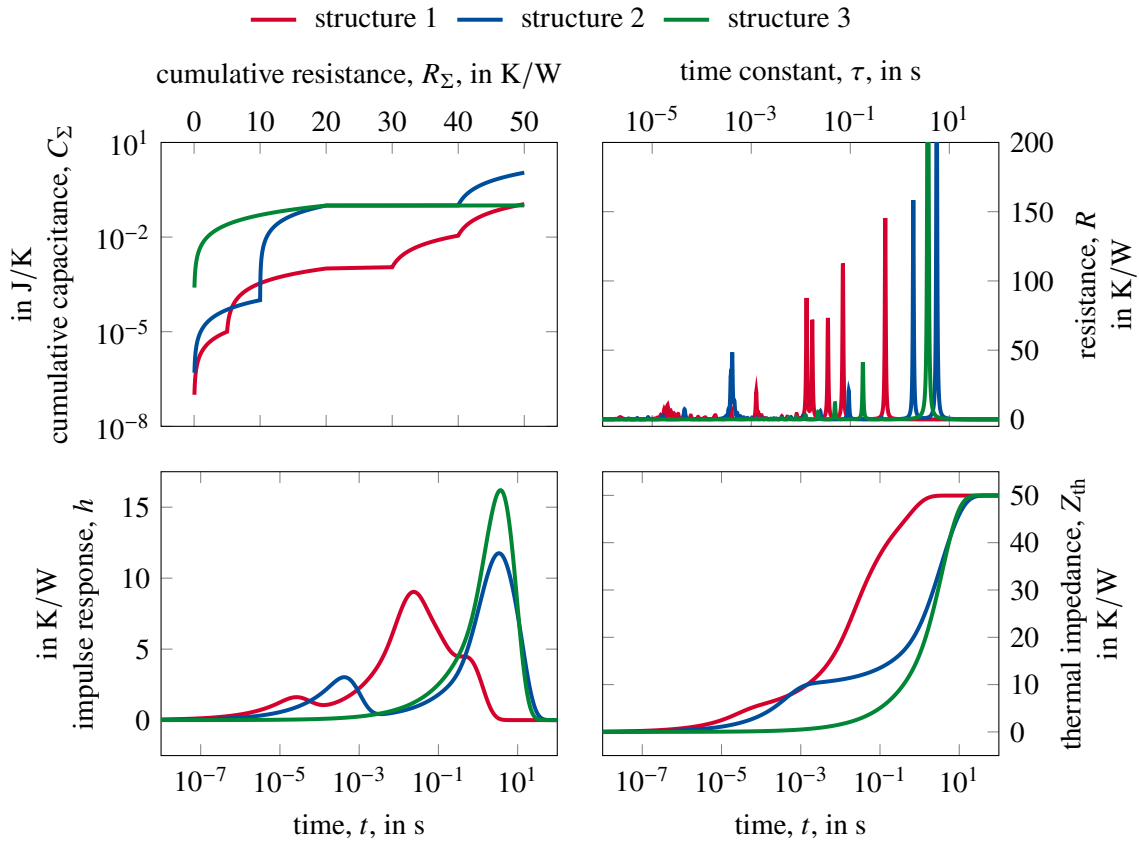
Figure 2.4: *Overview over the three test structure functions (top left), their respective time constant spectra (top right), impulse response (bottom left), and thermal impedance (bottom right) calculated at $\delta = 0.03°$. For the purpose of readability, the time constant spectra plotted are calculated with $\delta = 1.5°$.*

constant spectrum and the structure function gives a measure of the accuracy of the respective method. To simulate realistic measurement data, the exact theoretical thermal impedance is obscured by adding white noise and interpolated to simulate a constant sampling rate in linear time, t. In this way, the performance of the algorithms is studied under non-ideal conditions.

To avoid a systematic bias in the calculation, a high accuracy for the theoretically calculated functions must be ensured. For this reason, the first step is to investigate how large the error associated with the calculation of the theoretical thermal impedance is.

Because of the poles in $Z(s)$ on the negative real axis, a small angle δ must be introduced as described in (1.77). However, this leads to a small systematic error in the calculation that depends on the value of δ. While for smaller values of δ this kind of error decreases, simultaneously the peaks in the time constant spectrum become narrower. This increases the discretization error. To compensate for this, the sampling rate of ζ must be increased. For all following calculations, the logarithmic time constant, ζ, is evenly spaced using

$$\zeta \in [-20, 10] \quad \text{with} \quad N_\zeta = 10^6 , \tag{2.14}$$
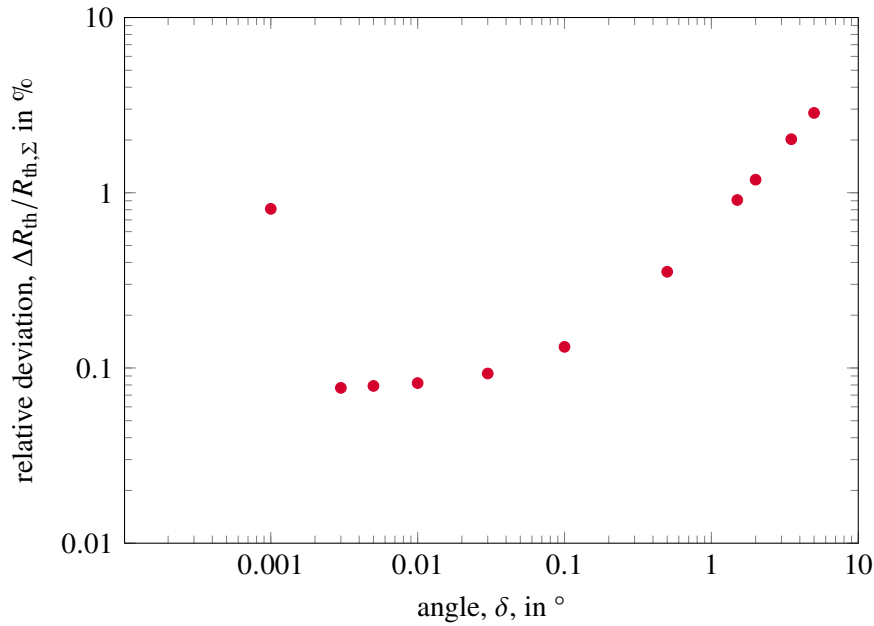
Figure 2.5: *Relative deviation between expected and observed thermal resistance for structure* 1 *at various values of δ and fixed sampling rate* (2.14).

where N_ζ is the number of points in the interval. This sampling rate corresponds to approximately 75 000 points per decade. This increases the computation time of a theoretical thermal impedance to several minutes on an average desktop PC for the implementation used in this work.

All three test structures defined above have a total thermal resistance of exactly $R_{\text{th},\Sigma} = 50$. Ideally, the theoretical thermal impedance should exactly match this value by satisfying the relation $R_{\text{th},\Sigma} = Z_{\text{th}}(t \to \infty)$. However, due to the discretization error and the finite angle δ, in practice $Z_{\text{th}}(t \to \infty)$ is smaller than $R_{\text{th},\Sigma}$. The difference is denoted as ΔR_{th},

$$\Delta R_{\text{th}} = |R_{\text{th},\Sigma} - Z_{\text{th}}(t \to \infty)| . \tag{2.15}$$

Figure 2.5 shows the relative deviation, $\Delta R_{\text{th}}/R_{\text{th},\Sigma}$, as a function of δ at a fixed sampling rate. At large angles, the rotated integration path causes a significant deviation in thermal resistance. For lower angles, the error is reduced before at very low angles the error increases again. At this point, the peaks in the time constant spectrum become so narrow that the sampling rate is insufficient to capture them correctly. To further reduce the error, a wider interval and a more dense sampling have to be used, which requires significantly more computation

Table 2.2: *Relative difference between expected and observed thermal resistance averaged over structure* 1 *to* 3 *at various values of δ and fixed sampling rate* (2.14).

Angle δ	5.00°	3.50°	2.00°	1.50°	0.50°	0.10°	0.03°
Deviation $\Delta R_{\text{th}}/R_{\text{th},\Sigma}$	2.82 %	1.98 %	1.15 %	0.87 %	0.32 %	0.09 %	0.05 %

time. Table 2.2 shows the values of $\Delta R_{\text{th}} / R_{\text{th},\Sigma}$ averaged over the three test structures for different values of δ. A comparison with Figure 2.5 shows that the error depends on the shape of the spectrum. To guarantee a sufficiently dense sampling in all cases, an angle of $\delta = 0.03°$ and a sampling of (2.14) is used for the most accurate calculations.

When assessing the absolute accuracy of a solution computed via a network identification procedure, the measure of accuracy needs to be defined with great care. The goal is to find two suitable functionals, one for measuring the accuracy of the time constant spectrum and one for the structure function. These should adequately measure the degree of similarity between the theoretical ideal and a given solution. While there is not one objectively correct way to quantify this, the following definitions have proven to be reliable and robust in extensive testing and have provided results that generally agree well with intuition. In the following, the reasoning that led to these definitions is explained.

First, the measure of accuracy for the time constant spectrum is presented. One challenge in comparing two different time constant spectra is the narrowness of the peaks. For example, it is not sufficient to directly integrate the difference of two sharply peaked time constant spectra, say via an L^2-norm. The sharpness of the peaks makes the overlap between two adjacent peaks is small, and once two peaks are completely separated, the relative distance would not be taken into account. Moreover, for theoretically calculated time constant spectra, the height of the peaks depends on the value of δ, which would make the absolute accuracy also depend on δ.

To avoid these issues, the integrated time constant spectrum, $\mathfrak{R}(\zeta)$, is considered instead.

$$\mathfrak{R}(\zeta) = \int_{-\infty}^{\zeta} R(\zeta') \ \mathrm{d}\zeta' \tag{2.16}$$

In this form, the delta-function-like peaks of a theoretical time constant spectrum become a stair function that is asymptotically independent of delta. Moreover, the use of $\mathfrak{R}(\zeta)$ correctly accounts for the area under the curve. This is particularly important for the time constant spectrum, since the area under the curve is proportional to the total resistance of the structure.

The measure of accuracy for the time constant spectrum m_{R} thus has the form of an L^2-norm of the difference between the integrated ideal time constant spectrum, $\mathfrak{R}_{\text{ideal}}(\zeta)$, and reconstructed time constant spectrum, $\mathfrak{R}(\zeta)$.

$$m_{\text{R}} = \sqrt{\int_{-\infty}^{\infty} \left(\mathfrak{R}_{\text{ideal}}(\zeta) - \mathfrak{R}(\zeta)\right)^2 \ \mathrm{d}\zeta} \ . \tag{2.17}$$

Because the time constant spectra are equal to zero in the limit $\zeta \to \pm\infty$, the integration limits are set to infinity. An L^2-norm is chosen, as opposed to an absolute norm, to devalue larger differences disproportionately more than smaller ones. To calculate the difference, one of the time constant spectra is interpolated to match the other.

In practice, the use of m_{R} for time constant spectra computed via Fourier

deconvolution tends to rank oscillations in the spectrum due to noise better than one might intuitively expect. This is not the case for Bayesian deconvolution and optimization-based network identification, where a strictly positive spectrum is guaranteed by the algorithm.

For the structure function, $C_\Sigma(R_\Sigma)$, a more complex functional is necessary. This is mainly because of the following three challenges that arise when quantitatively comparing structure functions.

First, the cumulative thermal capacity, C_Σ, typically spans several orders of magnitude, see Figure 2.4. Thus, it is often plotted on a logarithmic scale.

Second, the structure function is constructed from the thermal resistances and capacities provided by the Foster-to-Cauer transformation. Consequently, no two structure functions will have the same set of $R_{\Sigma,i}$ it is defined on. Critically, this means that the starting and end points of two structure functions will not generally be the same. This means that either one structure function has to be extrapolated or the other has to be truncated.

This is particularly important because, third, structure functions calculated via Bayesian deconvolution or Fourier deconvolution typically feature a divergence at the end. While this is a real disadvantage of these methods that should be properly quantified, no meaningful difference is counted in keeping track of, whether the structure function ends at, for example, $C_{\Sigma,\text{max}} = 10^{15}$ or $C_{\Sigma,\text{max}} = 10^{50}$.

Given these challenges, the following measure of accuracy for the structure function, m_S, is defined,

$$m_S = \int_{R_{\Sigma,\text{min}}}^{R_{\Sigma,\text{max}}} \left| \ln\big(C_{\Sigma,\text{ideal}}(R_\Sigma)\big) - \ln(C_\Sigma(R_\Sigma)) \right| \, dR_\Sigma, \qquad (2.18)$$

where $C_{\Sigma,\text{ideal}}(R_\Sigma)$ is the ideal and $C_\Sigma(R_\Sigma)$ the reconstructed structure function. The logarithm is used to not overly emphasize deviations at high values of C_Σ. Also, for the structure function an L^1-norm is used as opposed to the L^2-norm used above. This is done to not disproportionately devalue a structure function with divergences. For the same reasons, all structure function are truncated at $C_\Sigma = 10^6$.

The integration limits $R_{\Sigma,\text{min}}$ and $R_{\Sigma,\text{max}}$ are defined as,

$$R_{\Sigma,\text{max}} = \arg\max(C_\Sigma), \qquad\qquad (2.19a)$$
$$R_{\Sigma,\text{min}} = \arg\min(C_{\Sigma,\text{ideal}}). \qquad\qquad (2.19b)$$

This means that on the left side the ideal structure function defines the limit and the recovered structure function is truncated or, as is almost always the case, extrapolated accordingly. On the right side the limit is defined by the recovered structure function. This is necessary, because extrapolating the divergence of the recovered structure function to match ideal structure function has too great an impact. Conversely, extrapolating the ideal structure function is not an issue. Also, truncating the recovered structure function when the ideal structure function ends puts a bias into m_S to favor later divergences in the recovered

structure function. To avoid these issues, the limits are defined as in (2.19a) and (2.19b).

Furthermore, note that this norm for structure functions differs from the other norm (2.12) used previously. This is, because (2.12) is used as part of an optimization, where has proved to be advantageous to disproportionately devalue larger deviations. Hence, a quadratic norm is used there.

However, measuring the accuracy of structure functions via (2.18) does mean that the absolute accuracy of the total thermal resistance is not reflected in m_S. This is because the upper integration limit is defined by the location of the divergence via (2.19a). Consequently, only the shape of the divergence is taken into account and not its relative location.

For these reasons, an additional, third, measure of accuracy is used to characterize the total resistance belonging to the recovered structure function. The difference in total resistance, ΔR_Σ, is calculated by comparing the theoretically expected resistance $R_{\Sigma,\mathrm{ideal,max}} = \arg\max(C_{\Sigma,\mathrm{ideal}})$ to $R_{\Sigma,\mathrm{max}}$ as defined in (2.19a),

$$\Delta R_\Sigma = |R_{\Sigma,\mathrm{ideal,max}} - R_{\Sigma,\mathrm{max}}| . \tag{2.20}$$

To gauge the robustness of the algorithms when confronted with real measurement data, Gaussian noise is added to the theoretically calculated thermal impedance in an additional step. The standard deviation, σ, of the noise is defined via the signal-to-noise ratio, R_{SN}, and the asymptotic value of the thermal impedance $Z_{\mathrm{th}}(t \to \infty)$ via

$$R_{\mathrm{SN}} = \frac{Z_{\mathrm{th}}(t \to \infty)}{\sigma} . \tag{2.21}$$

To have the results not depend on a single noise pattern, many realizations of the noisy thermal impedance are generated and solved. For all following calculations, 2000 randomly generated noisy thermal impedances are evaluated as recommended in [89]. As a result, the median over 2000 solutions is calculated and compared via the measures of accuracy (2.17), (2.18), and (2.20).

For the impulse response, the pointwise median can be calculated directly, as all discrete z-values the solutions are defined on are identical. To guarantee identical domains for the structure functions, each solution is interpolated or extrapolated as far as necessary. These normalized structure functions are then averaged by calculating the median point by point. Finally, the divergence of the median structure function is truncated similarly to above.

The time constant spectrum, however, cannot be averaged directly, because the result would be highly biased towards zero. Because of this, first the integrated time constant spectrum is computed for each realization. The set of resulting integrated time constant spectra is then averaged. For the sake of accuracy comparisons, this is acceptable since only integrated time constant spectra are compared anyway.

To gain a measure of the width of the distribution of the solutions, confidence intervals are calculated. For these calculations, the set of solutions is prepared

identically as for the computations of the medians. Then, a confidence interval is calculated using the percentile method as described in [89]. This means that for each x value, the lowest 10 % and the highest 10 % of all y values are discarded. The remaining difference from the highest to the lowest value forms the 80 % confidence interval.

The Gaussian distributed random numbers are generated via the default random number generator available in numpy 1.19.2. To guarantee repeatability, for each of the 2000 realizations an individual fixed seed is used. In this way, repeated calculations with different parameters use the identical noise patterns, for instance the same calculation with two different signal-to-noise ratios, albeit with a different standard deviation. In any case, averaging over 2000 repetitions makes the median almost completely independent of a particular noise pattern.

In the above described case, the independent realizations of the noisy thermal impedance are directly available. When the theoretical solution is not known, for example when using real measurement data, bootstrap resampling is a way to generate additional realizations [89]. An approximation of the exact thermal impedance is calculated via optimal regression filtering as described in Subsection 2.1.2. Then, an equivalent realization, a bootstrap sample, is generated by resampling the residuals around the approximation of the exact thermal impedance. In this way, confidence intervals around structure functions based on measurement data can be calculated.

2.3.2 Performance for perfect data

In this subsection, the accuracy of reconstructed time constant spectra and structure functions is investigated. The latter are obtained from network identification with Bayesian deconvolution, Fourier deconvolution, or optimization-based network identification. As artificial measurement data, the exact thermal impedances belonging to structures 1 to 3, defined in Table 2.1, are used. These impedances have a sampling rate of approximately 75 000 points per decade and a relative error in R_{th} of approximately 0.05 %. The recovered solutions are compared to the theoretically ideal values using the accuracy measures m_{R}, m_{S}, and ΔR_{Σ} as defined in (2.17), (2.18), and (2.20).

There are several parameters such as the window length increment, ΔL, or the number of points in the derivative, N_{g}, which have to be specified to fully define the algorithm. For some of these variables, accurate tuning is crucial to guarantee good performance. An obvious example is the cut-off frequency, Φ_{c}, which determines the width of the filter in Fourier deconvolution. Other parameters, such as N_{g}, prove to have little effect on the result beyond a certain point. Nevertheless, for a fair comparison between the methods, it is important to set these parameters to the same values wherever possible.

However, for some parameters, particularly for the cut-off frequency, Φ_{c}, it is not possible to define a universally good value. In these cases, suitable values must be chosen individually for each evaluation. In fact, the optimal choice for Φ_{c} also depends on which accuracy measure one focuses. In general, the minima of m_{R}, m_{S} or ΔR_{Σ} are found at different values of Φ_{c}, respectively. In
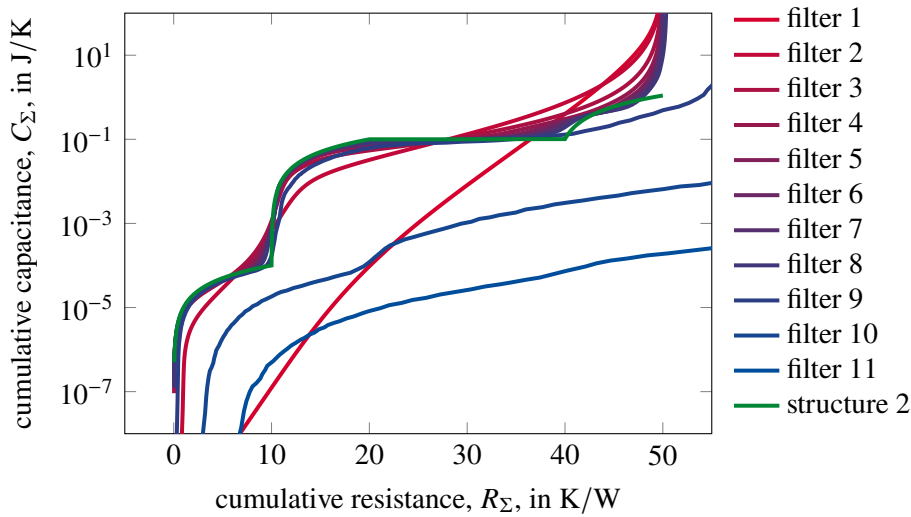
**Figure 2.6:** *Various trials for the cut-off frequency, Φ_c, in a network identification using a Gauss filter (2.9) for a fixed value of σ. Filter 1 is too narrow and Filter 11 is too wide. Additionally, the ideal theoretical result for structure 2 is shown.*

practice, it has been shown that m_S and ΔR_Σ usually show similar behavior. For this reason, only accuracies for m_S and m_R are shown below.

To illustrate the dependence of the result on the filter configuration, Figure 2.6 compares the theoretically ideal structure function for structure 2 with different solution attempts. Here, several solutions computed with the help of a Gaussian filter, see (2.9), using increasing values of Φ_c and fixed σ are plotted. Filter 1 is too narrow, leading to a significant loss of information in the result, while filter 11 is chosen too wide, with the consequence that residual noise components are greatly amplified and the total resistance is overestimated considerably. The best result is obtained by one of the filters in the middle.

However, the best of the filters shown in Figure 2.6 may not represent the actual optimum cut-off frequency with respect to m_S. It is likely that the optimum value for Φ_c lies somewhere between two filters, such that a finer resolution of the search space would yield an even better result. However, using a filter, which is merely *good*, gives a more realistic impression of the accuracy of Fourier deconvolution that is achievable in practice. This is because when confronted with real measured data, it is impossible to find the best filter since the optimum is unknown.

For the Fermi filter, (2.10), and the Gaussian filter, (2.9), it is much more difficult to find a good filter configuration because these filters depend on two parameters. This makes the search for the filer a two-dimensional optimization problem. In practice, there is no observable gain in accuracy to counterbalance this. Conversely, the Nuttall, Hann, and rectangular filters depend only on Φ_c.

To determine suitable filter configurations for all calculations in the following, a linear search analogous to the one shown in Figure 2.6 is performed for all tested filters, namely the Fermi, Gaussian, Nuttall, Hann, and rectangular filters. This procedure is repeated for each of the three test structures and both accuracy measures, m_R and m_S.
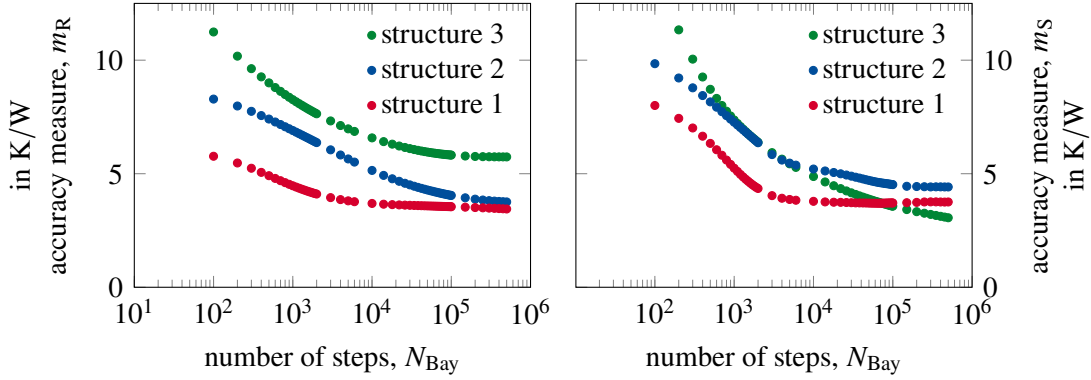
Figure 2.7: *Accuracy of the time constant spectrum, m_R, and structure function, m_S, as a function of number of steps in the Bayesian deconvolution for the three test structures. The number of points is set to $N_g = 250$.*

For all calculations presented in this subsection, this includes the ones using the Bayesian deconvolution and Fourier deconvolution as well as optimization-based network identification, the configuration (2.22) is used. In the following the process how these parameters have been determined is laid out. In the presence of noise, different parameters should be chosen.

$$
\begin{aligned}
L_- &= 0.05 & L_+ &= 3.00 \\
\Delta L &= 0.10 & N_g &= 250 \\
N_{Bay} &= 5 \times 10^5
\end{aligned}
\tag{2.22}
$$

The window length, L, is measured in logarithmic time, z. This means a window of size $L = 3.0$ corresponds to an interval of size $\Delta z = 3.0$ in the logarithmic time. The starting window length is automatically chosen by the algorithm. For Bayesian deconvolution, the number of steps is denoted as N_{Bay}.

Although Bayesian deconvolution also has a tunable parameter, namely the number of iterations, it is easier to handle than Fourier deconvolution. To determine what number of steps is appropriate for Bayesian deconvolution, a series of tests is performed. The results are shown in Figure 2.7. The number of steps spans several orders of magnitude from 10^2 to 5×10^5. While the accuracy increases in all cases, the rate of convergence depends significantly on the structure function. For structure 3, convergence for m_S is not achieved even after 5×10^5 steps. Nevertheless, $N_{Bay} = 5 \times 10^5$ minimizes m_S and m_R for all structures. However, using even more steps would give better results at the price of increased computation time. The computation time and accuracy for Bayesian deconvolution depends not only on the number of steps, but also on the number of data points, N_g, since this determines the size of the matrices involved. For the calculations shown in Figure 2.7, the number of points was set to $N_g = 250$. In this case, deconvolution with $O(10^5)$ steps takes several seconds.

Besides the process of deconvolution, derivation is also an important factor affecting the overall accuracy. There are a total of four important parameters that must be specified when using the optimal regression filtering as described
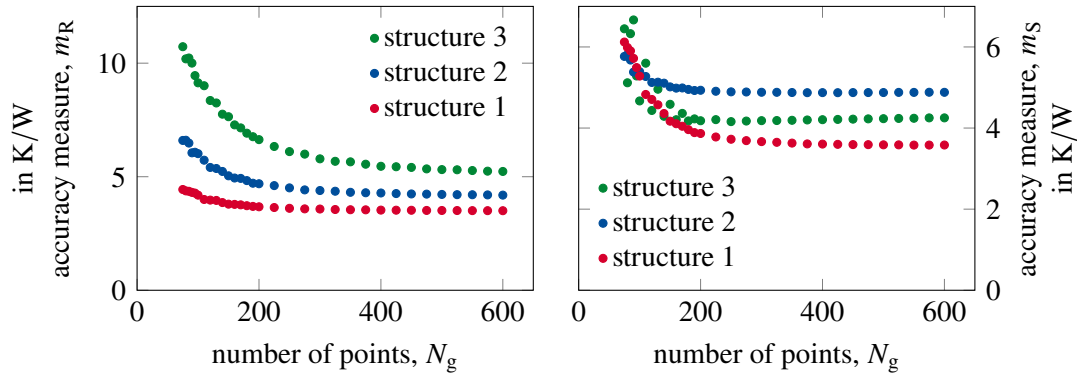
Figure 2.8: *Accuracy of the time constant spectrum and structure function as a function of the number of data points in the derivative for the Bayesian deconvolution. The number of steps is set to 3×10^4.*

in Subsection 2.1.2. Explicitly, these are the minimum window length L_-, the maximum window length L_+, the window length increment ΔL, and the number of steps N_g. To show the dependence of the solution on the number of points, N_g, for Bayesian deconvolution, another comparison is made. The results are plotted in Figure 2.8. The accuracy benefit from an increasing number of points drops off rapidly for $N_g \gtrsim 200$, for both the structure function and the time constant spectrum. Due to the steeply increasing computation time with increasing N_g, the number of points is set to $N_g = 250$. The number of steps belonging to the calculations in Figure 2.8 is set to 3×10^4.

For optimization-based network identification, more parameters have to be set. To provide initial values, a network identification using Bayesian deconvolution is also performed in the context of the optimization-based network identification. For this, the identical configuration as above is used. As far as the actual optimization is concerned, the tunable parameters include termination and convergence criteria for the iteration such as the maximum number of iterations, the acceptable relative error in $(R_{\Sigma,1}, \ldots, R_{\Sigma,N_S}, C_{\Sigma,1}, \ldots, C_{\Sigma,N_S})$, and the acceptable relative error in the objective function, o_{imp}, see (2.13). For the COBYLA solver, a tolerance for constraint violations must be set. A robust configuration was found for these parameters, which will be used in the following. Finally, the accuracy also depends on the number of piecewise uniform sections set for the approximation. For this parameter, the optimum value was found for each test structure. Due to the number of inverse calculations required to perform an optimization-based network identification each thermal impedance has to be calculated with reduced accuracy. In these inverse calculations, an angle of $\delta = 0.5°$ with 10^4 points for $\zeta \in [-20, 10]$ is used, which corresponds to approximately 750 points per decade.

Table 2.3 summarizes the performance metrics for all tested structures and methods. For the calculations, all parameters and tuneable values are kept identical regardless of method and test case. An exception to this is the cut-off frequency, Φ_c, which must be set separately for all cases. For this purpose, a number of filter configurations are tested and the best one is selected in the sense explained in Figure 2.6, which means that a different filter is used for each

structure and both accuracy measures, m_S and m_R. The respective performances are compiled in Table 2.3.

For the results presented in Table 2.3, the method with the best performance for each accuracy measure and structure is highlighted in bold and the second best result is underlined. In terms of m_S and m_R, optimization-based network identification with a Powell solver performs best for all test structures, while the second-best result is consistently obtained by optimization-based network identification with a COBYLA solver. The best resistance accuracy, ΔR_Σ, is achieved in all cases by network identification with a Bayesian deconvolution.

A comparison of filter choices used in Fourier deconvolution shows mixed results. Although there is no clear winner that performs best on every metric, the Hann filter stands out because it performs best or second best on m_S and m_R for all structures. In addition, the Hann filter has only a single adjustable parameter. As expected, a rectangular filter is not recommended.

There is a clear trend in the computational difficulty among the three structures tested. For almost all methods, the calculation of structure 1 gives the most accurate results, although the shape of its thermal structure function, time constant spectrum, and impulse response seems to be more complex than that of structure 3, which gives the least accurate results even though it includes only three sections, compare Figure 2.4 and Table 2.1.

For Bayesian deconvolution, convergence is achieved at much higher steps than discussed in the literature, which suggests the use of about 1000 steps, compare Subsection 1.6.2. However, according to the results depicted in Figure 2.7 it seems appropriate to use up to 10^5 iteration steps or even more.

Table 2.3: *Best accuracy for all methods in the absence of noise in units of* K/W. *The best performing method in each column is highlighted in bold, the second best result is underlined. The methods "Fermi", "Gauss", "Nuttall", "Hann", and "Rectangular" denote the window functions, F_{Window} as defined in* (2.5). *The methods "Powell" and "COBYLA" refer to two choices for the solver in optimization-based network identification. The measures of accuracy are defined in* (2.17), (2.18), *and* (2.20).

METHOD	STRUCTURE 1			STRUCTURE 2			STRUCTURE 3		
	m_R	m_S	ΔR_Σ	m_R	m_S	ΔR_Σ	m_R	m_S	ΔR_Σ
Fermi	4.7	7.7	<u>0.06</u>	5.8	9.6	0.91	8.1	16.3	2.91
Gauss	5.1	8.9	0.08	7.6	9.4	0.27	9.3	13.8	<u>0.09</u>
Nuttall	4.7	8.2	0.12	6.8	8.5	0.38	10.0	11.5	0.15
Hann	4.4	7.4	0.28	6.3	7.5	0.44	8.9	10.8	0.91
Rectangular	4.0	38.7	6.94	5.4	41.4	6.31	7.6	129	31.08
Bayesian	3.4	3.7	**0.04**	3.8	4.4	**0.02**	5.7	3.1	**0.01**
Powell	**1.2**	**1.2**	0.13	**2.0**	**1.3**	<u>0.14</u>	**2.4**	**1.8**	0.15
COBYLA	<u>1.5</u>	<u>2.0</u>	0.13	<u>2.4</u>	<u>2.6</u>	<u>0.14</u>	<u>2.5</u>	<u>1.9</u>	0.14
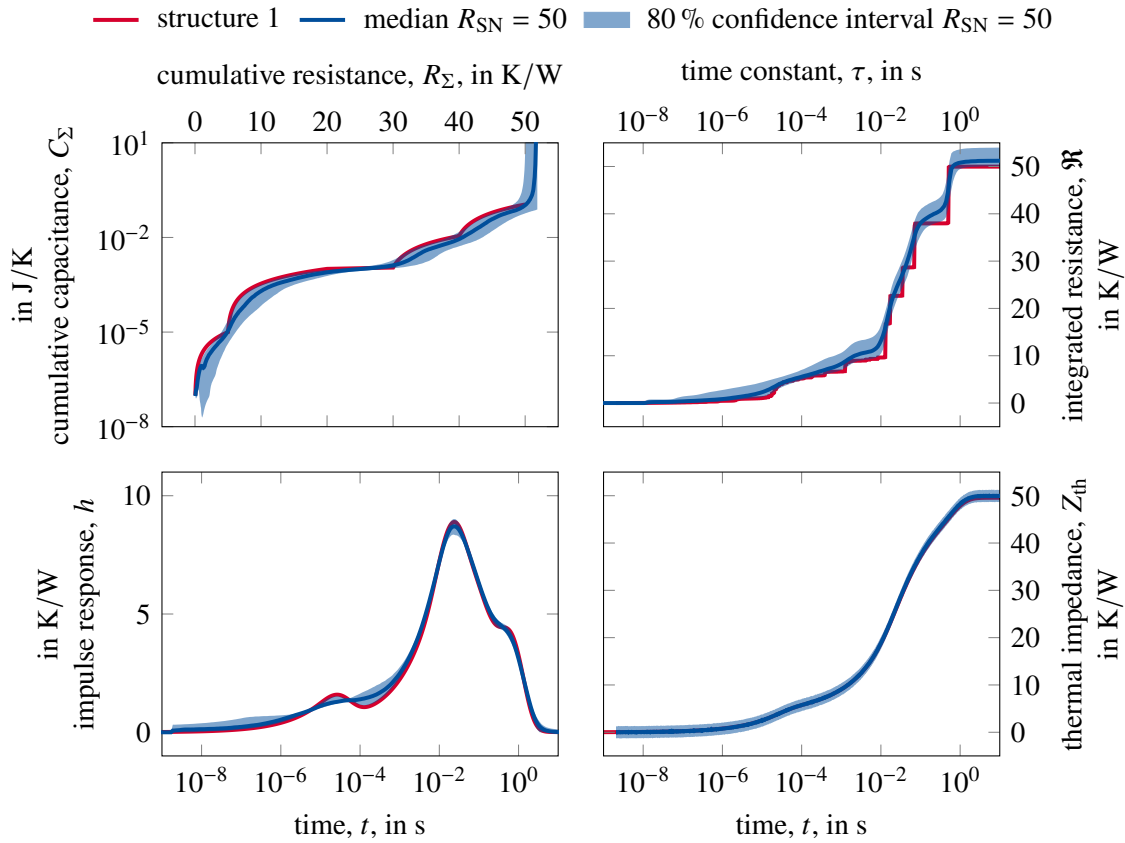
Figure 2.9: *Median solution and* 80 % *confidence intervals for structure* 1 *recovered by Bayesian deconvolution. Thermal structure function* (*top left*), *time constant spectrum* (*top right*), *impulse response* (*bottom left*), *and thermal impedance* (*bottom right*) *for a signal-to-noise ratio of* $R_{SN} = 50$ *calculated from* 2000 *noise realizations.*

2.3.3 Performance in presence of noise

In this subsection, the performance of selected methods in the presence of different levels of noise is analyzed. To that end, Gaussian noise is added to the exact thermal impedance. From the noisy thermal impedance, the structure function and integrated time constant spectrum are calculated. As the result, the pointwise median corresponding to 2000 independent noise distributions is calculated. For details concerning the averaging process, the reader is referred to the end of Subsection 2.3.1.

In addition to introducing noise into the thermal impedance, the sampling rate is reduced to approximately 90 points per decade. This is achieved by interpolating the exact thermal impedance. The standard deviation of the added noise is calculated from the signal-to-noise ratio, R_{SN}, via (2.21). The tested signal-to-noise ratios are 50, 100, 200, 500, 1000, 2000, and 5000. As an example, for a transient measurement with a total temperature rise of 100 K observed with an accuracy of 20 mK, the signal-to-noise ratio amounts to $R_{SN} = 5000$.

As test case, a thermal impedance corresponding to structure 1 with a signal-to-noise ratio of $R_{SN} = 50$ is solved via a conventional network identification
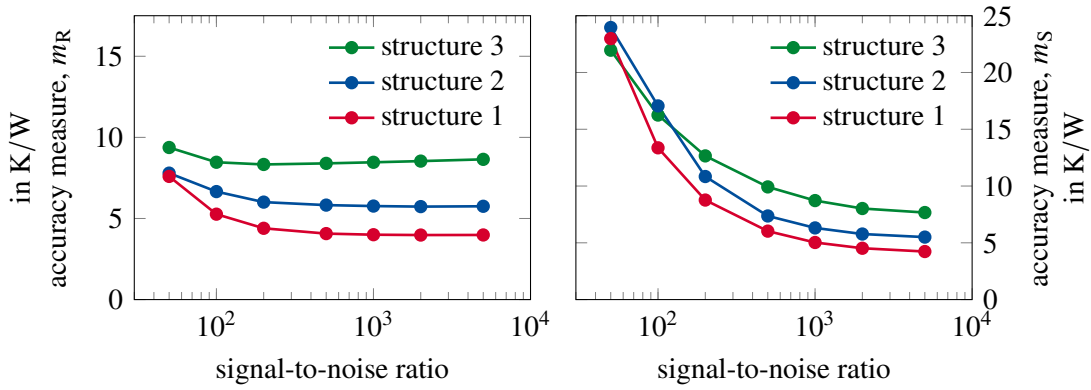
Figure 2.10: *Accuracy of the median integrated time constant spectrum and median structure function calculated via Bayesian deconvolution for the three test structures as a function of the signal-to-noise ratio from* 2000 *noise realizations.*

using Bayesian deconvolution. Figure 2.9 shows the median thermal structure function, the median integrated time constant spectrum, the median impulse response, and the median thermal impedance, as produced by the averaging process, as well as their respective 80 % confidence intervals. For the impulse response, the noise leads to an overestimation between $t = 10^{-8}$ and $t = 10^{-6}$ in a part of the calculations. Accordingly, the integrated time constant spectrum is overestimated on average and the structure function is underestimated. This is a typical defect in an evaluation using Bayesian deconvolution of noisy data. It arises because the impulse response and time constant spectrum have to be strictly non-negative. Negative values have to be corrected by setting them to zero. As a result, the derivative is biased to be overestimated.

For optimal performance, an important adjustment in the presence of noise is the tuning of the derivative parameters. Even though individually adjusting the parameters for every noise level would yield gains in accuracy, here, a single set of derivative parameters is used for all calculations. This is done to make the results independent of these choices and reduce the number of free parameters. In all following calculations, the setup (2.23) is used.

$$
\begin{aligned}
L_- &= 0.60 & L_+ &= 15.0 \\
\Delta L &= 0.20 & N_g &= 250 \\
N_{\text{Bay}} &= 3 \times 10^4
\end{aligned}
\tag{2.23}
$$

For Fourier deconvolution it is not possible to use the same filter width for all signal-to-noise ratios. For every pair of window function and signal-to-noise ratio, the cut-off frequency, Φ_c, is manually adjusted to achieve acceptable results.

A comparison of the computational difficulties to recover structures 1 to 3 in the presence of varying levels of noise for Bayesian deconvolution is shown in Figure 2.10. Continuing the trend of Table 2.3, computations of structure 1 show the most accurate results while structure 3 appears most difficult to recover. Furthermore, it stands out that for all test structures the recovered structure
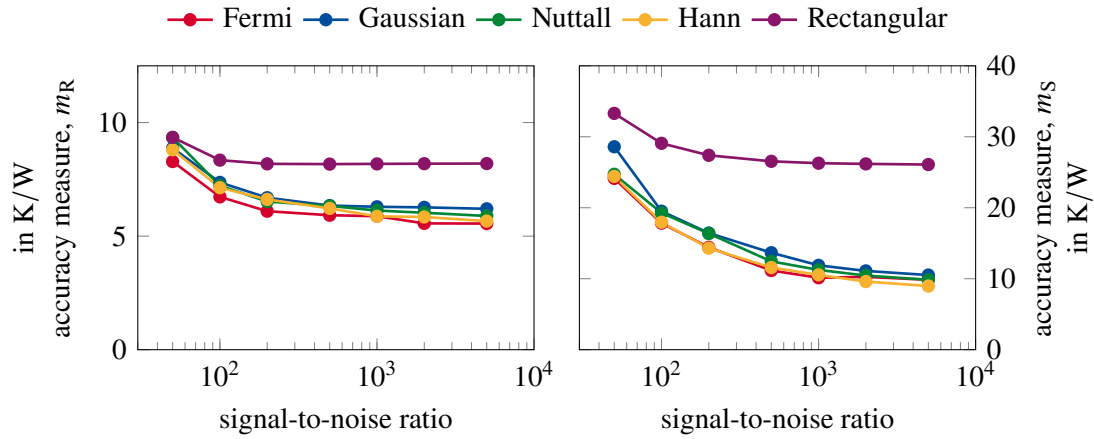
Figure 2.11: *Accuracy of the median integrated time constant spectrum and median structure function for Fourier deconvolution, using a Fermi filter, Gaussian filter, Nuttall filer, Hann filter, and Rectangular filter as a function of the signal-to-noise ratio calculated from* 2000 *noise realizations for structure* 1.

function benefits more from decreasing levels of noise than the time constant spectrum. This means that there is a remaining degree of freedom in the shape of the time constant spectrum besides the accuracy measure, m_R, which has a significant influence on the accuracy of the structure function, m_S.

Next, the relative performance of the algorithms is analyzed. First, the filter choices for the Fourier method are compared to each other, see Figure 2.11. In contrast to the derivative parameters (2.23), which are used for all noise levels, the filter parameters have to be manually adjusted for each filter and noise level. The rectangular filter performs the worst by a large amount. The remaining choices are relatively similar in performance. However, in most cases the Hann and Fermi filter have a slight edge in performance when compared with the Nuttall and Gaussian window. Note that the Gaussian and Fermi windows require tuning of two filter parameters. Because of this, significantly more tuning effort is required when using these filters. Given the results for structure 1, the Hann filters is a good choice in practice.

For the comparison of Fourier deconvolution with the other methods, the Hann filter is chosen and the Powell solver is used for optimization-based network identification. The results are compiled in Figure 2.12. For each data point, an average over 2000 independent realizations of Gaussian noise is calculated employing the method in question. Confirming the results from the computations without noise, Fourier deconvolution yields the most inaccurate results for all levels of noise, while optimization-based network identification achieves the best results. In particular in the presence of higher noise levels, the optimization-based network identification is able to calculate the structure function to significantly better accuracy. This is possible, because this approach avoids the difficulties connected with derivation and deconvolution in the presence of noise, apart from generating the initial values.
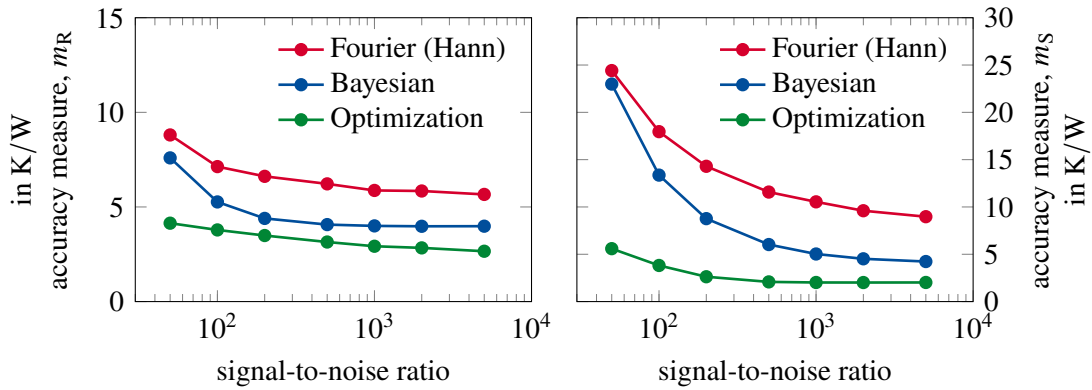
Figure 2.12: *Accuracy of the median integrated time constant spectrum and median structure function for Fourier deconvolution, using a Hann filter, Bayesian deconvolution and optimization-based network identification using the Powell solver as a function of the signal-to-noise ratio calculated from* 2000 *noise realizations.*

2.3.4 Linear-time sampling

In a last step, the quality of the data is reduced further. The exact thermal impedance is resampled using a fixed sampling rate in linear time, t, of 10^7 Hz. In addition, the starting point is added. To limit the number of data points, the sampling rate is slowed down once a certain density of points in logarithmic time, z, is reached. The resulting thermal impedance consists of 784 data points. As an example, a noise pattern is shown in the bottom right of Figure 2.13.

Additionally, an optimization-based network identification with six sections using a thermal impedance with a signal-to-noise ratio of $R_{SN} = 50$ is shown exemplarily. Both structure functions from the conventional algorithm and the optimized result are shown. Additionally, the integrated time constant spectrum of both methods is provided. The impulse response and the thermal impedance, which are shown for the Bayesian solution, are generated by reconvolving the time constant spectrum according to (1.73). This is done to show the impulse response and the thermal impedance which are actually represented by the time constant spectrum. As a comparison, the exact results belonging to structure 1 are shown.

In Table 2.4, the respective accuracy values achieved by the Bayesian solution and the optimized solution are shown as well as the median accuracy values, which are taken from Figure 2.14. The noise pattern presented in the bottom right part of Figure 2.13 leads to a solution with a significantly below average quality.

Table 2.4: *Accuracy values for the solutions in Figure* 2.13. *Additionally, comparisons to the respective median values for $R_{SN} = 50$ from Figure* 2.14 *are provided.*

in K/W	BAYESIAN	POWELL	BAYESIAN MEDIAN	POWELL MEDIAN
m_R	9.80	4.68	6.32	4.29
m_S	27.09	7.25	18.66	5.14
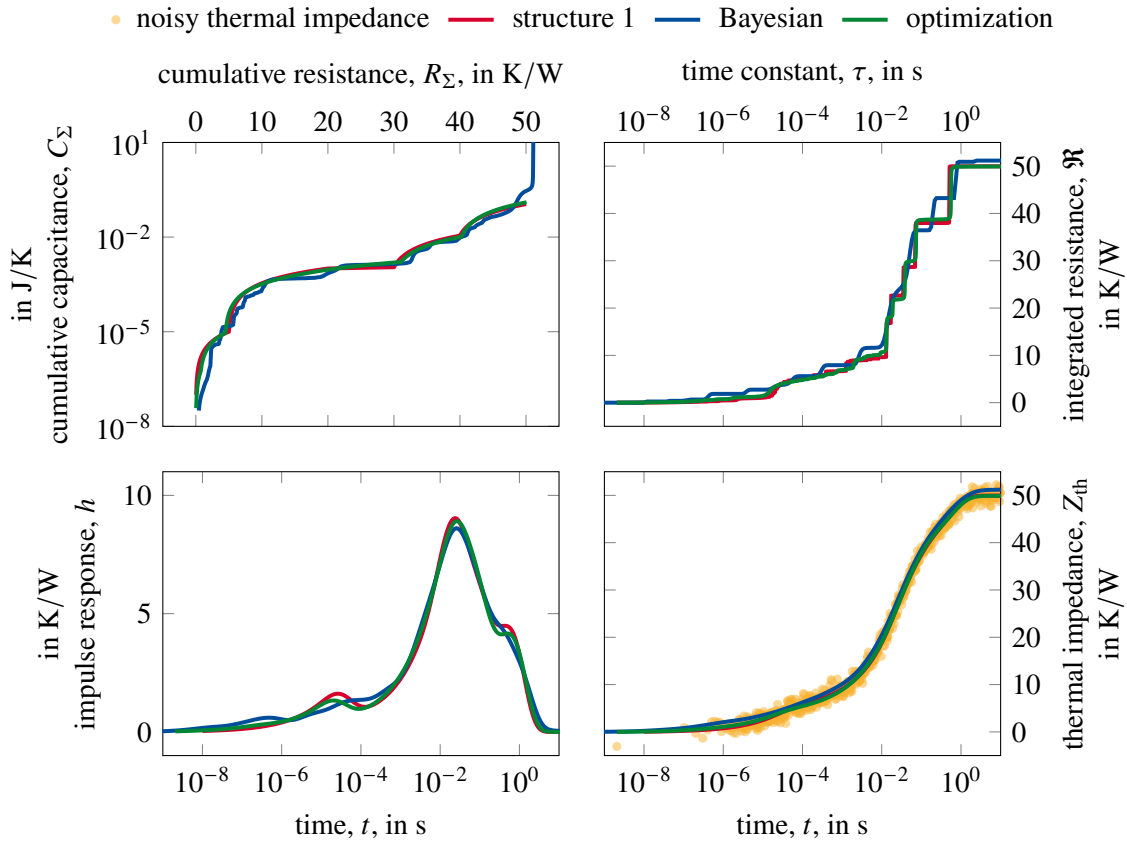
Figure 2.13: *Example solution for a network identification using Bayesian deconvolution and Powell optimization for noisy sparse data with $R_{SN} = 50$. The Bayesian solution is used to generate initial values for the optimization.*

Still, the optimization algorithm is able to increase the accuracy of the time constant spectrum and the structure function significantly. In addition, the thermal impedance of the optimization-based network identification matches better with the exact thermal impedance of structure 1 than the original Bayesian solution. In the optimized structure function, all sections of structure 1 are recovered.

For a systematic analysis of the performance, 2000 instances of the resampled noisy thermal impedances are generated and their respective solutions are averaged by calculating the median. Each of the 2000 Bayesian solutions is used to generate the initial values for the corresponding optimization. The computations in this section are conducted as similarly as possible relative to the evaluation in the previous subsection. This includes the use of the derivative parameters (2.23). For Fourier deconvolution, a Hann filter is used with a manually fine-tuned filter width for each noise level.

The results are shown in Figure 2.14. As expected, the Fourier deconvolution still performs the worst on all metrics. For the time constant spectrum, however, optimization-based network identification and the Bayesian deconvolution show results of similar accuracy. This is possible, because the goal of the optimization is the improvement of o_{imp}, see (2.13), and not of m_R and m_S. Nevertheless,
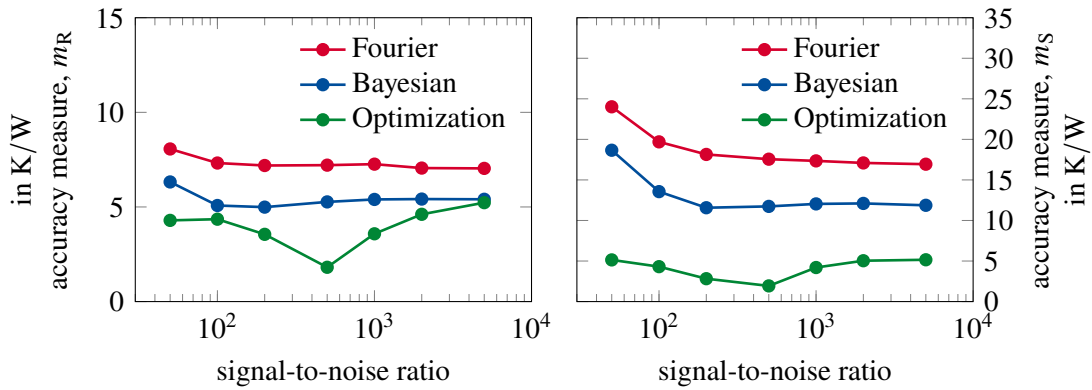
Figure 2.14: *Accuracy of the median integrated time constant spectrum and median structure function for Fourier deconvolution, using a Hann filter, Bayesian deconvolution and optimization-based network identification using the Powell solver as a function of the signal-to-noise ratio calculated from* 2000 *noise realizations.*

the structure function is significantly improved by optimization-based network identification for all noise levels.

It has to be kept in mind, however, that while the optimization procedure is able to increase the accuracy of network identification by deconvolution significantly, it is still based on the initial values. The optimization might converge to a local minimum that does not represent a global optimum. Avoiding this is important for achieving an even better accuracy. In particular for relatively inaccurate initial values, finding the correct local minimum during optimization is not guaranteed.

For the optimization-based solution in Figure 2.14, the accuracy measures do not decrease monotonically with increasing signal-to-noise ratio. This means that for an increasing portion of noise patterns the solver converged to a local minimum with a suboptimum result. By fine-tuning the parameters involved for both the conventional algorithm, which provides the initial values, and optimization-based network identification the quality of convergence increases. An example of this is using different derivative parameters in selected cases besides the ones defined in (2.23) and the use of a different number of sections other than six.

2.4 Conclusion

This chapter provides an extensive overview of different practices used for the determination of thermal structure functions from thermal transient measurements. Together with the theoretical background in the previous chapter, a self-contained treatment on network identification could be created. Starting from an elementary introduction to the physics of heat conduction, this work makes it possible to develop a complete understanding of thermal structure functions and network identification. Detailed descriptions of the implementations for network identification by deconvolution used in the literature and in this

work are given. Commonly used algorithms as well as modified and improved versions of existing algorithms and newly developed approaches are investigated and compared. Finally, a comprehensive overview on the state of the art in network identification by deconvolution and current research areas is presented. An overview of similar scope has not yet been created.

To enable a systematic performance analysis of network identification by deconvolution, specific metrics are developed for the time constant spectrum and thermal structure function for the first time. Using these metrics in combination with a predefined set of test structures, it is possible to objectively compare the performance of algorithms. This presents a clear advantage over the approach by Szalai [12], which uses the concept of a practical maximum tolerance. The approach by Szalai is widely known in the scientific community dealing with thermal structure functions. Using these metrics, the performance of all methods described in this chapter is compared against each other. The analysis is based on various test cases of increasing difficulty, which are generated via resampling and the addition of artificial noise. Existing algorithms could be optimized using this method. In this work, it could be shown that it is possible to significantly enhance the accuracy of network identification by deconvolution.

In particular, the performance of network identification by deconvolution could be improved by showing that performing significantly more steps in the Bayesian deconvolution results in notable accuracy gains for some structure functions. The number of points forming the derivative is less significant beyond a certain level. An adaptive step size algorithm is able to efficiently differentiate thermal impedances of varying signal-to-noise ratios and sampling rates enabling a very high total thermal resistance accuracy of structure functions in combination with Bayesian deconvolution. A systematic test on a number of window functions for Fourier deconvolution shows that the Hann filter is the most suitable filter in practical applications.

A newly developed method, named optimization-based network identification, is presented. It achieves a greatly enhanced accuracy for the price of a higher computational workload. The method impresses in cases of high noise levels and sparsely sampled data while providing divergence free structure functions as well as the corresponding theoretically accurate time constant spectra. As the resulting structure functions do not have a smeared-out divergence at the end, interpreting these structure functions is easier. Because the method is based on inverse calculations, it is not necessary to extrapolate thermal responses for short times, for example via the commonly performed square-root extrapolation. Instead, the physical model underlying the method naturally extends the prediction for all times.

All test cases in this chapter consist of theoretically generated piecewise uniform structure functions. This could give an advantage to optimization-based network identification, as it is also based on piecewise uniform structure functions. The case of real measurement data is explored in the next chapter. There, thermal transient measurements based on the forward voltage of a p-n junction are evaluated. Additionally, the use of infrared thermography for network identification via thermal transient measurements is explored.

Chapter 3

Thermographic application

Some results in this chapter have been published in [79]*,* [90]*,* [91]*,* [92]*,* [93] *and* [94]*.*

3.1 Non-destructive testing

3.1.1 Introduction

With the need to replace fossil fuels, electrification is taking place in many areas. For applications in electrical supply networks, electric motors, or in automotive applications, this increases the demand for power semiconductors such as IGBTs (insulated-gate bipolar transistors), thyristor or power MOSFETs (metal-oxide-semiconductor field-effect transistors). This is pushing manufacturers to strive for ever higher efficiencies and smaller devices, with the result that the power output and quality requirements for these devices are increasing. High power densities are also found in IC packages (integrated circuit packages) and LED lighting applications, where high temperatures severely impact lifetime and reliability. At the same time, the ongoing system integration increases the complexity of devices, which in turn raises the demands on test methods.

Non-destructive testing has established itself as a valuable tool for the analysis of thermal behavior in these applications. The applied techniques are also suitable to analyze the electrical functionality or to identify mechanical defects. Non-destructive testing has also become a valuable tool in failure mode analysis. The results assist in research and development, inline quality control, during production or maintenance work. They allow an informed decision to be made whether a component should be processed further, an element needs to be replaced, or a design objective has been achieved.

An overview of non-destructive testing techniques commonly used in IC package analysis can be found in [95]. Common defects in these devices are voids or cracks in solder joints and layer delamination.

The aerospace industry is a typical field of application for infrared thermography. An extensive overview of recent advances in this area is provided by [96]. Inspection via infrared thermography offers a non-destructive and non-contact measurement method that helps to meet the high safety requirements in civil aviation. Often, the objects under examination are composite materials that may

be subject to impact damage, thermo-mechanical fatigue, layer delamination, and many other modes of failure.

Besides thermographic investigation, radiographic methods such as X-ray inspection or X-ray computed tomography are applied. Using X-ray microscopy, lateral resolutions in the order of a few microns can be achieved [95]. The main challenges lie in the long scanning and computation times as well as a dependence on material composition.

Other non-destructive testing techniques employed include scanning acoustic microscopy [97], magnetic current imaging [98, 99, 100], surface acoustic waves [101], visual inspection [102], and more. Outlining all of these techniques is beyond the scope of this work, as the focus here lies on infrared thermography.

3.1.2 Thermographic testing

Infrared thermography is a well-established technique for non-destructive testing [103, 104]. Modern high-resolution infrared cameras provide detailed insights into thermal dynamics down to a geometrical resolution of almost one micrometer. Combined with high sampling rates of up to several hundred hertz, the amount of data collected during these measurements quickly adds up to several gigabytes. Modern techniques make it possible to compress the data while losing as little essential information as possible. Sophisticated post-processing algorithms are employed to enhance the sensitivity and to detect even the slightest deviations in thermal behavior.

A typical goal of these evaluations is the characterization of defective samples, for example, by determining defect dimensions and defect depths and by quantifying their influence on heat conduction. In other cases, the physical parameters of heat conduction or properties derived from them are determined. An example is the characterization of layer thicknesses of coatings.

Infrared thermography can be used as a purely passive observation tool. In this way, it allows to record equilibrium temperatures during different modes of operation, revealing unforeseen thermal interactions between components. It is also possible to visualize hotspots caused by narrow electrical connections or defective components.

More detailed information is obtained with active infrared thermography. For these methods, the sample is additionally excited by external heating sources. The resulting thermal dynamics allow conclusions about the internal structure or the thermal properties of the device. A typical setup for lock-in thermography is shown in Figure 3.1.

For lock-in thermography, a periodical excitation is applied which induces thermal waves into the sample [105, 106]. During their (highly dampened) propagation through the device they interact with material boundaries and inhomogenities inside the device. An example of such a defect in an IC package would be a delamination or a void inside a solder connection. This method is very sensitive by merit of the lock-in principle, but requires long measurement times.
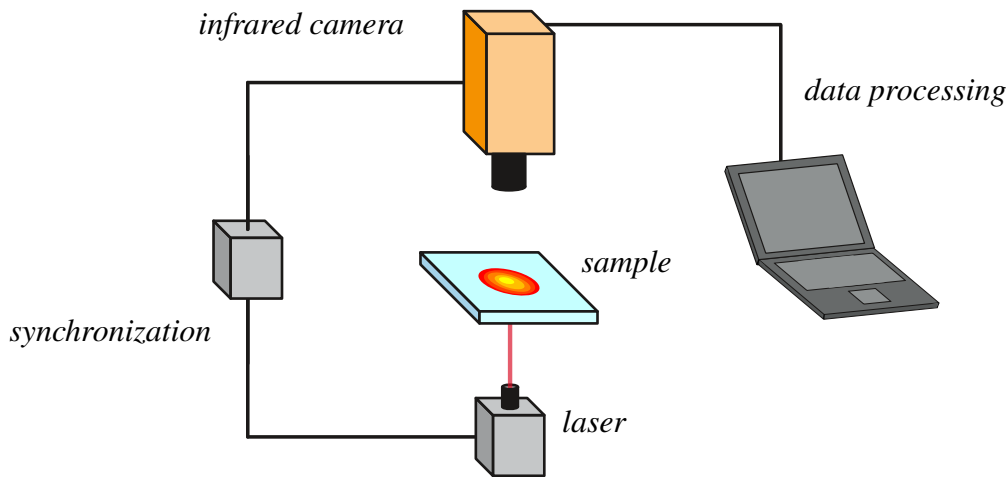
Figure 3.1: *A typical setup for lock-in thermography consists of a synchronized infrared camera and an excitation source. The resulting image sequence is evaluated via digital data processing.*

In pulsed thermography, a high heating power is applied for a short time [107]. The resulting impulse response depends on the local environment of the heated area. Defective sections of a device will show a different response compared to a defect-free sample. Reference samples or areas are often used in this type of investigation.

In transient or step heating thermography, the transition from an on-state temperature distribution to an off-state distribution is observed, or vice versa. This method is similar to pulsed thermography, except that here the step response is measured instead of the impulse response, see Section 1.2. As a result, fewer issues with the high momentary powers during instantaneous energy deposition arise. In turn, step thermography features a longer measurement time.

As a means to apply heat into or onto a device under test, a wide range of sources have been applied [96, 107]. The suitability of a heating method depends on the nature of the sample and the type of thermography. Besides self-heating of a device, for example via periodically applied electric power during a lock-in measurement, heat is often applied electromagnetically. This includes optical heating via flashlamps, halogen lamps, or lasers as well as other types of radiation such as microwaves. Furthermore, in conductive samples heating can be applied via induced eddy currents. In the field of vibrothermography, friction processes during vibrations induced for example via ultrasonic waves are detected via infrared thermography. Even convective heating, for example via hot air, is possible in sufficiently slowly reacting processes.

3.1.3 Processing thermographic signals

For a comprehensive study of thermographic evaluation algorithms see [14, 107, 108, 109]. A brief overview treating the most common techniques is given below. Many infrared thermographic methods rely on a contrast parameter such as a temperature difference, ΔT, of a single pixel to a later time or to a reference.

Alternatively, the relative deviation, $T_{\text{test}}/T_{\text{reference}}$, can be analyzed as well as other contrast parameters. The differential absolute contrast evaluation falls in this category.

Another approach is the comparison of temperature curves with analytical models or computer simulations of the tested device. The simplest case is a one-dimensional semi-infinite homogeneous body, but more complex models of higher dimension have also been applied, for example to assist automatic defect classification [110]. Furthermore, various techniques from the field of image post-processing can be applied such as smoothing filters. In principle, this includes the entire area of video processing and refinement methods.

Integral transform techniques are also popular such as the use of Fourier transformation for pulse phase thermography. In this method, a fast Fourier transformation is used to extract amplitude and phase information of the temperature curve for each pixel. In this sense, it is similar to lock-in thermography. Both techniques have the advantage that the phase information is independent of signal strength, which greatly limits the impact of inhomogeneous emissivities and excitation. Besides the Fourier transform, the use of Laplace transform, Wavelet transform, and Hough transform is documented. The transformations differ with respect to the basis functions employed. Depending on the nature of the spatial and temporal temperature dependence, these transformations show varying success. The Hough transform, for instance, specializes in recognizing geometrical shapes such as lines or circles.

The approach of matrix processing algorithms, such as the principal component thermography, is also common. In this method, a singular value decomposition is performed to extract a set of orthogonal functions based the dataset itself, the empirical orthogonal functions. The most significant of these functions capture the main dynamics of the process, often including the defective regions. Typically, the noise is projected onto higher order functions making the other images sharper.

Lastly, the thermographic signal reconstruction by Shephard *et al.*, which belongs to the class of model fitting techniques, is explained here in more detail [13, 16]. A practical example from a medical application and a comparison to other methods using a flat bottom hole sample are given in [15]. To perform a thermographic signal reconstruction, first, the surface is instantaneously heated by an idealized Dirac heating impulse of energy density Q [14]. In a semi-infinite homogeneous body, this induces surface temperature change, $T(t)$, relative to the initial temperature, T_0, of

$$T(t) = T_0 + \frac{Q}{e\sqrt{\pi t}} \,, \tag{3.1}$$

where e is the thermal effusivity. Rewriting this equation to a logarithmic form yields

$$\ln(\Delta T) = \ln\left(\frac{Q}{e}\right) - \frac{1}{2}\ln(\pi t) \,. \tag{3.2}$$
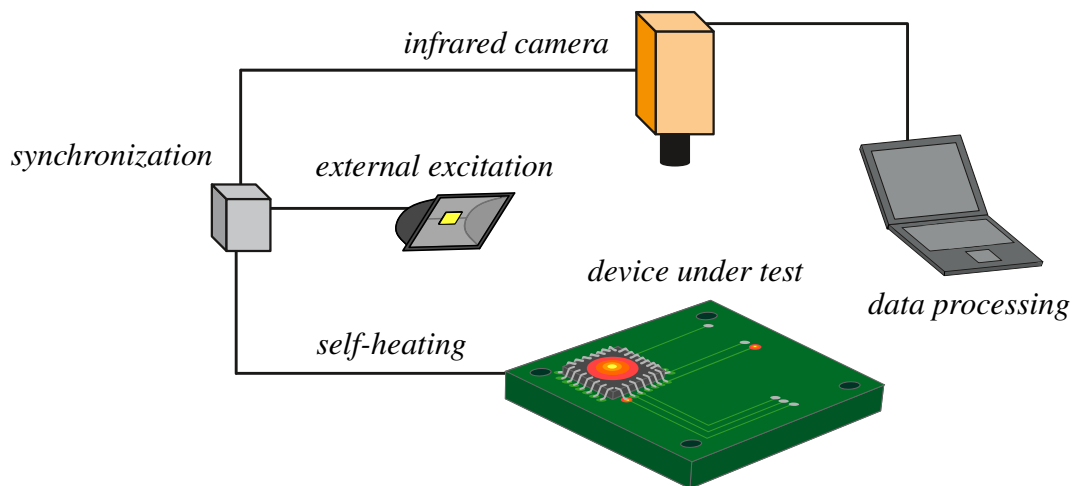
Figure 3.2: *Experimental setup for a thermographic network identification via self-heating or external excitation of an integrated circuit as device under test.*

In this way, it can be seen that when fitting a polynomial in logarithmic time, $z = \ln(t)$, to the logarithm of the temperature difference, a polynomial of first degree is appropriate. In practice, the thermal behavior might be more complex, for example due to defects in the material. Hence, a polynomial of higher degree is approximated. The use of polynomials from order 4 to 11 is reported [14, 15, 16].

$$\ln(\Delta T(z)) \approx a_0 + \sum_{i=1}^{N} a_i z^i = T_{\text{TSR}}(z) \tag{3.3}$$

For the evaluation, images of the first and second derivative of $T_{\text{TSR}}(z)$ are examined.

3.2 Thermographic network identification

This section discusses a thermographic non-destructive testing technique developed and patented as part of this work called "thermographic network identification" [17]. The method was developed by the author in collaboration with Peter W. Nolte and Stefan Schweizer and is introduced and discussed in the following.

For thermographic network identification, a pulsed or transient thermal excitation is applied to a device under test. An infrared thermographic measurement of the resulting impulse or step response is used as input to a network identification. A typical measurement setup is shown in Figure 3.2. It consists of an infrared camera in a top-down view of the device under test, which is subject to either self-heating or external excitation, for example via a powerful spotlight. Data acquisition and heating power are controlled through a centralized synchronization. As a device under test, an integrated circuit is shown.
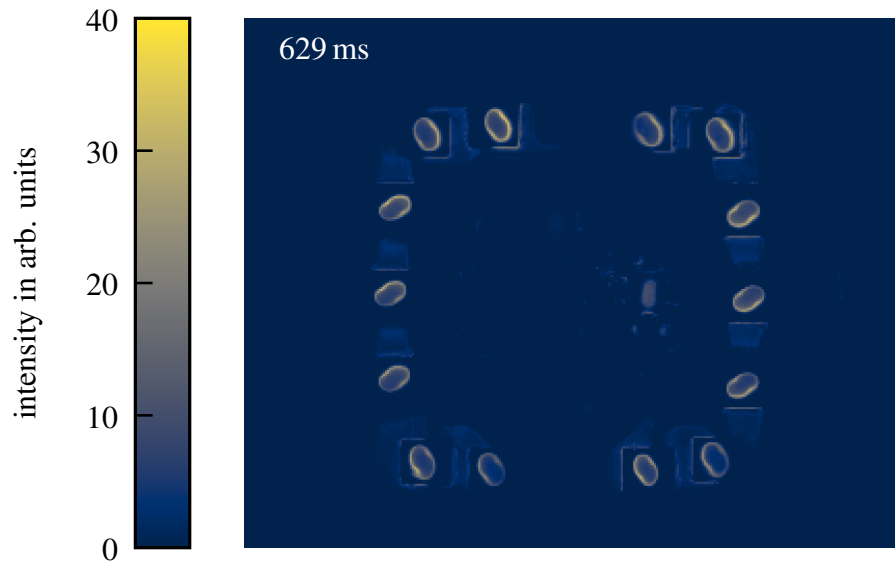
Figure 3.3: *Result of a thermographic network identification. The image shows the spatially resolved time constant spectrum of a lamp similar to Figure* 3.4c *at* 629 *ms. The measurement is not emissivity corrected and a homogeneous unit power step is assumed.*

To perform a thermographic network identification, the algorithms discussed in the first part of this work are suitable. In this application, special emphasis is put on the computational efficiency of the algorithm, as an independent network identification is performed for each pixel in the infrared image sequence. In this way, a unique time constant spectrum is obtained for each pixel. When compiled together, they form the spatially resolved time constant spectrum. To process a full-frame infrared image sequence, on the order of 10^5 network identifications have to be performed. This results in a particular need for a fast implementation of the algorithm or high parallelization. It is possible to visualize both the time constant spectrum and the thermal structure functions in this way. As an example, in Figure 3.3 a spatially resolved time constant spectrum belonging to an E27 socket LED retrofit lamp (see Figure 3.4c) is shown. The image compiles the amplitudes, i. e. the resistances in the equivalent Foster networks, of all time constant spectra at $\tau = 629$ ms. In Subsection 3.4.1, spatially-resolved time constant spectra are explained and analyzed in detail. When imaging spatially resolved structure functions, the model-based limitations of network identification by deconvolution have to be kept in mind. Measured two-dimensional thermal impedances are always valid and two-dimensional time constant spectra derived from it yield accurate predictions as long as the same excitation pattern and environment conditions are maintained.

In the following, the merits of thermographic network identification are discussed as compared to other infrared thermographic non-destructive testing techniques and in relation to forward voltage-based network identification by deconvolution. Thermographic network identification is usable in several ways. On the one hand, it is able to serve as a visualization tool for defect detection in non-destructive testing. Additionally, is able to provide temperature predictions,

given a power function. Lastly, when the emissivity and power step are accounted for and the heat path is suitably one-dimensional, accurate thermal resistances and capacitance are recovered with the structure function.

True volumetric evaluation of thermal properties is done via thermal impedance tomography [111]. This method strives to solve the full three-dimensional problem of recovering internal parameters from surface distributions. The procedure is mathematically similar to electrical resistivity tomography, from the field of geophysics, or electrical impedance tomography, a medical diagnostic technique. However, fully recovering internal parameters from surface data only is a severely ill-posed problem.

When calculating structure functions via thermographic network identification, the applied power has to be controlled precisely. Only in this way, are valid thermal resistances and capacitances obtained. For optical excitation, the radiation has to either be sufficiently homogeneous or its spatial distribution needs to be known. Halogen lamps, which are commonly used, show a significant afterglow due to their thermal inertia, which affects the power step directly and via infrared reflections.

When used as a thermal non-destructive testing technique, the requirements of thermographic network identification towards heating power are more relaxed, as the goal consists in noticing defects and an imaging thereof. In some infrared thermographic testing techniques, the analysis relies on phase information, which is independent of signal strength. This makes them less sensitive to inhomogeneous emissivities and similar defects. Similarly, for the time constant spectrum a constant scaling factor in the temperature does not affect the location of the peaks.

Thermographic network identification provides a means to monitor electric devices at an early stage and investigate arbitrary components, not only those that have a suitable electric connection. In addition, no device-specific calibration is required. The method is contactless and derives time constant spectra distributed over the entire test specimen. For each component, spatially resolved information is obtained. Thermographic network identification yields quantitative dynamic thermal parameters in a well-defined physical model. This enables the quantification of the actual thermal impact of a defect.

3.3 Verification

In following sections, an analysis of the algorithms for network identification by deconvolution on real measurement data is performed. The algorithms discussed in Section 2.1 include different deconvolution methods as well as the newly developed optimization-based network identification. The test on real measurement data is different from the generated test cases in several aspects. On the one hand the tested devices do not have ideal piecewise uniform solutions. In addition, sampling rate and signal-to-noise ratio are different. In particular for infrared measurements, the lower sampling rate might lead to discontinuities in the derivative, depending on the thermal inertia of the sample.

3.3.1 Experimental realization

Experimental setup

For the infrared thermographic measurements, the camera used is an InfraTec ImageIR 8380S. It is a cooled camera that employs an indium antimonide focal plane array snapshot detector, which is sensitive between 2.0 μm and 5.7 μm. The camera is able to record infrared images with a geometric resolution of 640 × 512 px. In full frame mode, it records image sequences up to a frequency of 200 Hz. At the price of a reduced geometric resolution in half frame mode, it is possible to increase the frame rate to 500 Hz. This offers the possibility to better capture fast thermal dynamics on small components where a large field of view is not required.

Frame synchronization is achieved with the help of a National Instruments USB-6003. For power control, a solid state relay or a source measurement unit Keithley SMU 2461 is employed, depending on the sample and excitation type. The entire setup is enclosed to limit convection and reflections from external infrared sources.

What follows, is a brief discussion of experimental side effects that need to be considered during thermographic network identification. Despite the synchronization, it is sometimes difficult to determine the exact time of the power step. Not only does the power step have a finite steepness in reality, but the electrical properties of the device also delay its reaction by an unknown amount. For example, the device under test might feature additional capacitors or the switching speed of the relay might be significant. Because of this, in some cases the zero point, t_0, has to be adjusted by hand. For high geometric resolution, special care is taken to limit vibrations in the infrared camera relative to the sample. Thermographic network identification is especially sensitive to this effect, as noise components for low z have a high impact on the overall accuracy.

The samples

As practical applications, thermal transient measurements on the four samples shown in Figure 3.4 are performed. In the following, the samples are introduced and the analysis performed on them is outlined. All four devices are self-heated electrically, no external excitation is used.

First, the stand-alone high-power LED as shown in Figure 3.4a is investigated. The yellow phosphor of the LED has a relatively good emissivity which is assumed to be one here. For a precisely determined power step, light emission needs to be accounted for. As the goal here is not to measure accurate thermal resistances, it is neglected and the exact power during the transient measurement step remains unknown. As a result, the measured thermal impedances are only proportional to the true ones. On the LED, both infrared and forward voltage measurements are conducted, as it is the only sample that allows forward voltage measurements. At the end of this Section, a comparison between the two measurement principles is conducted. Forward voltage measurements

(*a*) *stand-alone high-power LED*

(*b*) *black-coated heating pad*

(*c*) *E27 socket LED lamp*

(*d*) 4 × 4 *LED module*
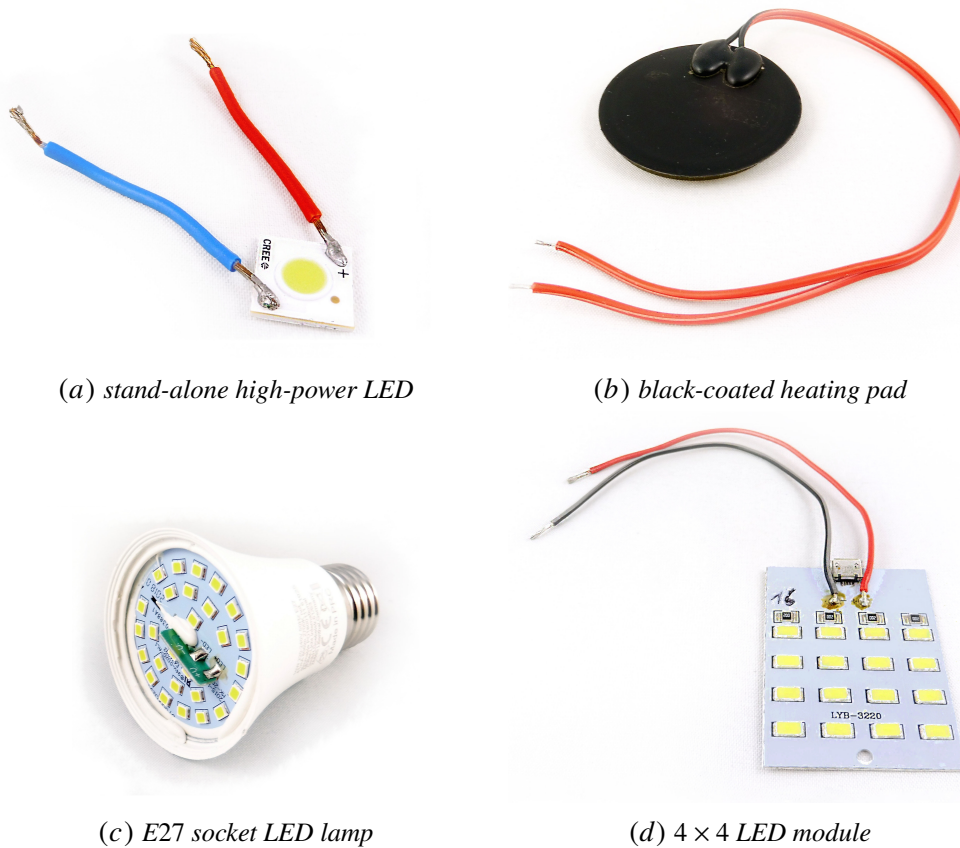
Figure 3.4: *Compilation of all four sample types analyzed in the following. The E27 socket LED lamp is representative for a range of similar lamps which are all analyzed below. All LED lamps have the light-diffusing plastic cap removed to allow a direct view of the LEDs.*

on this sample are evaluated in Sections 3.3.2 and 3.3.3. In addition, it is used to compare the optimization-based network identification and network identification via Bayesian deconvolution.

Next, the heating pad as depicted in Figure 3.4b is examined. It consists of a spiraled ohmic resistance to provide a homogeneous surface heating (compare Figure 3.15). To make the surface suitable for infrared imaging, it is coated with black paint, which as an emissivity of approximately $\varepsilon = 0.95$. In Section 3.3.4, the quality of the thermal equivalence network to predict temperature developments given a power curve is checked. In this way, it is possible to validate the thermal models.

An electronically more sophisticated device is analyzed in the form of an E27 socket LED retrofit lamp. The lamp shown exemplarily in Figure 3.4c stands representative for a range of eight comparable LED lamps, which are analyzed in Section 3.4. A statistical evaluation using the time constant spectra of the LED chips reveals differences between and within each lamp.

Lastly, Figure 3.4d depicts a 4 × 4 LED module. In this device, the circuit layout prevents measuring individual forward voltages of the LEDs. However, infrared based measurements are unhindered by this. Advanced analysis using
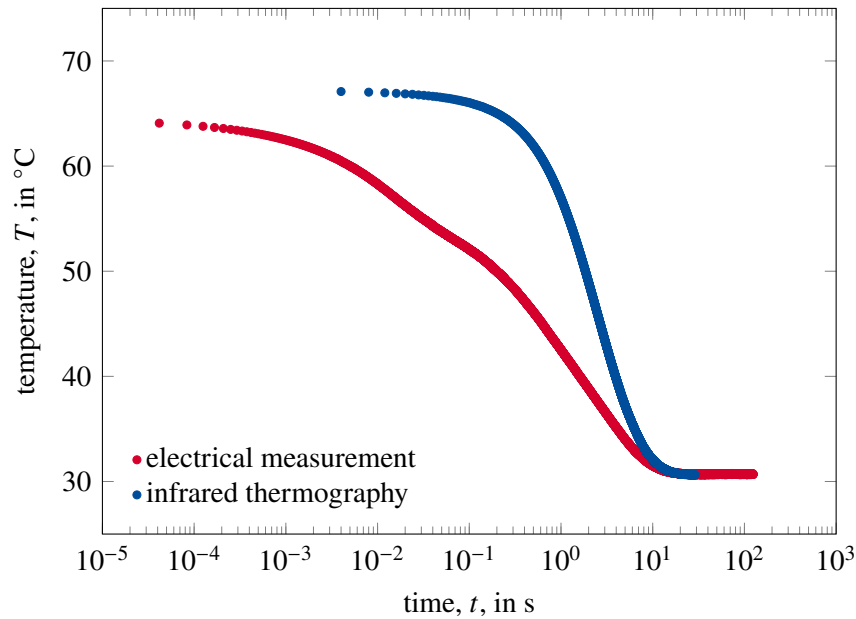
Figure 3.5: *Comparison of temperature measurements conducted via infrared thermography and forward voltage on the stand-alone high-power LED (Figure 3.4a).*

thermographic network identification is conducted in Section 3.4.2. The goal is to identify bottlenecks in the heat conduction path.

For all measurements on LEDs in the following, the light emission is not included in the power step. Therefore the power step is assumed to be one. As a consequence, the impulse response, the time constant spectrum, and the structure function have to be multiplied by a constant factor. Time values and time constants, however, are not affected by this. In the time constant spectrum, a different value for the power step appears as a constant scaling factor of the *y*-axis. The relative height of the peaks as well as their location is not affected.

Infrared versus voltage measurements

To compare forward voltage-based and infrared measurements, a transient thermal measurement is performed on the stand-alone high-power LED, see Figure 3.5. The electrical measurement is extrapolated for low times to mask the electric transient. For the extrapolation, a conventional square-root extrapolation is performed. A temperature controlled heat sink is used to set the equilibrium temperature to 30 °C, which is reached by both measurement methods in the limit.

For short times, the equilibrium temperature of the voltage-based measurement is lower than the infrared thermographic observation. This highlights the difference in measurement location between the two principles. A possible explanation for the higher temperature in the phosphor is the additional heat generation caused by the stokes shift in the light conversion process. The high thermal resistance of the phosphor prevents an efficient cooling and causes a gap between junction and phosphor temperature. High phosphor temperatures

are a common problem in LED design. Another aspect to keep in mind is that the junction temperature represents a spatial average of the temperature over the region of the p-n junction. Therefore, locally junction temperatures higher than reflected by the forward voltage measurement may exist. This comparison shows that when analyzing thermal transients, the difference in measurement location has to be kept in mind.

3.3.2 Algorithmic comparison on real data

The purpose of this section is to compare the performance of different variants of network identification when faced with real measurement data. In the previous chapter, a similar analysis using artificial measurement data is performed. In that case, measures of accuracy, m_R and m_S, are available, which directly compare the results to the reference structure. There, the analysis concluded that optimization-based network identification performed best, followed by Bayesian and then Fourier deconvolution.

Here the objective function, o_imp, introduced in (2.13), has to serve as a performance metric instead. It quantifies the difference between the measured thermal impedance, $a_\text{measured}(z)$, and the result of the evaluation, $a_\text{calculated}(z)$. For optimization-based network identification, $a_\text{calculated}(z)$ corresponds to the optimized thermal impedance. In network identification via Bayesian and Fourier deconvolution, the reconvolved and integrated time constant spectra are used. For details of the implementation used, see Section 2.1.

As a test case, a voltage-based thermal transient measurement on the stand-alone high-power LED introduced in Figure 3.4a is evaluated. Using a K-factor calibration, the forward voltage is translated into a temperature. The electric transient is masked by extrapolation. The related thermal impedance is shown in Figure 3.6, bottom right. Additionally, the results of network identifications using Fourier and Bayesian deconvolution as well as results from an optimization-based network identification are given. The thermal impedance in the bottom tight part of Figure 3.6, as well as the impulse response, are calculated by reconvolving and integrating the corresponding time constant spectra. The respective accuracies of the solutions as measured by o_imp are compared in Table 3.1.

In the absence of an objective measure of accuracy for the structure function and time constant spectrum, there are two intuitive ways to choose the cut-off frequency of a filter for the Fourier deconvolution. The first way is by visual judgment of the results and the other way is to determine the optimum filter by minimizing o_imp. Here, a Hann filter is used with a cut-off frequency, which achieves a low value for o_imp. For the Bayesian deconvolution, 3×10^4 iteration steps are performed.

The optimization-based network identification uses a Bayesian deconvolution to generate the initial structure function, which is approximated by a piecewise uniform structure function with six sections. This is an assumption about the form of the structure function of the device, which is analyzed below.
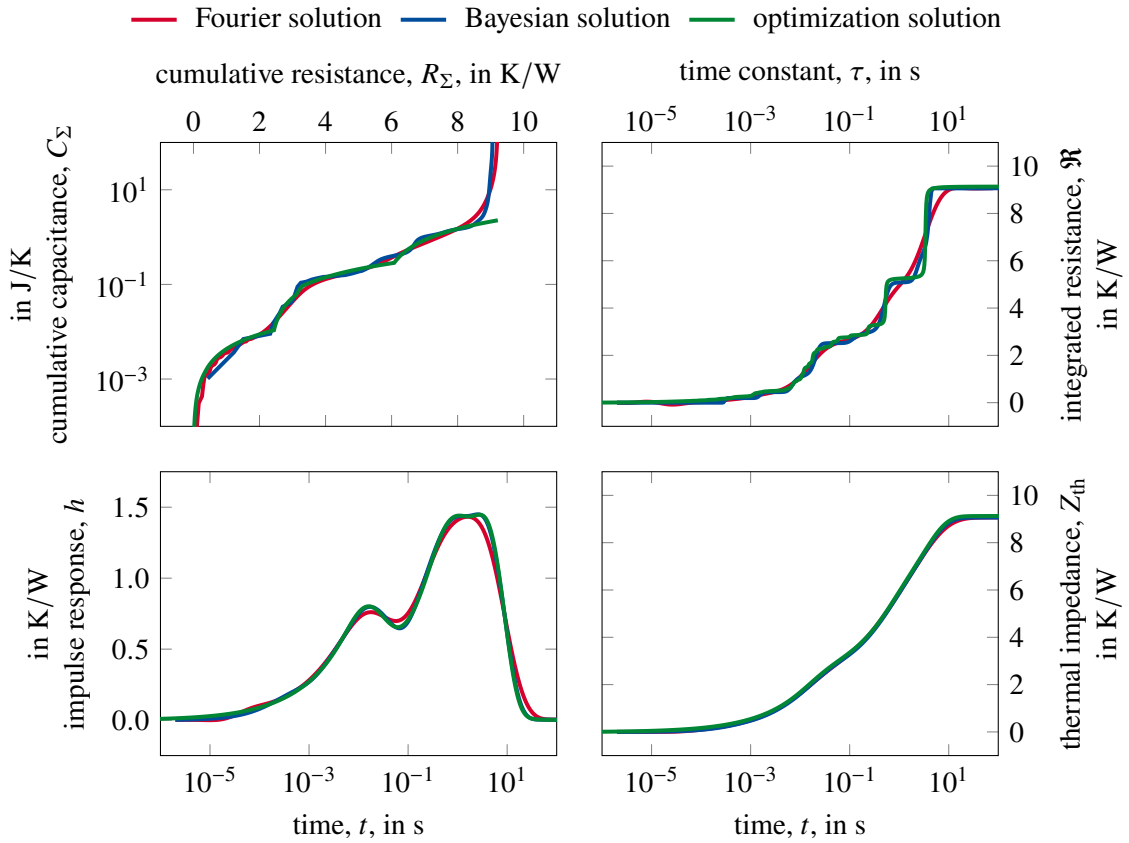
Figure 3.6: *Comparison of different variants of network identification for a thermal transient measurement on the stand-alone high-power LED in Figure 3.4a. The thermal impedance and its derivative are calculated by reconvolting the time constant spectrum. The corresponding accuracies to the measure thermal impedance o_{imp} are gathered in Table 3.1.*

For high and low cumulative resistances, R_Σ, the optimized structure function deviates the most from the conventional approaches (Figure 3.6, top left). For low R_Σ, the structure function not limited by the discretization resulting from the Foster-to-Cauer transformation via polynomial long division, which is only feasible up to a few hundred points. For high R_Σ, the optimized result has no divergence, which masks the final part of the structure function. Additionally, the optimization result has fewer noise components. The impulse response and the integrated time constant spectrum of the Fourier solution deviates significantly from the Bayesian and optimization solutions.

A detailed view of the results including the measured thermal impedance is provided in Figure 3.7. The optimized thermal impedance matches the

Table 3.1: *Comparison of the difference between the measured thermal impedance and the reconvolved time constant spectrum.*

in K/W	FOURIER	BAYESIAN	OPTIMIZATION
o_{imp}	0.308	0.282	0.022
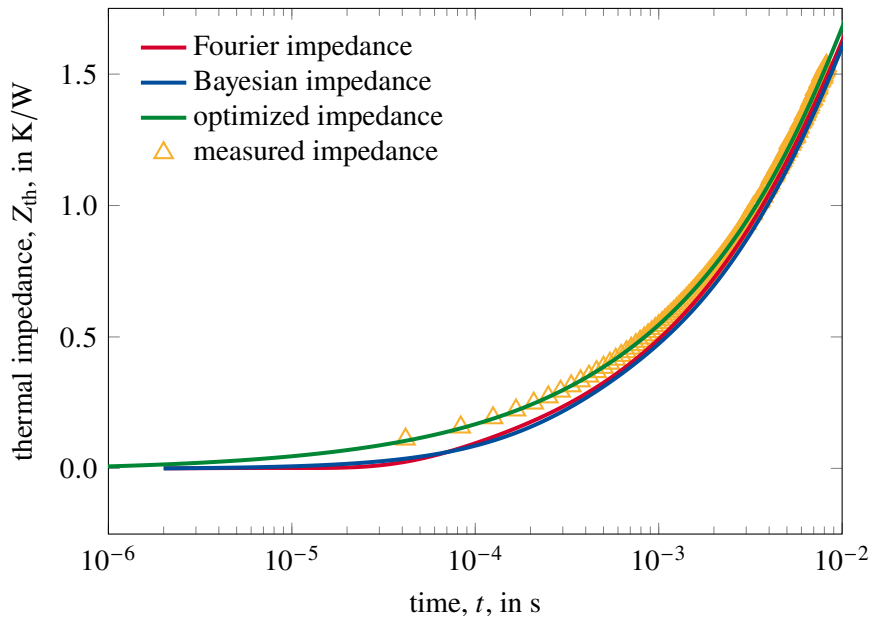
Figure 3.7: *Enlarged view of the calculated thermal impedances shown in the bottom right of Figure* 3.6. *The corresponding deviations from the measured thermal impedance o_{imp} are gathered in Table* 3.1.

measurement data closely. As visible from the results in Table 3.1, this amounts to a significant gain in accuracy when integrated over the entire curve. The algorithm based on Bayesian deconvolution performs better than Fourier deconvolution while requiring no tuning of the filter parameters. These results support the conclusion of the previous section that optimization-based network identification is the more accurate method.

The optimization-based network identification performed above is repeated with 3, 6, 9, and 12 sections. In Figure 3.8, the obtained structure functions and their corresponding integrated time constant spectra are compared. The resulting values for o_{imp} are compiled in Table 3.2. In comparison with conventional network identification, the optimization results for 6, 9, and 12 sections all show significantly increased accuracy. However, using too few sections results in a decrease in accuracy, as shown by the optimization using three sections. The obtained structure functions and time constant spectra are similar for all results and in parts identical. For high R_{Σ}, the solutions for 3 and 6 sections as well as the solutions for 9 and 12 sections have each converged to similar local minima, respectively. To judge which piecewise uniform structure function characterizes the device under test best, a more detailed analysis is required. As the computational workload increases significantly with an increasing number of sections, the solutions with fewer sections are more efficient while providing similar accuracy according to o_{imp}.
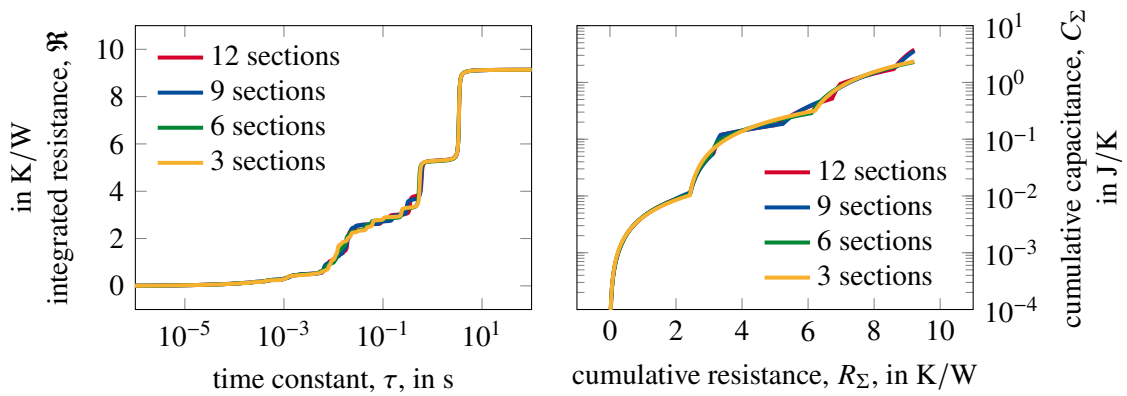
Figure 3.8: *Dependence of the result of optimization-based network identifications on the number of sections in the piecewise uniform structure function. The corresponding similarities o_{imp} are gathered in Table 3.2.*

3.3.3 Transient dual interface measurements

The transient dual interface test is an established method in transient thermal testing. Its measurement and evaluation procedure is described in the standard JESD51-14 by the JEDEC solid state technology association [7]. The method is discussed and expanded up to this day [42]. For an extension, current discussion points include the extension to multi-chip devices or incorporation of parasitic heat paths. The method offers a means to quantify the entire heat path from source to environment and to identify the total thermal resistance up to a predefined point. This is done by introducing different interface layers at the position in question and recording a thermal transient for each case. A typical example is the determination of the total thermal resistance of an integrated circuit up to the board. In this case, transient thermal measurements both with and without thermal grease as interface material from the chip to the board are conducted. This introduces a divergence between the two corresponding thermal impedances. The point of separation is used to determine the thermal resistance of the device. In this way, the transient dual interface test helps to measure thermal resistances of complex devices and to interpret their structure function.

In the following, an outline of the evaluation procedure is given. Then, results of a transient dual interface test are analyzed, see Figure 3.9. The network identifications necessary for the evaluation are performed via optimization-based network identification. As a comparison, the analysis is repeated using the conventional method as described in the standard JESD51-14.

For the transient dual interface test, the stand-alone high-power LED in

Table 3.2: *Accuracies of optimization-based network identifications for a varying number of sections in the piecewise uniform structure function.*

in K/W	3 SECTIONS	6 SECTIONS	9 SECTIONS	12 SECTIONS
o_{imp}	0.0303	0.0216	0.0212	0.0205
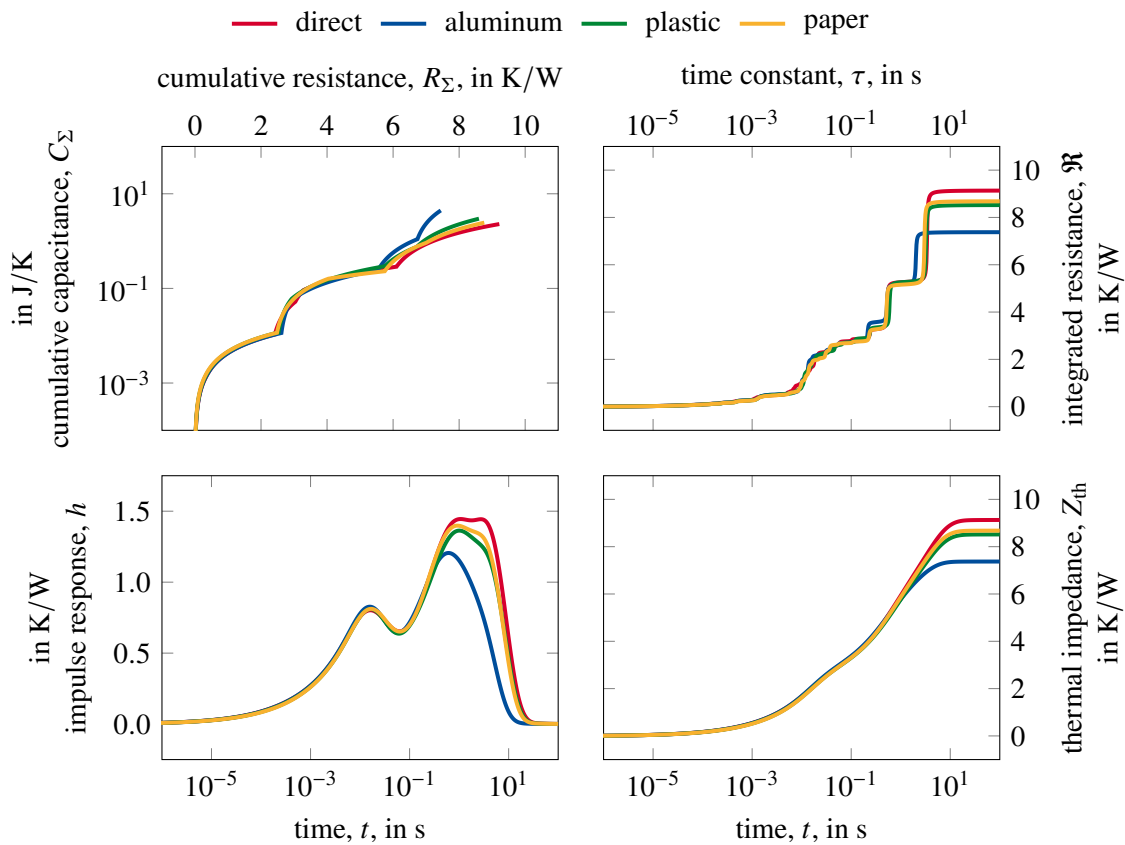
Figure 3.9: *Optimization-based network identification results for a transient dual interface test on the stand-alone high-power LED in Figure* 3.4a *using four different interface media.*

Figure 3.4a is connected to a temperature controlled heat sink. Between the LED and the heat sink, four different interface media are inserted. These are aluminum, paper, plastic, and direct contact without additional medium. No thermal grease is applied between the media. These measurements are not conducted to obtain an accurate thermal resistance but to investigate the possibilities of optimization-based network identification for transient dual interface tests.

For each interface medium, a thermal impedance is recorded and evaluated via optimization-based network identification, see Figure 3.9. Due to the good match between optimized thermal impedance and measurement thermal impedance, see Figure 3.7, the measurement data is omitted. In general, the result of a transient dual interface test consists of two thermal impedances, $Z_{\text{th},1}(t)$ and $Z_{\text{th},2}(t)$. Without loss of generality it is assumed that $Z_{\text{th},2}(t)$ is the curve with the lower thermal resistance.

For the evaluation, two variants are described in the JEDEC standard. The first option is to evaluate the point of separation between the thermal impedances and derive from it a thermal resistance. However, the difference in temperature induced by the two interface media manifests itself only slowly. From a theoretical point of view, the curves are separated from the start, even if only by
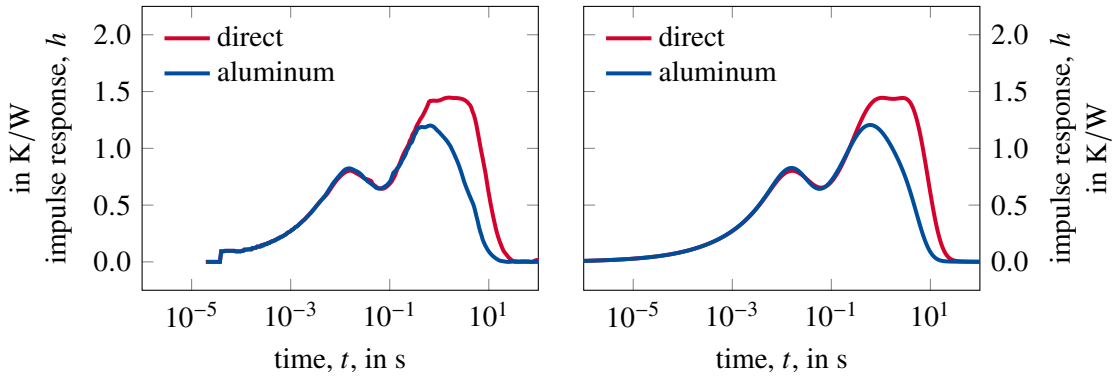
Figure 3.10: *Impulse responses for the direct contract and aluminum medium calculated via derivation (left) and optimization-based network identification (right).*

a small amount. Consequently, determining the point of separation is a matter of convention.

As a solution, the JEDEC standard introduces a small parameter, ε, that describes a minimum difference of the curves necessary for them to be considered separated. For details and limitations on how ε is defined, see [7, 42]. To achieve greater accuracy, the comparison with ε is done using the derivative of the thermal impedance, i.e. impulse response $h(z)$. The difference curve, δ, is defined as the weighted difference between the impulse responses. Note that it is a function of the second thermal impedance, $Z_{th,2}$, and not of time,

$$\delta(Z_{th,2}) = \frac{h_1 - h_2}{\Delta\theta} \ . \tag{3.4}$$

Here, $\Delta\theta$ is defined as $\Delta\theta = |Z_{th,1}(t \to \infty) - Z_{th,2}(t \to \infty)|$. The thermal resistance is then defined as the point where $\delta > \varepsilon$ is achieved.

For the transient dual interface test performed here, the results for *direct* and *aluminum* media are most suitable, as they show the earliest point of separation. Figure 3.10 shows the impulse responses for the direct contact and aluminum medium evaluated using conventional network identification, shown on the left-hand side, and using optimization-based network identification, shown on the right. The discrete step on the left-hand is an artifact of the derivation process. Figure 3.11 compares the corresponding delta curves. To avoid the separation point being obscured by noise, the standard recommends exponential fitting. Due to the low noise level, this does not seem to be necessary for optimization-based network identification. Both delta curves show oscillations between $Z_{th} \approx 1$ and $Z_{th} \approx 4$. The simultaneous presence in both results points to the measurement as a cause.

The second method described in the JEDEC standard uses the structure functions to determine the thermal resistance. This variant analyses the point of separation between the two structure functions belonging to the transient tests with and without interface medium. The standard JESD51-14 notes that the success of this method is impeded by the low accuracy of the structure function when calculated via network identification by deconvolution. Figure 3.12 shows
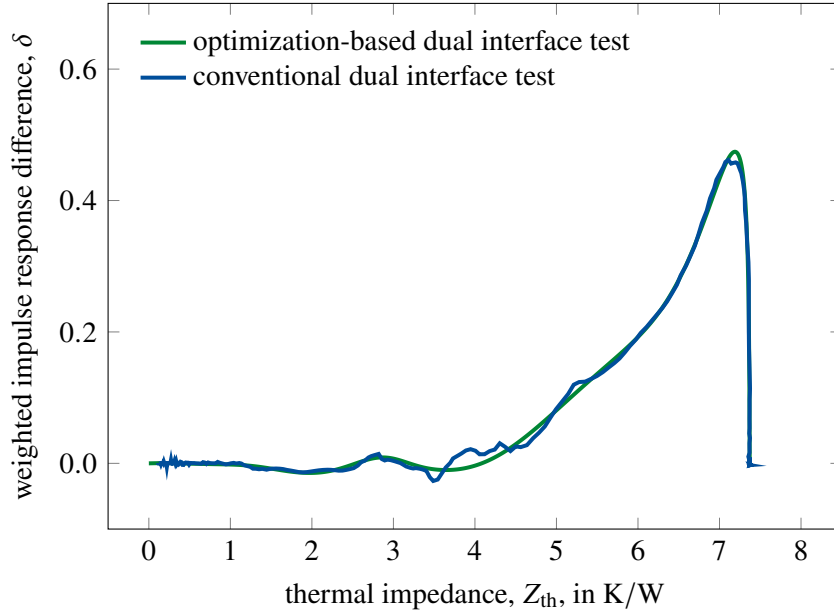
Figure 3.11: *Comparison of the δ-curves for the impulse responses shown in Figure* 3.10.
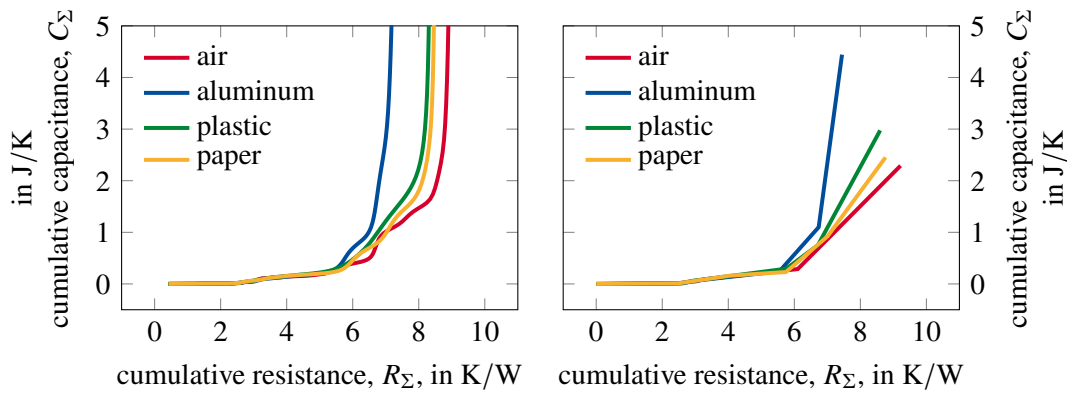
Figure 3.12: *Thermal structure functions calculated with network identification by deconvolution* (*left*) *and optimization-based network identification* (*right*).

the structure function for conventional network identification and optimization-based network identification with a linear C_Σ-axis. To determine the point of separation precisely, the difference in thermal structure functions, $\Delta C_\Sigma(R_\Sigma)$, between them is considered,

$$\Delta C_\Sigma(R_\Sigma) = C_{\Sigma,2}(R_\Sigma) - C_{\Sigma,1}(R_\Sigma) . \tag{3.5}$$

Figure 3.13 shows the delta curve between the direct contract and aluminum medium for network identification by deconvolution and optimization-based network identification. The separation point agrees between both methods. The deviation around $R_\Sigma \approx 3$, compare Figure 3.11, appears to be a feature of the measurement.
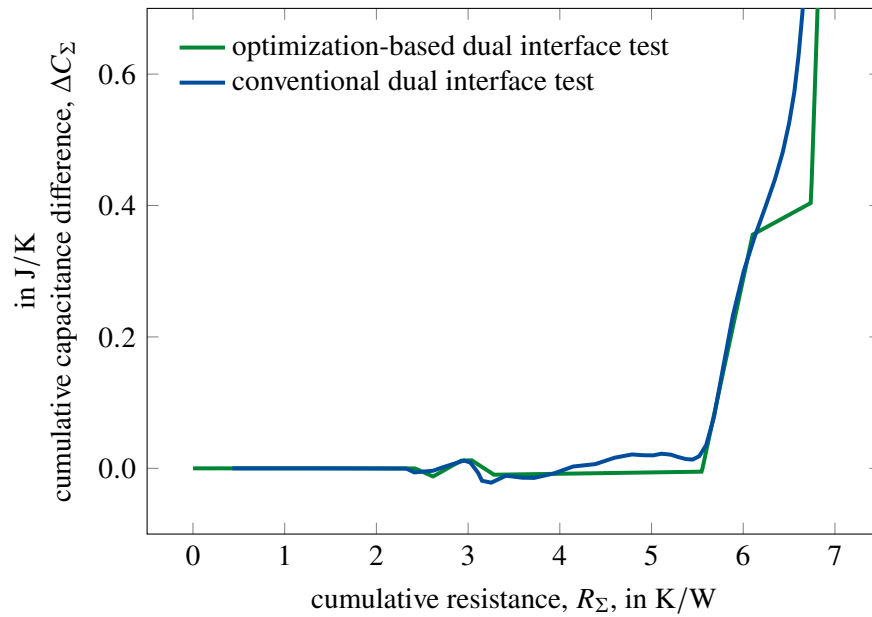
Figure 3.13: *Structure function difference for the thermal transients with direct contract and aluminum medium shown in Figure* 3.12.
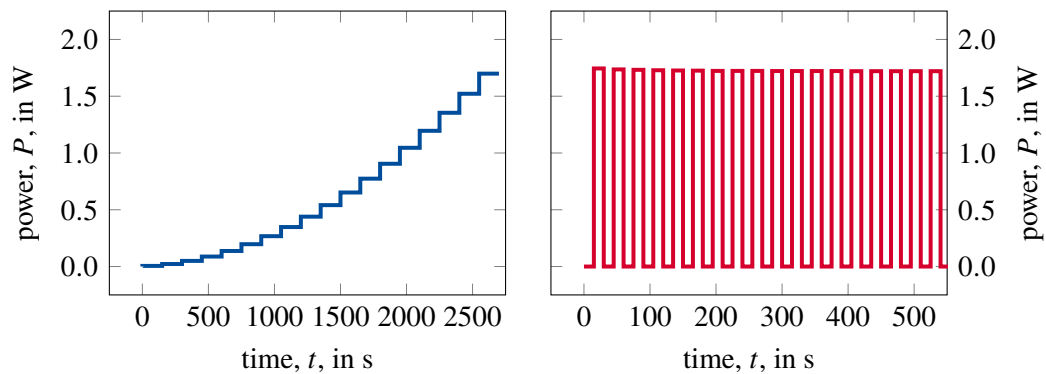
Figure 3.14: *Definition of the power functions for the temperature prediction test. A staircase excitation (left) and rectangular excitation (right) are applied.*

3.3.4 Temperature prediction test

A meaningful physical model must contain a predictive element, which can be verified or falsified in experiments. For the thermal models generated in this work, this means that given a power curve, $P(t)$, device temperatures have to be predicted accurately. In particular, the spatially resolved thermal models generated via infrared thermography require verification. Thus, a temperature prediction test is performed, which works as follows. First, a thermal equivalence circuit of a device under test is generated from a transient thermal measurement. Then the device is excited with a predefined power function (Figure 3.14) and the resulting temperature values are recorded. Independently, the temperature is predicted based on the thermal model and the power function of the excitation.

As a test subject, the heating pad sample in Figure 3.4b is used. Since it is a purely ohmic resistor, there is no forward voltage and therefore no
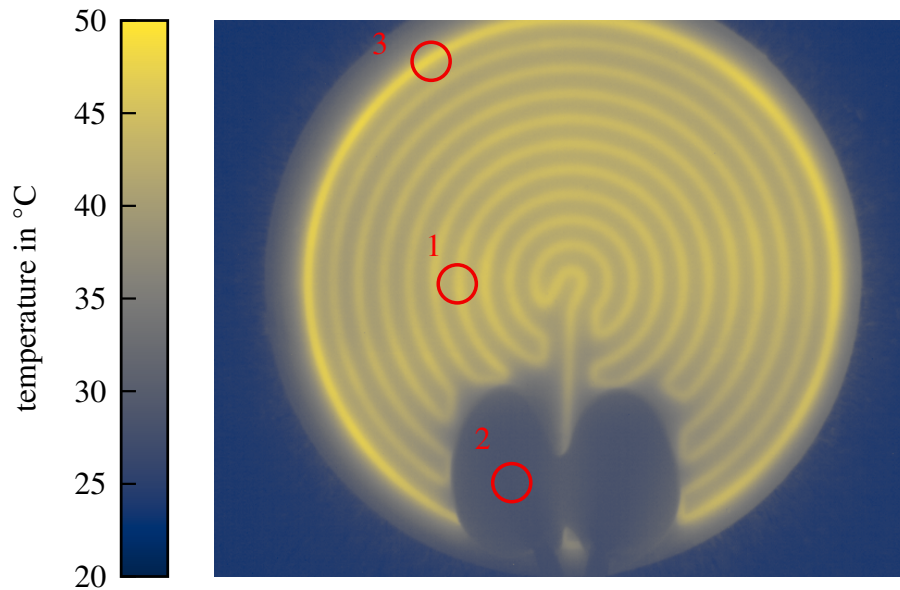
Figure 3.15: *Equilibrium temperature distribution of the black-coated heating pad, see Figure 3.4b, during the reference measurement. The three positions highlighted correspond to the curves in Figure 3.16.*

junction temperatures can be measured as possible with LEDs. Instead, infrared thermographic measurements are used to record the surface temperature of the heating pad. The equilibrium temperature distribution before the power step is shown in Figure 3.15. For LEDs, light emission makes it difficult to obtain the true power step, which is necessary for accurate predictions. For the heating pad, exactly determining the power step is simpler. Using the two-dimensional information of the image sequence, it is possible to generate independent thermal models for every part of the heating pad. The power step is assumed to have no spatial dependence. It is treated as a scalar value, constant for each pixel in the image.

For the power step in the reference measurement, the heating pad is switched from on-state to off-state, which corresponds to a cooling curve. The staircase function and rectangular excitation in Figure 3.14, on the other hand, correspond to heating curves. This translation is allowed as long as the device properties are sufficiently temperature independent. In both cases, the measurements have to start from relative thermal equilibrium. The resulting step response is evaluated at the three positions indicated in Figure 3.15. For each position, the average temperature curve of an area spanning 3×3 pixel in the center of the circle is taken. In this way, for each position and each power curve an individual temperature curve is predicted. To relate the image sequences of the reference and test measurements to each other, the infrared images have to align exactly, i. e., two equivalent pixels in the infrared images have to correspond to the same position on the heating pad.

To generate the thermal equivalence circuits, optimization-based network identifications with six sections are performed. The results are shown Figure 3.16. The thermal impedances shown in the lower right correspond to the optimized
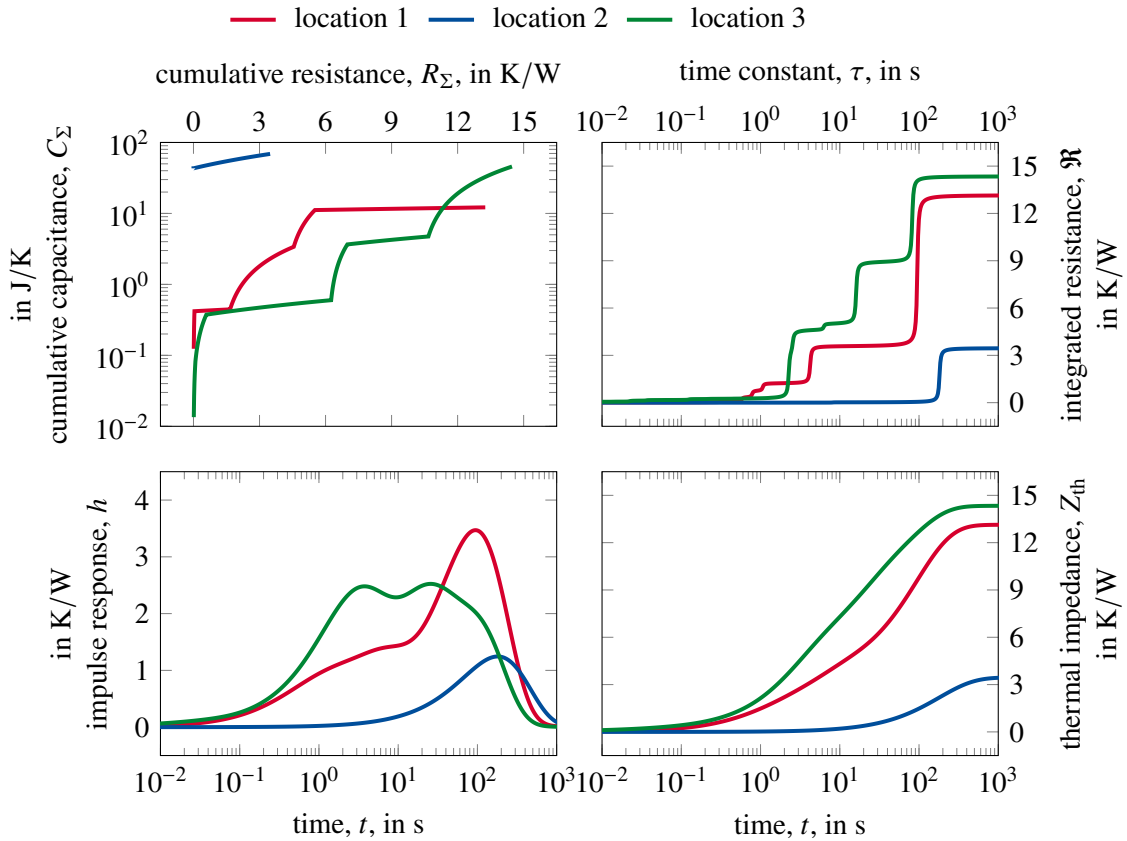
Figure 3.16: *Results of optimization-based network identifications at the three positions highlighted in Figure 3.15.*

thermal impedance. They reflect the optimized thermal impedance resulting from optimization-based network identifications. Here, the impulse response is generated by convolving the time constant spectrum. This yields a significant increase in accuracy when compared to conventional network identification by deconvolution. This advantage is especially noticeable in the prediction of fast dynamics. In addition, using the optimization-based network identification guarantees that the total thermal resistance is captured as accurately as possible.

Next, the process of generating the temperature predictions from the reference measurement is laid out in more detail. Following the theory of linear time-invariant systems, the temperature is calculated from the impulse response, $h(t)$, of the system and the power function, $P(t')$, of the excitation. The relevant definition (1.67) is reproduced for convenience,

$$T(t) = T_0 + \int_0^t P(t')h(t - t')\,\mathrm{d}t'\,. \tag{3.6}$$

Here, T_0 is the starting temperature. The impulse response, $h(t - t')$, is a function of linear time and should not be confused with the impulse response in logarithmic time, $h(z)$. They are connected via $z = \ln(t)$ and hence are

converted into each other according to,

$$h(t) = \frac{\mathrm{d}}{\mathrm{d}t} Z_{\mathrm{th}}(t) = \frac{\mathrm{d}a(z)}{\mathrm{d}z} \frac{\mathrm{d}z}{\mathrm{d}t} = h(z = \ln(t)) \frac{1}{t}. \tag{3.7}$$

Here, $Z_{\mathrm{th}}(t)$ is the thermal impedance and $a(z)$ is the step response in logarithmic time, where $Z_{\mathrm{th}}(t = \exp(z)) = a(z)$.

The logarithmic impulse responses used for the prediction are shown in the bottom left of Figure 3.16. After conversion to linear time, the spectra become significantly more sharply peaked close to the origin due to the factor $1/t$. Because of this, a dense sampling of t is required to limit the discretization error for short times. This increases the computation time significantly.

In practice, calculating $h(t)$ is easy when using the optimization-based network identification as all curves are available to high accuracy and without noise. First, the optimized thermal impedance, $a_{\mathrm{opt}}(z)$, is converted to linear time. Then, the linear time impulse response, $h(t)$, is generated by differentiating $Z_{\mathrm{th,opt}}(t)$ in linear time. As an alternative way, $h(z = \ln(t))$ is multiplied by $1/t$. For this approach, however, two small numbers have to be divided, potentially leading to numerical inaccuracies. For this reason, the former method is applied. The impulse responses obtained in this way are convolved with the staircase and rectangular power functions from Figure 3.14. For the comparison between prediction and measurement, the temperature difference, $\Delta T(t)$, is considered, which is defined as

$$\Delta T(t) = |T(t) - T_0|. \tag{3.8}$$

The three position marked in Figure 3.15 were selected because they have qualitatively different heat paths. The first position lies directly on the heating wire near the center and is dominated by the bulk behavior of the heating pad. The second position is located on top of the solder connection, compare Figure 3.4b. This position is mainly heated indirectly and reacts much slower than the rest of the sample. At the third position, the accuracy of the thermal model at the outer edge of the heating pad is tested, where it is significantly warmer, and the heat flow is geometrically restricted. For all three positions, the models generated via the optimization-based network identification achieves a good fit between optimized thermal impedance and thermal transient measurement data.

Figure 3.17 and Figure 3.18 show the measured and predicted temperature development for both excitation types at position 1. For each substep in the staircase excitation, the majority of the ensuing temperature increase happens before the next substep. The remaining temperature increase is superimposed onto the following steps. When viewed on a longer timescale or the sample reacts sufficiently slowly, the rectangular excitation is equivalent to a constant average heating power. Consequently, the resulting thermal dynamic describes an oscillation around an equilibrium, where the amplitude is determined by the time constant spectrum of the sample. For most times, both models provide temperature predictions that are within the range of variation of the measured temperature signal. In this sense, the model accurately describes the thermal
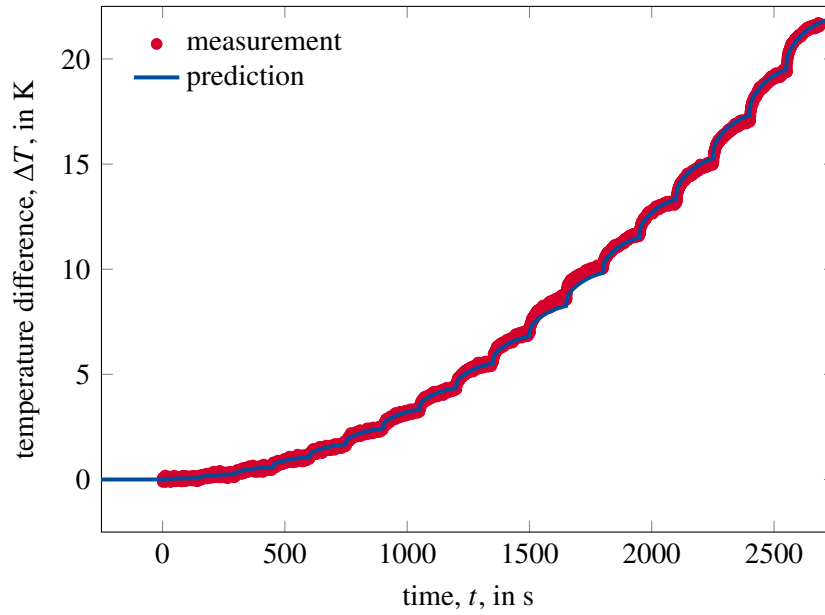
Figure 3.17: *Measured and predicted temperature rise for the staircase excitation* (*Figure* 3.14, *left*) *at position* 1.
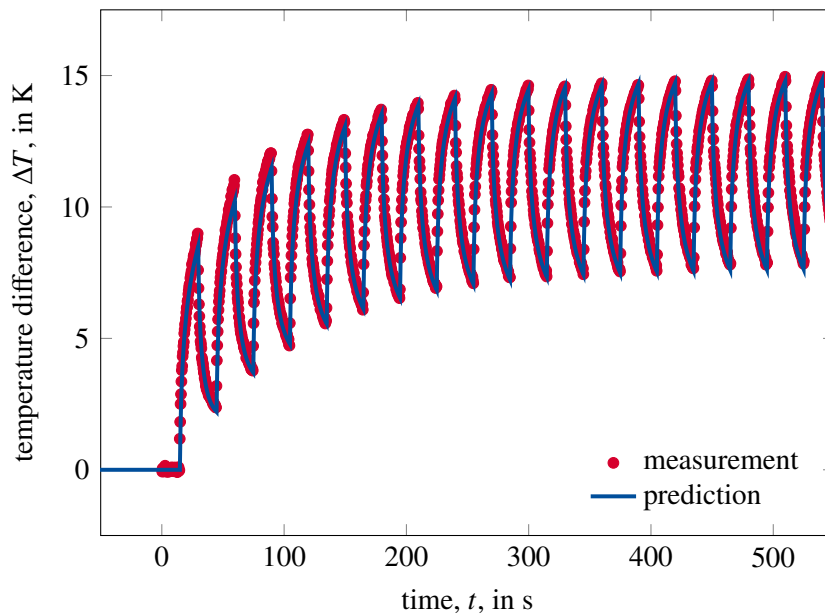

Figure 3.18: *Measured and predicted temperature rise for the rectangular excitation* (*Figure* 3.14, *right*) *at position* 1.

dynamics of the sample.

Closer inspection, however, reveals a slight deviation at approximately 1500 s for the rectangular excitation in Figure 3.17. Similarly, during the initial temperature increase in the rectangular excitation the oscillation is underestimated, see Figure 3.18. The reason for these deviations could lie in a variety of factors which are not investigated systematically in this work. In any case, the following aspects must be guaranteed for an accurate prediction. First, the power function has to be known precisely and be guaranteed to accurately reflect
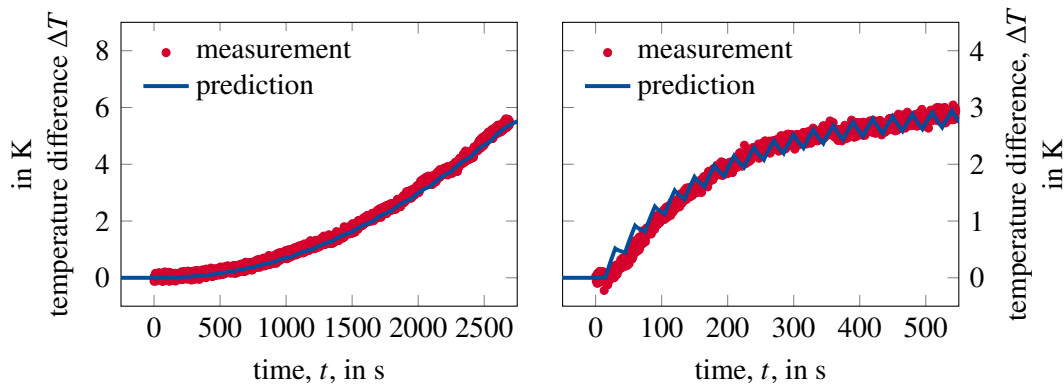
Figure 3.19: *Measured and predicted temperature rise for the staircase excitation (left) and rectangular excitation (right) at position 2.*

the energy deposition in the sample. Furthermore, inherent in the model is the assumption of linearity, which includes that $h(t)$ is independent of P and T. Given the temperature scales of the present case, the electrical resistance and thermal properties are practically independent of the temperature. Here, it is also assumed that $P(t)$ is constant over the entire sample. Furthermore, important for accurate predictions is the accuracy of the model generated by optimization-based network identification, i.e. the difference between optimized and measured thermal impedance has to be small.

As a second test case, the temperature curves at position 2 are investigated. This position is chosen to test the limits of the model. Temperature predictions at this point are particularly critical because the position is not located on the heating spiral, but on the solder connection of the cabling. At most, only a small amount of heat is generated at this point. Possibly, only indirect heating takes place. Strictly following the theory, non-heated areas cannot be represented by thermal models generated via optimization-based network identification or network identification by deconvolution. This is because part of the model assumptions is that the temperature is measured at the position of power deposition, which might be violated at position 2. As a consequence, it is not guaranteed that the thermal behavior is describable by a Cauer-type RC ladder, in which case the predictive accuracy decreases. As an alternative, it is possible to directly use the derivative of the measured thermal impedance as step response in (3.6). However, this step response does not necessarily belong to a one-dimensional thermal model as such as a piece uniform RC line.

The predicted and measured temperature curves at position 2 for the staircase and rectangular excitations are shown in Figure 3.19. Despite the theoretical concerns, for the staircase excitation the temperature is accurately predicted. The individual steps are not visible due to the high thermal inertia. For the rectangular excitation, the model predicts an oscillation with a relatively small amplitude. No oscillations are visible in the measurement, as the amplitude of the oscillation is smaller than the measurement uncertainty of the infrared camera. A deviation between prediction and measurement is visible between 0 s and 100 s.
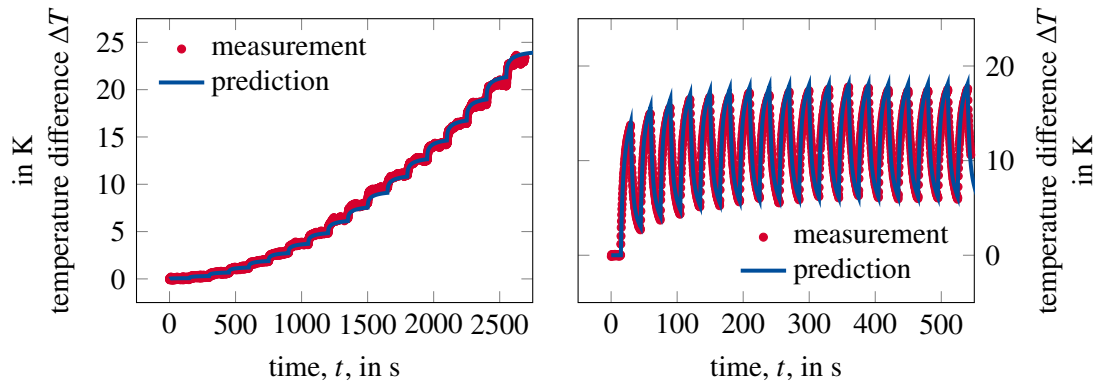
Figure 3.20: *Measured and predicted temperature rise for the staircase excitation (left) and rectangular excitation (right) at position* 3

Finally, the third position is evaluated, which is sited at the outer edge of the heating pad on the heating wire. The results are shown in Figure 3.20. At this position, the heating pad shows an immediate response. Despite the change in geometry, the predictions have similar accuracy as in the previous two cases.
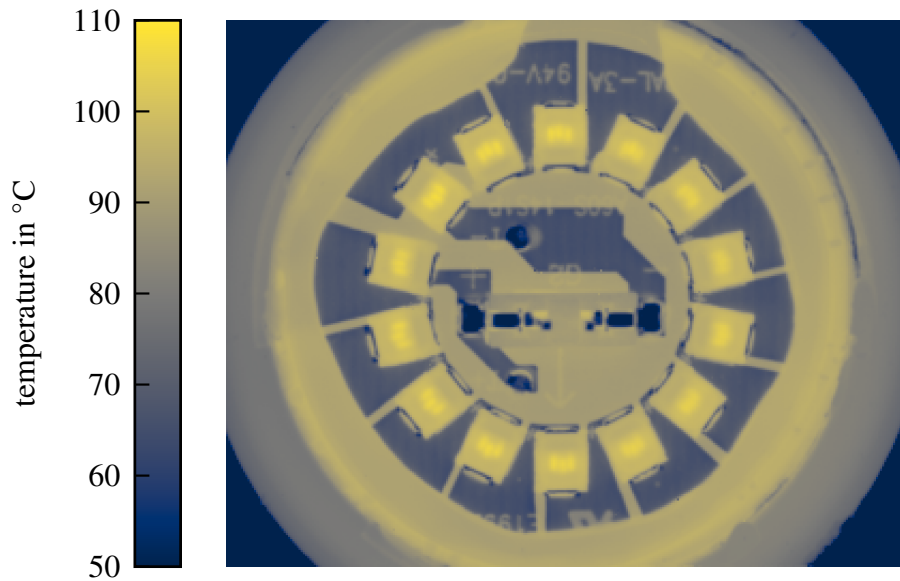
Figure 3.21: *Equilibrium temperature distribution (not emissivity corrected) for an E27 LED retrofit lamp, similar to Figure* 3.4c. *This lamp is listed as A2 in Table* 3.3.

3.4 Application examples

3.4.1 Visualizing spatially resolved spectra

In this section, thermographic network identification is applied and evaluated using electronic devices as examples. The principle of thermographic network identification is introduced and discussed in Subsection 3.2. Given a two-dimensional thermographic image sequence, for each pixel an independent network identification is performed. To limit computational time, it is advised to perform a network identification by deconvolution using Bayesian deconvolution. As a result, a non-negative spatially resolved time constant spectrum is obtained. In cases where the one-dimensional approximation is justified, the evaluation can be continued to obtain the thermal structure function.

Even if the one-dimensional model is insufficient to fully describe the three-dimensional sample, the time constant spectrum encodes well-defined information about the thermal response. This is because the impulse response is well-defined even outside one-dimensional heat conduction phenomena and the time constant spectrum is a deconvolution of the impulse response. The resistances and capacities in the corresponding Foster network do not correspond to thermal resistances and capacities. In the examples discussed in this section, heat-spreading effects are not guaranteed to be negligible. Because of that, only time constant spectra are calculated in the following.

The sample analyzed here is an LED retrofit lamp for E27 sockets. The lamp is of similar design to the one shown in Figure 3.4c. On these lamps no transient thermal measurement via the forward voltage are possible due to the integrated electronics.

Figure 3.21 shows the equilibrium temperature of the investigated lamp before the power step. For the sake of functionality, the lamp cannot be painted black

for an increased emissivity. Various electronic components as well as PCB label print are visible in the thermogram. As the light emission is not accounted for, the exact power step for each LED is unknown. Therefore, the results are only qualitative and the power, P, is set to one for all pixels.

For an initial impression of the thermal dynamics, the transient temperature averaged over one of the LEDs is examined. The resulting temperature curve is shown on the left side of Figure 3.22. In addition, the corresponding time constant spectrum is given on the right. According to the algorithm, the thermal transient is best characterized by five maxima. From the curves only, it is difficult to interpret the cooling stages of the lamp by attributing features of the thermal transient to specific components or phenomena. For later reference, the first four maxima are marked by dashed lines on the right side of Figure 3.22.

Figure 3.23 shows the spatially resolved time constant spectrum. In these images, for each pixel the amplitude of the time constant spectrum is translated into a color. Each image displays a different time constant, which is noted on the top left. To enhance the contrast, the color chart is normalized for each image. The relative magnitude between the images can be estimated from Figure 3.22. The spatially resolved time constant spectrum makes is easier to interpret the thermal transient. The images are more informative than scalar curves due to the spatial correlation.

The first maximum in Figure 3.22 lies at $\tau = 13\,\text{ms}$. The corresponding spatially resolved time constant spectrum is shown in the top left image in Figure 3.23. As the image shows, the first peak corresponds to a slight cooling at the LED chips. For detailed attribution of the maxima to chip components, more information about the structure of the lamp is necessary, which is not provided for commercial products.

The second maximum at $\tau = 132\,\text{ms}$ is related to a slower cooling also concentrated on the LEDs. This cooling stage might be related to the phosphor. Comparing the cooling behavior between the LEDs, it is apparent that the LEDs on the right side are more diffuse and have a higher average amplitude. In the other images, no difference is noticeable between the LEDs.
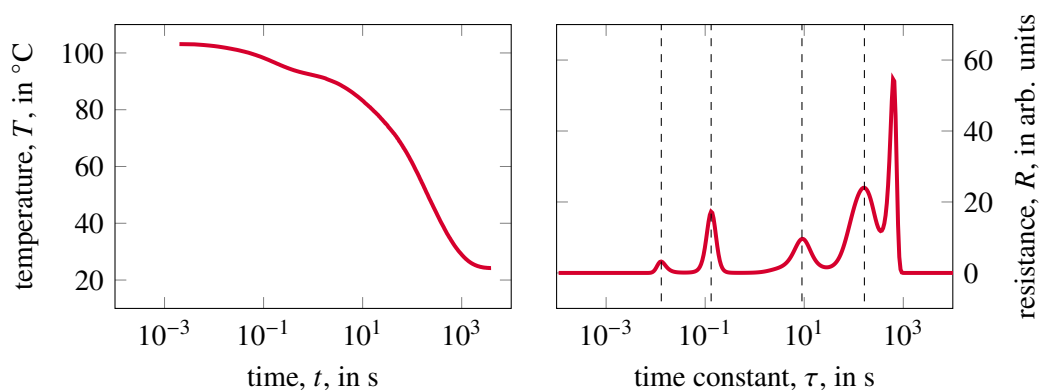
Figure 3.22: *Averaged LED temperature and corresponding time constant spectrum. The dashed lines indicate the maxima in the spectrum and correspond to the images in Figure 3.23. The lamp used is listed as A2 in Table 3.3.*
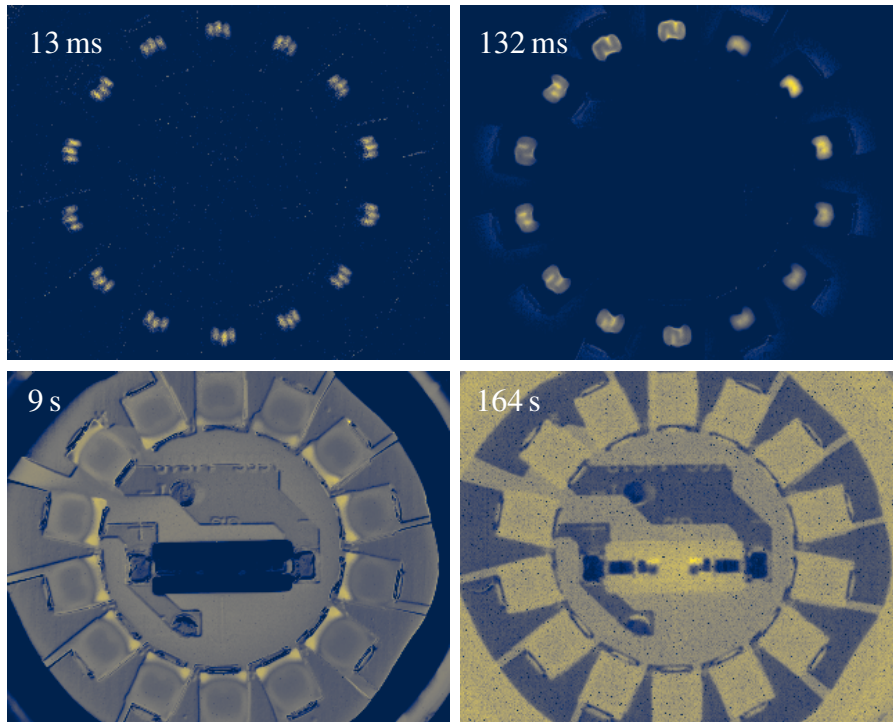
Figure 3.23: *Spatially resolved time constant spectrum for lamp A2 at four selected time constants. In Figure 3.22, the selected time constants are highlighted.*

The third maximum at $\tau = 9\,\text{s}$ is spatially more homogeneously distributed. It is interpreted to be related to the cooling of the PCB. The dark ring on the outside corresponds to the PCB gluing, which reacts even slower.

The fourth maximum at $\tau = 164\,\text{s}$ is the most homogeneous and attributed to the cooling of the lamp housing. This image would likely appear almost completely homogeneous if the temperatures were emissivity corrected. The fifth maximum has a spatial distribution which is similar to the fourth one. Further examples are presented in the proceedings of the Therminic 2020 conference [90].

3.4.2 Analyzing time constant spectra

In the previous subsection, the spatially resolved time constant spectrum is analyzed using pseudo-color images. Viewing the results of a network identification in this way allows a human observer to relatively easily comprehend a large amount of information. Through spatial correlation, features in the time constant spectrum can be attributed to components of the sample. In this subsection, a quantitative analysis of the transient thermal behavior is conducted via thermographic network identification. The influence of each component on the thermal transient is captured via its contribution to the time constant spectrum. The results discussed in this subsection are also part of the proceedings of the Therminic 2019 conference [91]. The spatially resolved time constant spectrum belonging to the LED module is not analyzed here.
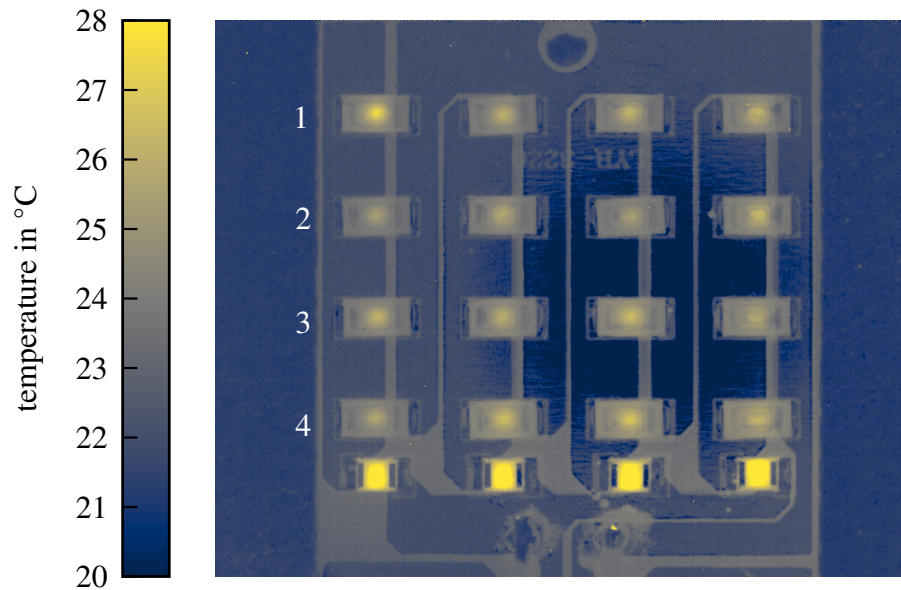
Figure 3.24: *Equilibrium temperature distribution (not emissivity corrected) of the LED module. For later reference, the rows are numbered from top to bottom.*

For this, the reader is referred to the proceedings of the Quantitative Infrared Thermography Conference (QIRT) 2020 [93].

The analysis focuses on the LED module introduced in Figure 3.4d. Its equilibrium temperature distribution (not emissivity corrected) before the thermal transient is shown in Figure 3.24. The LEDs in the module are organized into four columns comprising four LEDs each. The rows of LEDs are numbered from top to bottom for later reference. The hotspots near the bottom correspond to a row of four resistors. Additionally, the conductive paths between the LEDs are visible in the thermogram. The dark spot covering parts of the second and third row is explained by the narcissus effect. The apparently cooler temperatures are caused by a reflection of the cold detector inside the camera. This effect is visible because the module cannot be coated in black. The LEDs and conductors are not significantly affected by this, which indicates their good emissivity. Detailed analysis reveals a small temperature gradient along the sample from bottom to top. It is not visible in the thermogram, because its magnitude is on the order of a few centikelvins from top to bottom. It is induced by the asymmetrical heating power of the resistors on the bottom.

To quantify the contribution of each component in the heat path to the thermal transient, first, the temperatures are averaged for each LED. In this way, sixteen temperature curves are obtained that form the basis for the following analysis. Electrically, the power step is identical for all LEDs, neglecting light emission. Then a network identification is performed for each LED, where the deconvolution is done via Fourier deconvolution. The undershoots are an artifact of the Fourier deconvolution.

In Figure 3.25, the time constant spectrum belonging to the second LED in the third row (Figure 3.24) is shown. The time constant spectrum mainly consists of two peaks, a shorter and a longer time constant. The first peak is interpreted to
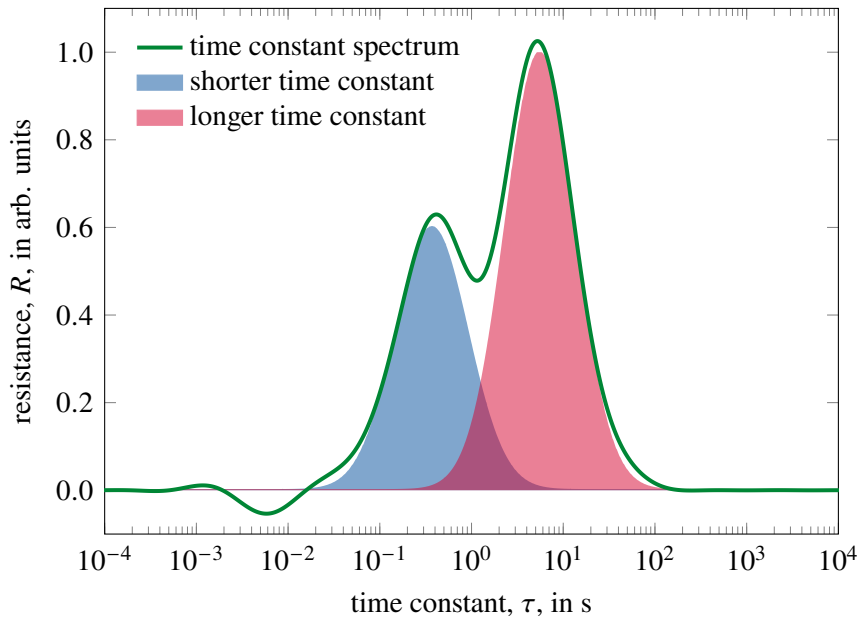
Figure 3.25: *Logarithmic time constant spectrum for the average temperature of the second LED in the third row (Figure 3.24) calculated with Fourier deconvolution.*

belong to the cooling of the LED chips, while the second peak is attributed to the cooling of the PCB. To measure the associated areas, each peak is approximated by a Gaussian function via least squares regression. The total area under the time constant spectrum is equivalent to the total thermal resistance. In this case, it is identical to the temperature difference since the power step is set to one. The time constant spectra belonging to the other transients are structurally similar to the one shown in Figure 3.25, i.e., they are also well approximated by two Gaussian functions.

The peak areas for each time constant spectrum are compiled in Figure 3.26. The areas are measured using logarithmic time, $\zeta = \ln(\tau)$. The later time constant has a relatively low variance. A clear trend of increasing contribution from the later peak with increasing row number is visible. This means the cooling of the PCB is responsible for a relatively larger part of the total temperature drop. A possible explanation are the increased temperatures in the proximity of the resistors on the bottom of the module.

The shorter time constant shows a greater variance and no increasing or decreasing trend with respect to row number is apparent. The area of the first peak is a measure of individual LED cooling performance. The outlier in the first row with a peak area almost double that of the others corresponds the top left LED in Figure 3.25. Using the time constant spectrum the heat spreading effect of the resistors can be separated to measured individual LED performances.

3.4.3 Statistical evaluation

In this subsection, the analysis of the LED retrofit lamp from Subsection 3.4.1 is continued to demonstrate the possibilities of advanced analysis using the
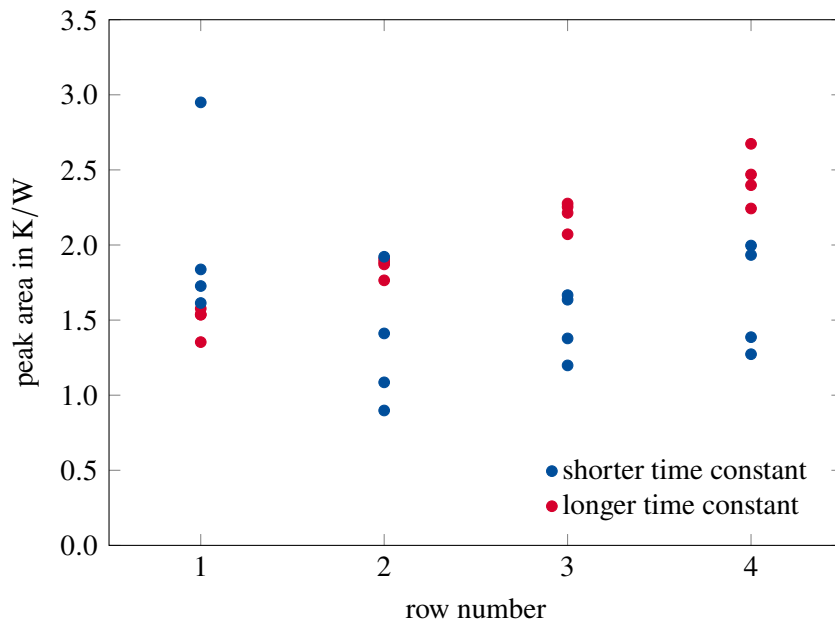
Figure 3.26: *Comparison of the peak areas according to the Gaussian approximation for all sixteen LEDs of the array split into earlier and later time constant.*

thermographic network identification. As before, the analysis focuses on the time constant spectrum of the averaged cooling curves for each LED. To enable a statistical analysis, the measurement is extended to a series of comparable LED lamps of different types. The goal is to compare the thermal paths of the LEDs to find structural differences both between and within the lamps. The lamps examined are all products from different manufacturers or variants from the same manufacturers. Still, they are all similar in design to the lamp shown as an example in Figure 3.4c. In total, eight different lamps are investigated. An overview of the technical specifications is given in Table 3.3. For each lamp, the electric power, the luminous flux, the correlated color temperature (CCT), and the number of LEDs is noted. Furthermore, two different types of lamp mountings for the E27 sockets are investigated. One mounting is made of plastic and the other is made entirely of metal. By comparing the influence of the mounting on the time constant spectra, its contribution to the heat paths is investigated. The results discussed in this subsection were presented at the LpS (LED Professional Symposium) Digital Conference and are published in the LED professional review by Peter W. Nolte, Stefan Schweizer and the author [92].

For the analysis, the thermal transients of all lamps and all LEDs are extracted from the infrared image sequences. A network identification using Bayesian deconvolution is performed on each transient. As an example, the time constant spectrum associated to the thermal transient of one of the LEDs from lamp A2 mounted on the metal socket is shown in Figure 3.27. The spectrum is identical to the one shown on the right side of Figure 3.22. Here, the analysis is continued by approximating a Gaussian function to each peak via a least squares regression. The peak area is calculated by integrating the Gaussian
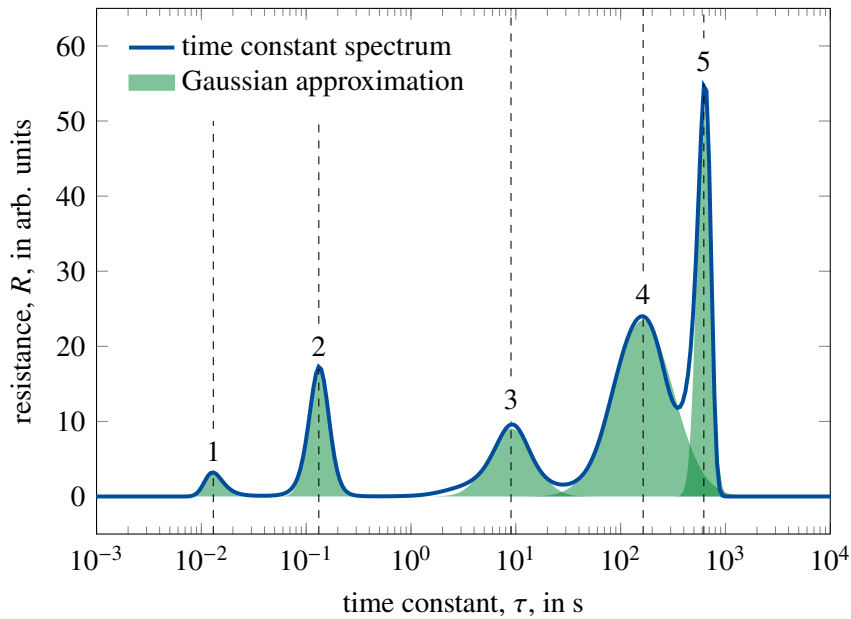
Figure 3.27: *Average time constant spectrum for one of the LEDs of lamp A2. Additionally, each of the five peaks is approximated by a Gaussian function.*

approximation analytically. In this way, each peak is attributed an area and a time constant, τ_0, the Gaussian is centered on, indicated by dashed lines in Figure 3.27. The peaks are numbered from one to five. In the previous analysis using the spatially resolved time constant spectrum, it was concluded that the first and second peak are associated to the cooling of LEDs. The third peak is related to cooling of PCB, while the fourth and fifth peak are attributed to the cooling of the entire lamp.

Figure 3.28 shows a density plot of the peak area versus center time constant, τ_0. Most time constant spectra have five maxima. Only in rare cases, the spectrum consists of four or six maxima. In total, all peaks in all spectra amount to

Table 3.3: *Specifications of all lamps which are investigated in the following. The correlated color temperature is abbreviated as CCT.*

LAMP TYPE	LUMINOUS FLUX IN LUMEN	POWER IN WATT	CCT IN KELVIN	NUMBER OF LEDs	PRODUCT
A1	806	7.5	4000	11	Philips CorePro
A2	806	8.0	2700	14	Philips CorePro
B1	806	8.5	4000	14	Osram AC17440
B2	806	8.8	2700	9	Osram AC17462
C	806	9.0	4000	19	Osram AB41763
D	1000	10.0	2700	14	IKEA LED1734G10
E	806	10.0	2700	27	ML HD95-LED
F	1055	11.0	2700	15	Philips CorePro
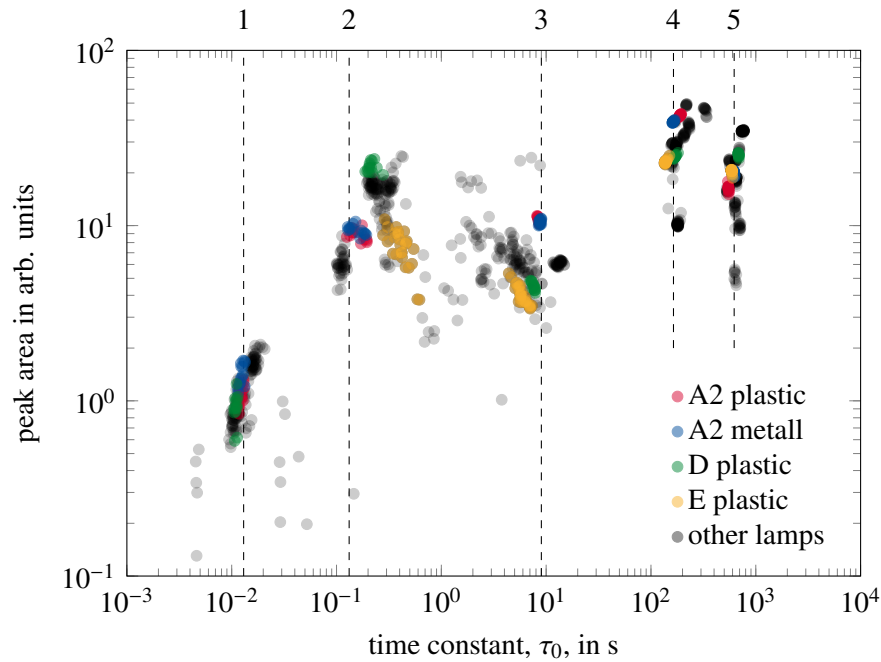
Figure 3.28: *Density plot of all peak areas versus center time constant, τ_0, for all lamps listed in Table 3.3 on a metal and plastic mounting each. Each point is partially transparent. More saturated areas imply a higher density of data points. The dashed lines correspond to the maxima of lamp A2 in Figure 3.27. At the top, the clusters are numbered from one to five.*

approximately 1000 data points. The locations of the maxima from Figure 3.27 are reproduced in Figure 3.28. For later analysis, the contributions of selected lamps are highlighted. Due to the similar structure of the lamps, the data points clearly separate into several clusters. The clusters are numbered according to the dashed lines. From the variance within the clusters, a difference in the cooling performance between the lamps and among the components of each lamp can be gathered. It is noticeable that the variance of the clusters is significantly different with respect to the peak area and the center time constant, τ_0. The clusters 1, 4, and 5 are mostly distributed in peak area. With respect to τ_0 the distribution is relatively narrow. Clusters 2 and 3 show significant variance in both dimensions.

In the following, a detailed analysis of the density plot is conducted. To discuss the influence of the mounting on the heat path, the data points for the lamp of type A2 on the metal and plastic mounting are highlighted in Figure 3.28. For both mounting types, the clusters 1, 2, and 3 lie almost exactly on top of each other. This is to be expected, because these clusters relate to the cooling of the LED and the PCB as can be seen from the spatially resolved time constant spectrum. In clusters 4 and 5, a slight difference is noticeable. However, on average no significant effect of the mounting type on equilibrium temperatures is observable. This also holds true for the other lamp types.

Next, the lamps of types D and E are compared, see Figure 3.28. The average LED equilibrium temperature for lamp D is 104 °C, while it is only 82 °C for lamp E. Both lamps have a nominal electrical power requirement of 10.0 W. A

significant difference is that lamp D consists of 14 LEDs, while lamp E has 27 LEDs. In the density plot, the largest difference is visible in cluster 2 at $\tau_0 \approx 0.3$ s, where lamp E performs significantly better. From their respective spatially resolved time constant spectra (not shown here), it is visible that these maxima for lamps D and E are also related to the LEDs. In the other clusters, the performance is relatively similar between both lamps. Lamp E has no contribution belonging to cluster one.

Comparing lamps D and E with lamp A2, it is seen that they perform significantly better in cluster 3, which partly explains lamp A2's high average LED equilibrium temperature of 104 °C. Despite this, lamp D has an equilibrium temperature similar to lamp A2 in part due to its high LED contribution in cluster 2. In fact, lamp D has the highest cluster-2 contribution of all tested LEDs. Of all lamps analyzed, lamp E has the lowest LED equilibrium temperature and in this sense the best cooling performance. Judging from the density plot, the main reason for this seems to be the low contribution of the LEDs and the PCB.

3.5 Conclusion

The goal of this chapter was to investigate the potential of network identification by deconvolution on the basis of thermographic measurements. As a first step towards that goal, a systematic analysis of the algorithms of network identification by deconvolution was conducted in Chapter 2. There, it was concluded that the presented methodology is suitable for a systematic improvement of the accuracy of existing algorithms. In addition, the method of optimization-based network identification was newly developed. The remaining task for this chapter was to analyze the accuracy of these algorithms when confronted with real measurement data as well as to explore their potential as a non-destructive testing technique.

At the beginning of this chapter, a brief summary of non-destructive testing techniques is given. Special emphasis is put on infrared thermography, which includes methods such as the thermographic signal reconstruction. Then, the method of thermographic network identification is presented, which was patented as a part of the research for this work. This sets the thermographic network identification in the context of other thermographic testing techniques.

Next, a systematic analysis of network identification by deconvolution using thermographic data is given. This completes the analysis based on theoretical test cases presented in Chapter 2. Optimization-based network identification is applied to thermal transient measurements based on forward voltages. The results are compared to network identification by deconvolution using Fourier deconvolution and Bayesian deconvolution. The success of optimization-based network identification on artificially generated measurement data presented in the previous chapter could be repeated.

To verify the thermal models generated in this way, a temperature prediction test is performed. Only if the calculated thermal models possess a predictive quality can they claim to actually describe the device under test. Using a black-coated heating pad, thermal models calculated via optimization-based

network identification were able to accurately predict the surface temperature development on multiple positions and for two different excitation patterns. As an application, the more precise calculations of optimization-based network identification are applied to transient dual interface tests with good success.

Finally, several examples for thermal analysis using thermographic network identification are given. The resulting data can be used for defect analysis as it is demonstrated on the example of an LED module. On an ensemble of LED retrofit lamps, a cluster analysis of the cooling performance of each LED is performed on the basis of the time constant spectrum. The resulting data enables a study on cooling strategies for LED retrofit lamps. Analysis using the spatially resolved time constant spectrum can assist in research and development, thermal design as well as failure mode analysis.

The achievements of thermographic network identification are the combination of network identification by deconvolution and thermographic measurements, which is a great success in achieving the goals of this work. The method enables a contactless measurement of time constant spectra without prior calibration of electric sensing property or the existence of related electric components. With the help of the spatially resolved time constant spectrum, maxima in the time constant spectrum are attributed to specific components of the device under test. In this way, the contribution of each component to the heat path is captured simultaneously. The application of optimization-based network identification to calculate spatially resolved time constant spectra from thermographic measurements is limited by the increased computational time. In this area, further algorithmic optimization is required.

Summary and outlook

Chapter 1 gives a complete overview of the theory of network identification by deconvolution. At the beginning of the chapter, the concept of lumped thermal modeling is introduced. The relation to thermal analysis using finite elements models and analytical models is established. The electrical analysis of the thermal equivalence circuits used in this work is kept as brief as possible without compromising understanding. A more detailed treatment of circuit theory is beyond the scope of this work. Nevertheless, all central equations of network identification by deconvolution are derived in detail. The sections on algorithms for performing network identification by deconvolution covers algorithms, whose use has been documented in the literature. In summary, the theoretical basis established in this work is satisfactory and does not require further expansion.

It is the task of Chapter 2 to analyze these algorithms in detail and improve their accuracy as well as to find new approaches for calculating thermal structure functions. The three main results of Chapter 2 are, first, the development of a methodology to systematically analyze the performance of algorithms for network identification by deconvolution, the optimization and comparison of existing algorithms, and finally the development of the optimization-based network identification.

For the network identification by deconvolution, some approaches remain to be systematically analyzed, such as the idea of using inverse filtering and Wiener optimal filtering for the deconvolution. For the Foster-to-Cauer transformation, the algorithms by Khatwani [74] and Sobhy [76] have not been implemented as a part of this work. Additionally, the tridiagonalization method described by Codecasa [73] remains to be systematically compared. Once these alternative algorithms have been implemented, a systematic evaluation to investigate which combination of differentiation, deconvolution and Foster-to-Cauer transformation technique yields the most accurate result for the network identification by deconvolution is possible.

The presented optimization-based network identification offers many opportunities to increase its accuracy advantage further. This includes different solvers, other ways to generate initial values, and more sophisticated optimization strategies to avoid early convergence to local minima. The goal of further work is to achieve a reduction in computation time while increasing the accuracy of the results. In the version presented, the optimization-based network identification shows better performance than the conventional algorithm already.

Chapter 3 covers the experimental aspects of the application of thermographic measurement data towards network identification by deconvolution. The main result of Chapter 3 is the development and analysis of a newly developed method

for non-destructive testing called thermographic network identification. The method has been patented [17]. The success of Chapter 2 in developing accurate algorithms for network identification provides a major benefit for the analysis in Chapter 3. A well-performing algorithm is important for increasing the detection sensitivity of the method and improving its signal-to-noise ratio. This is in particular important for the case of network identification by deconvolution as the process of deconvolution is numerically challenging.

In this work, thermographic network identification has been applied using self-heating of a device under test for example via electrical heating as described in [94]. A natural next step is to perform step heating thermography using external (optical) excitation. With this, a systematic study on the merits of thermographic network identification as a method for defect analysis is possible. This could be done by analyzing the contrast of artificial defects, for example in the form of flat-bottom hole samples, in comparison to other non-destructive testing techniques. Appropriate for this task is a comparison to thermographic signal reconstruction, which can be performed using both step and flash excitation. This makes it a good method for a comparison with thermographic network identification. As a part of such a research project it is necessary to consider a generalization of the shape of the power function applied to a device under test. In this work, only power steps from equilibrium in the form of a single Heaviside function, i. e. thermal transients, are considered. In principle, flash excitation, i. e. heating via a Dirac delta pulse or heating with a finite pulse length, are also possible. With this type of excitation different thermal responses are obtained requiring a re-evaluation of the applied algorithms.

It is a prerequisite for such a comparison to have a suitable excitation source for step heating excitation. Some progress towards such an excitation sources has been made already [112]. The approach presented in the paper uses high power infrared LEDs to provide highly controllable optical excitation outside of the detection range of the infrared camera. Another promising candidate is laser-induced heating via a vertical-cavity surface-emitting laser (VCSEL) [113, 114]. This type of laser offers a precisely controllable high-power emission, which provides homogeneously distributed heating over a relatively large area. Similar to LEDs, VCSEL emission is limited to a narrow spectral range, which does not overlap with typical infrared camera detection sensitivities. Its main advantage over LEDs is the higher irradiance.

Building on the above described steps, an automated defect classification system can be developed. The goal of such a system could be to perform a cluster analysis, similar to the one shown in Figure 3.28, to assist in quality assurance during production processes. Based on a set of reference measurements, outliers can be automatically identified and categorizing using their individual quantitative performance. Available for an automated evaluation is the entire information included in the spatially resolved time constant spectrum. The merit of such a system is that the analysis is based on the thermal resistances and capacitances of the heat path, which are the fundamental quantities when evaluating thermal performance. This work contributes a major step towards the development of such a system.

Bibliography

[1] UN General Assembly. *Transforming our world: the 2030 agenda for sustainable development*. A/RES/70/1. 2015. URL: https://www.un.org/ga/search/view_doc.asp?symbol=A/RES/70/1&Lang=E (cit. on p. 13).

[2] UN Economic and Social Council. *Progress towards the sustainable development goals: report of the secretary-general*. E/2021/58. 2021. URL: https://sustainabledevelopment.un.org/content/documents/28467E_2021_58_EN.pdf (cit. on p. 13).

[3] M. J. Loveridge et al. "Looking deeper into the galaxy (note 7)". In: *Batteries* 4.1 (2018). DOI: 10.3390/batteries4010003 (cit. on p. 13).

[4] Samsung Newsroom. *Samsung Electronics Announces Cause of Galaxy Note7 Incidents in Press Conference*. 2017. URL: https://news.samsung.com/global/samsung-electronics-announces-cause-of-galaxy-note7-incidents-in-press-conference (visited on 08/21/2021) (cit. on p. 13).

[5] U. Jahn et al. *Review on infrared and electroluminescence imaging for pv field applications*. Report IEA-PVPS T13-10:2018. International Energy Agency, Mar. 2018 (cit. on p. 13).

[6] E. A. Elsayed. "Accelerated Life Testing". In: *Handbook of Reliability Engineering*. Ed. by Hoang Pham. London: Springer London, 2003, pp. 415–428. ISBN: 978-1-85233-841-1. DOI: 10.1007/1-85233-841-5_22 (cit. on p. 13).

[7] JC-15 Thermal Characterization Techniques for Semiconductor Packages. *Transient dual interface test method for the measurement of the thermal resistance junction to case of semiconductor devices with heat flow through a single path*. Standard JESD51-14. Arlington, US: JEDEC Solid State Technology Association, Nov. 2010 (cit. on pp. 15, 42, 45, 48, 49, 52, 94, 96).

[8] V. Székely. "THERMODEL: a tool for compact dynamic thermal model generation". In: *Microelectronics Journal* 29.4 (1998), pp. 257–267. DOI: 10.1016/S0026-2692(97)00065-7 (cit. on pp. 15, 43, 49).

[9] V. Székely. "Identification of RC networks by deconvolution: chances and limits". In: *IEEE Transactions on Circuits and Systems I: Fundamental Theory and Applications* 45.3 (1998), pp. 244–258. DOI: 10.1109/81.662698 (cit. on pp. 15, 42, 45, 51).

[10] M. Schmid et al. "A new noise-suppression algorithm for transient thermal analysis in semiconductors over pulse superposition". In: *IEEE Transactions on Instrumentation and Measurement* 70 (2021), pp. 1–9. DOI: 10.1109/TIM.2020.3011818 (cit. on pp. 15, 47, 51).

[11] K. A. Pareek et al. "Effect of different deconvolution methods on structure function calculation". In: *26th International Workshop on Thermal Investigations of ICs and Systems (THERMINIC)*. 2020, pp. 97–104. DOI: 10.1109/THERMINIC49743.2020.9420505 (cit. on p. 15).

[12] A. Szalai and V. Székely. "Possible acception criteria for structure functions". In: *Microelectronics Journal* 43.2 (2012), pp. 164–168. DOI: 10.1016/j.mejo.2011.08.010 (cit. on pp. 15, 44, 52, 79).

[13] S. M. Shepard et al. "Reconstruction and enhancement of active thermographic image sequences". In: *Optical Engineering* 42.5 (2003), pp. 1337–1342. DOI: 10.1117/1.1566969 (cit. on pp. 16, 84).

[14] H. Czichos. *Handbook of technical diagnostics: fundamentals and application to structures and systems*. Springer Berlin Heidelberg, 2013. DOI: 10.1007/978-3-642-25850-3 (cit. on pp. 16, 83–85).

[15] D. L. Balageas et al. "The thermographic signal reconstruction method: a powerful tool for the enhancement of transient thermographic images". In: *Biocybernetics and Biomedical Engineering* 35.1 (2015), pp. 1–9. DOI: 10.1016/j.bbe.2014.07.002 (cit. on pp. 16, 84, 85).

[16] A. Schager et al. "Extension of the thermographic signal reconstruction technique for an automated segmentation and depth estimation of subsurface defects". In: *Journal of Imaging* 6.9 (2020). ISSN: 2313-433X. DOI: 10.3390/jimaging6090096 (cit. on pp. 16, 84, 85).

[17] P. W. Nolte, N. J. Ziegeler, and S. Schweizer. "Verfahren zur Bestimmung der ortsaufgelösten thermischen Strukturfunktion und/oder Zeitkonstantenspektren eines Objekts". Deutsches Patent- und Markenamt Patentschrift DE 10 2019 214 472 B3. Fachhochschule Südwestfalen and Fraunhofer-Gesellschaft zur Förderung der angewandten Forschung e.V. Dec. 17, 2020 (cit. on pp. 17, 85, 116).

[18] D. W. Hahn and M. N. Özişik. "Heat Conduction Fundamentals". In: *Heat Conduction*. John Wiley and Sons, Ltd, 2012. Chap. 1, pp. 1–39. ISBN: 9781118411285. DOI: 10.1002/9781118411285.ch1 (cit. on p. 19).

[19] L. M. Jiji. *Heat Conduction*. Springer Berlin Heidelberg, 2009. ISBN: 9783642012679. DOI: 10.1007/978-3-642-01267-9 (cit. on p. 22).

[20] H. I. Rosten and C. J. M. Lasance. "DELPHI: The development of libraries of physical models of electronic components for an integrated design environment". In: *Model Generation in Electronic Design*. Boston, MA: Springer US, 1995. Chap. 5, pp. 63–89. DOI: 10.1007/978-1-4615-2335-2_5 (cit. on p. 23).

[21] C. J. M Lasance. "Ten years of boundary-condition-independent compact thermal modeling of electronic parts: A review". In: *Heat Transfer Engineering* 29.2 (2008), pp. 149–168. DOI: 10.1080/01457630701673188 (cit. on pp. 23, 24, 45).

[22] C. J. M. Lasance. "The European project PROFIT: prediction of temperature gradients influencing the quality of electronic products". In: *Seventeenth Annual IEEE Semiconductor Thermal Measurement and Management Symposium*. 2001, pp. 120–125. DOI: 10.1109/STHERM.2001.915160 (cit. on p. 23).

[23] JC-15 Thermal Characterization Techniques for Semiconductor Packages. *Methodology for the thermal measurement of component packages (single semiconductor device)*. Standard EIA/JESD51-1. Arlington, US: Electronic Industries Association, JEDEC Solid State Technology Association, Dec. 1995 (cit. on p. 24).

[24] JC-15 Thermal Characterization Techniques for Semiconductor Packages. *Thermal modeling overview*. Standard JESD15. Arlington, US: JEDEC Solid State Technology Association, Oct. 2008 (cit. on p. 24).

[25] L. Codecasa et al. "Matrix reduction tool for creating boundary condition independent dynamic compact thermal models". In: *21st International Workshop on Thermal Investigations of ICs and Systems (THERMINIC)*. 2015, pp. 1–5. DOI: 10.1109/THERMINIC.2015.7389596 (cit. on p. 25).

[26] L. Codecasa et al. "Fast novel thermal analysis simulation tool for integrated circuits (FANTASTIC)". In: *20th International Workshop on Thermal Investigations of ICs and Systems (THERMINIC)*. 2014, pp. 1–6. DOI: 10.1109/THERMINIC.2014.6972507 (cit. on p. 25).

[27] L. Codecasa et al. "Thermal resistance advanced calculator (TRAC)". In: *24rd International Workshop on Thermal Investigations of ICs and Systems (THERMINIC)*. 2018, pp. 1–5. DOI: 10.1109/THERMINIC.2018.8593333 (cit. on p. 25).

[28] L. Codecasa et al. "Thermal resistance and impedance calculator (TRIC)". In: *25th International Workshop on Thermal Investigations of ICs and Systems (THERMINIC)*. 2019, pp. 1–5. DOI: 10.1109/THERMINIC.2019.8923605 (cit. on p. 25).

[29] P. Pasquier and D. Marcotte. "Short-term simulation of ground heat exchanger with an improved TRCM". In: *Renewable Energy* 46 (2012), pp. 92–99. DOI: https://doi.org/10.1016/j.renene.2012.03.014 (cit. on p. 25).

[30] P. Pasquier and D. Marcotte. "Joint use of quasi-3D response model and spectral method to simulate borehole heat exchanger". In: *Geothermics* 51 (2014), pp. 281–299. ISSN: 0375-6505. DOI: 10.1016/j.geothermics.2014.02.001 (cit. on p. 25).

[31] P. Pasquier. "Interpretation of the first hours of a thermal response test using the time derivative of the temperature". In: *Applied Energy* 213 (2018), pp. 56–75. DOI: 10.1016/j.apenergy.2018.01.022 (cit. on p. 25).

[32] P. Pasquier, A. Zarrella, and D. Marcotte. "A multi-objective optimization strategy to reduce correlation and uncertainty for thermal response test analysis". In: *Geothermics* 79 (2019), pp. 176–187. DOI: 10.1016/j.geothermics.2019.02.003 (cit. on p. 25).

[33] R. Unbehauen. *Systemtheorie 1*. 8. korrigierte Auflage. Oldenbourg: De Gruyter, 2002. ISBN: 3486259997 (cit. on p. 27).

[34] R. Unbehauen. *Systemtheorie 2*. 7. überarbeitete und erweiterte Auflage. Oldenbourg: De Gruyter, 1998. ISBN: 9783486240238 (cit. on p. 27).

[35] J. Distefano. *Schaum's outline of feedback and control systems*. 3. Edition. McGraw-Hill Education Ltd, 2013. ISBN: 9780071829489 (cit. on p. 28).

[36] W.-K. Chen. *Feedback, nonlinear, and distributed circuits*. The Circuits and Filters Handbook, 3rd Edition. CRC Press, 2009. ISBN: 9781351835053 (cit. on pp. 33, 35, 36).

[37] E. N. Protonotarios and O. Wing. "Theory of nonuniform RC lines, part I: analytic properties and realizability conditions in the frequency domain". In: *IEEE Transactions on Circuit Theory* 14.1 (1967), pp. 2–12. DOI: 10.1109/TCT.1967.1082650 (cit. on p. 36).

[38] E. N. Protonotarios and O. Wing. "Theory of nonuniform RC lines, part II: analytic properties in the time domain". In: *IEEE Transactions on Circuit Theory* 14.1 (1967), pp. 13–20. DOI: 10.1109/TCT.1967.1082651 (cit. on p. 36).

[39] V. Székely. "On the representation of infinite-length distributed RC one-ports". In: *IEEE Transactions on Circuits and Systems* 38.7 (1991), pp. 711–719. DOI: 10.1109/31.135743 (cit. on p. 39).

[40] W. Van Assche. *The impact of Stieltjes' work on continued fractions and orthogonal polynomials*. 1993. arXiv: math/9307220 [math.CA] (cit. on p. 41).

[41] D. Schweitzer, H. Pape, and L. Chen. "Transient measurement of the junction-to-case thermal resistance using structure functions: chances and limits". In: *Twenty-fourth Annual IEEE Semiconductor Thermal Measurement and Management Symposium*. 2008, pp. 191–197. DOI: 10.1109/STHERM.2008.4509389 (cit. on pp. 44, 46).

[42] A. Poppe et al. "Suggestions for extending the scope of the transient dual interface method". In: *27th International Workshop on Thermal Investigations of ICs and Systems (THERMINIC)*. 2021, pp. 23–30 (cit. on pp. 44, 94, 96).

[43] D. Schweitzer et al. "How to evaluate transient dual interface measurements of the Rth-JC of power semiconductor packages". In: *2009 25th Annual IEEE Semiconductor Thermal Measurement and Management Symposium*. 2009, pp. 172–179. DOI: 10.1109/STHERM.2009.4810760 (cit. on p. 44).

[44] L. Codecasa. "Canonical forms of one-port Passive Distributed thermal networks". In: *IEEE Transactions on Components and Packaging Technologies* 28.1 (2005), pp. 5–13. DOI: 10.1109/TCAPT.2004.843182 (cit. on p. 45).

[45] L. Codecasa et al. "Accurate and efficient algorithm for computing structure functions from the spatial distribution of thermal properties in electronic devices". In: *IEEE Transactions on Electron Devices* (2021), pp. 1–8. DOI: 10.1109/TED.2021.3073647 (cit. on pp. 45, 47).

[46] M.-N. Sabry. "Dynamic compact thermal models used for electronic design: a review of recent progress". In: vol. 1. International Electronic Packaging Technical Conference and Exhibition. July 2003, pp. 399–415. DOI: 10.1115/IPACK2003-35185 (cit. on p. 45).

[47] J. W. Sofia. "Analysis of thermal transient data with synthesized dynamic models for semiconductor devices". In: *IEEE Transactions on Components, Packaging, and Manufacturing Technology: Part A* 18.1 (1995), pp. 39–47. DOI: 10.1109/95.370733 (cit. on p. 45).

[48] G. Oliveti, A. Piccirillo, and P.E. Bagnoli. "Analysis of laser diode thermal properties with spatial resolution by means of the TRAIT method". In: *Microelectronics Journal* 28.3 (1997), pp. 293–300. DOI: 10.1016/S0026-2692(96)00032-8 (cit. on p. 45).

[49] V. Székely and T. Van Bien. "Fine structure of heat flow path in semiconductor devices: A measurement and identification method". In: *Solid-State Electronics* 31.9 (1988), pp. 1363–1368. DOI: 10.1016/0038-1101(88)90099-8 (cit. on p. 45).

[50] JC-15 Thermal Characterization Techniques for Semiconductor Packages. *Integrated circuits thermal measurement method - electrical test method (single semiconductor device)*. Standard EIA/JESD51-1. Arlington, US: Electronic Industries Association, JEDEC Solid State Technology Association, Dec. 1995 (cit. on p. 45).

[51] R. P. Stout and D. T. Billings. "How to extend a thermal-RC-network model (derived from experimental data) to respond to an arbitrarily fast input". In: *Fourteenth Annual IEEE Semiconductor Thermal Measurement and Management Symposium (Cat. No.98CH36195)*. 1998, pp. 8–15. DOI: 10.1109/STHERM.1998.660381 (cit. on p. 45).

[52] P. Szabo et al. "Short time die attach characterization of leds for in-line testing application". In: *2006 8th Electronics Packaging Technology Conference*. 2006, pp. 360–366. DOI: 10.1109/EPTC.2006.342743 (cit. on pp. 45, 47).

[53] JC-25 Committee on Transistors. *Thermal impedance measurement for insulated gate bipolar transistors (delta VCE(on) method)*. Standard JESD25-12. Arlington, US: JEDEC Solid State Technology Association, June 2004 (cit. on p. 46).

[54] JC-15 Thermal Characterization Techniques for Semiconductor Packages. *Implementation of the electrical test method for the measurement of real thermal resistance and impedance of light-emitting diodes with exposed cooling*. Standard JESD51-51. Arlington, US: JEDEC Solid State Technology Association, Apr. 2012 (cit. on p. 46).

[55] JC-15 Thermal Characterization Techniques for Semiconductor Packages. *Guidelines for combining CIE 127-2007 total flux measurements with thermal measurements of leds with exposed cooling surface*. Standard JESD51-52. Arlington, US: JEDEC Solid State Technology Association, Apr. 2012 (cit. on p. 46).

[56] C. J. M. Lasance and A. Poppe. *Thermal Management for LED Applications*. Solid State Lighting Technology and Application Series. Springer New York, 2016. ISBN: 9781493941339 (cit. on pp. 46, 48, 52).

[57] M. Rencz et al. "Increasing the accuracy of structure function based thermal material parameter measurements". In: *IEEE Transactions on Components and Packaging Technologies* 28.1 (2005), pp. 51–57. DOI: 10.1109/TCAPT.2004.843204 (cit. on p. 46).

[58] V. Székely and A. Szalai. "Measurement of the time-constant spectrum: systematic errors, correction". In: *Microelectronics Journal* 43.11 (2012), pp. 904–907. DOI: 10.1016/j.mejo.2012.05.011 (cit. on p. 46).

[59] M. Schmid et al. "Time saving averaging algorithm for transient thermal analyses over deterministic pulse superposition". In: *25th International Workshop on Thermal Investigations of ICs and Systems (THERMINIC)*. 2019. DOI: 10.1109/THERMINIC.2019.8923548 (cit. on pp. 47, 48).

[60] F. N. Masana. "Thermal impedance measurements under non-equilibrium conditions. How to extend its validity". In: *Microelectronics Reliability* 48.4 (2008), pp. 563–568. DOI: 10.1016/j.microrel.2007.11.005 (cit. on p. 47).

[61] V. Szekely. "Evaluation of short pulse thermal transient measurements". In: *14th International Workshop on Thermal Inveatigation of ICs and Systems*. 2008, pp. 20–25. DOI: 10.1109/THERMINIC.2008.4669872 (cit. on pp. 47, 49, 52).

[62] Y. Ezzahri and A. Shakouri. "Application of network identification by deconvolution method to the thermal analysis of the pump-probe transient thermoreflectance signal". In: *Review of Scientific Instruments* 80.7 (2009), p. 074903. DOI: 10.1063/1.3176463 (cit. on pp. 47, 48, 51).

[63] L. Codecasa, D. D'Amore, and P. Maffezzoni. "Multipoint moment matching reduction from port responses of dynamic thermal networks". In: *IEEE Transactions on Components and Packaging Technologies* 28.4 (2005), pp. 605–614. DOI: 10.1109/TCAPT.2005.859741 (cit. on p. 47).

[64] D. Rafiq and M. A. Bazaz. "Model order reduction via moment-matching: a state of the art review". In: *Archives of Computational Methods in Engineering* (2021), pp. 1–21 (cit. on p. 47).

[65] S. R. Krishnan and C. S. Seelamantula. "On the selection of optimum savitzky-golay filters". In: *IEEE Transactions on Signal Processing* 61.2 (2013), pp. 380–391. DOI: 10.1109/TSP.2012.2225055 (cit. on pp. 47, 54).

[66] S. M. Kay. *Fundamentals of statistical signal processing, volume 1: estimation theory*. 1st. Prentice Hall Signal Processing Series. Pearson Education, 1993. ISBN: 9788131728994 (cit. on p. 47).

[67] J. G. Proakis and D. G. Manolakis. *Digital signal processing principles, algorithms, and applications*. 4th. Prentice Hall, 2006 (cit. on p. 49).

[68] W. H. Press et al. *Numerical recipes 3rd edition: the art of scientific computing*. 3rd ed. USA: Cambridge University Press, 2007. ISBN: 0521880688 (cit. on pp. 49, 55).

[69] T. J. Kennett, W. V. Prestwich, and A. Robertson. "Bayesian deconvolution I: Convergent properties". In: *Nuclear Instruments and Methods* 151.1 (1978), pp. 285–292. DOI: 10.1016/0029-554X(78)90502-5 (cit. on p. 49).

[70] T. J. Kennett, W. V. Prestwich, and A. Robertson. "Bayesian deconvolution II: noise properties". In: *Nuclear Instruments and Methods* 151.1 (1978), pp. 293–301. DOI: 10.1016/0029-554X(78)90503-7 (cit. on p. 49).

[71] T. J. Kennett et al. "Bayesian deconvolution III: applications and algorithm implementation". In: *Nuclear Instruments and Methods* 153.1 (1978), pp. 125–135. DOI: 10.1016/0029-554X(78)90628-6 (cit. on p. 49).

[72] V. Székely. "Enhancing reliability with thermal transient testing". In: *Microelectronics Reliability* 42.4 (2002), pp. 629–640. DOI: 10.1016/S0026-2714(02)00028-8 (cit. on p. 51).

[73] L. Codecasa, D. D'Amore, and P. Maffezzoni. "Physical interpretation and numerical approximation of structure functions of components and packages". In: *Semiconductor Thermal Measurement and Management IEEE Twenty First Annual IEEE Symposium*. 2005, pp. 146–153. DOI: 10.1109/STHERM.2005.1412171 (cit. on pp. 51, 115).

[74] K. J. Khatwani, J. S. Bajwa, and H. Singh. "Determining elements of lossy ladder networks". In: *Electronics Letters* 12 (3 1976), pp. 87–88 (cit. on pp. 51, 115).

[75] R. Srinivasagopalan and G. Martens. "Formulas for the elements of lossy low-pass ladder networks". In: *IEEE Transactions on Circuit Theory* 19.4 (1972), pp. 360–365. DOI: 10.1109/TCT.1972.1083467 (cit. on p. 51).

[76] M. Sobhy. "Elements of lossy ladder networks". In: *IEEE Transactions on Circuit Theory* 20.5 (1973), pp. 614–615. DOI: 10.1109/TCT.1973.1083724 (cit. on pp. 51, 115).

[77] Y. C. Gerstenmaier, W. Kiffe, and G. Wachutka. "Combination of thermal subsystems modeled by rapid circuit transformation". In: *13th International Workshop on Thermal Investigation of ICs and Systems (THERMINIC)*. 2007, pp. 115–120. DOI: 10.1109/THERMINIC.2007.4451758 (cit. on p. 51).

[78] V. Szekely and M. Rencz. "Thermal dynamics and the time constant domain". In: *IEEE Transactions on Components and Packaging Technologies* 23.3 (2000), pp. 587–594. DOI: 10.1109/6144.868862 (cit. on p. 52).

[79] N. J. Ziegeler, P. W. Nolte, and S. Schweizer. "Optimization-based network identification for thermal transient measurements on LEDs". In: *27th International Workshop on Thermal Investigations of ICs and Systems (THERMINIC)*. 2021, pp. 23–30. DOI: 10.1109/THERMINIC52472.2021.9626491 (cit. on pp. 53, 81).

[80] N. J. Ziegeler, P. W. Nolte, and S. Schweizer. "Quantitative performance comparison of thermal structure function computations". In: *Energies* 14.21 (2021). DOI: 10.3390/en14217068 (cit. on p. 53).

[81] N. J. Ziegeler, P. W. Nolte, and S. Schweizer. "Optimization-based network identification for thermal transient measurements". In: *Energies* 14.22 (2021). DOI: 10.3390/en14227648 (cit. on p. 53).

[82] C. R. Harris et al. "Array programming with NumPy". In: *Nature* 585.7825 (Sept. 2020), pp. 357–362. DOI: 10.1038/s41586-020-2649-2 (cit. on p. 53).

[83] P. Virtanen et al. "SciPy 1.0: Fundamental Algorithms for Scientific Computing in Python". In: *Nature Methods* 17 (2020), pp. 261–272. DOI: 10.1038/s41592-019-0686-2 (cit. on p. 53).

[84] C. Van Horsen, A. Martelli, and P. Peterson. *General multi-precision arithmetic for python 2.6+/3+ (gmp, mpir, mpfr, mpc)*. 2000. URL: https://github.com/aleaxit/gmpy (cit. on p. 53).

[85] K.M.M. Prabhu. *Window functions and their applications in signal processing*. CRC Press, 2018. ISBN: 9781466515840 (cit. on p. 56).

[86] A. Nuttall. "Some windows with very good sidelobe behavior". In: *IEEE Transactions on Acoustics, Speech, and Signal Processing* 29.1 (1981), pp. 84–91. DOI: 10.1109/TASSP.1981.1163506 (cit. on p. 56).

[87]   M. J. D. Powell. "An efficient method for finding the minimum of a function of several variables without calculating derivatives". In: *The Computer Journal* 7.2 (Jan. 1964), pp. 155–162. ISSN: 0010-4620. DOI: `10.1093/comjnl/7.2.155` (cit. on p. 61).

[88]   M. J. D. Powell and J.-P. Hennart. "A direct search optimization method that models the objective and constraint functions by linear interpolation". In: *Advances in optimization and numerical analysis*. Dordrecht: Springer Netherlands, 1994, pp. 51–67. DOI: `10.1007/978-94-015-8330-5_4` (cit. on p. 61).

[89]   B. Efron and T. Hastie. *Computer age statistical inference*. Institute of Mathematical Statistics Monographs. Cambridge University Press, 2016. DOI: `10.1017/CBO9781316576533` (cit. on pp. 67, 68).

[90]   N. J. Ziegeler, P. W. Nolte, and S. Schweizer. "Thermal equivalence networks for analysis of transient thermographic data". In: *26th International Workshop on Thermal Investigations of ICs and Systems (THERMINIC)*. 2020, pp. 226–231. DOI: `10.1109/THERMINIC49743.2020.9420520` (cit. on pp. 81, 107).

[91]   N. J. Ziegeler, P. W. Nolte, and S. Schweizer. "Application of infrared thermography to thermal transient measurements". In: *25th International Workshop on Thermal Investigations of ICs and Systems (THERMINIC)*. 2019, pp. 1–4. DOI: `10.1109/THERMINIC.2019.8923882` (cit. on pp. 81, 107).

[92]   P. W. Nolte, N. J. Ziegeler, and S. Schweizer. "Analysis of heat paths in led retrofit lamps". In: *LED professional Review* 82 (2020), pp. 54–57 (cit. on pp. 81, 110).

[93]   N. J. Ziegeler, P. W. Nolte, and S. Schweizer. "Transient thermographic heat path analysis using spatially resolved thermal equivalent networks". In: *15th Quantitative InfraRed Thermography Conference*. 2020. DOI: `10.21611/qirt.2020.037` (cit. on pp. 81, 108).

[94]   N. J. Ziegeler, P. W. Nolte, and S. Schweizer. "Thermographic network identification for transient thermal heat path analysis". In: *Quantitative InfraRed Thermography Journal* (2022). DOI: `10.1080/17686733.2022.2033529` (cit. on pp. 81, 116).

[95]   P. Aryan, S. Sampath, and H. Sohn. "An overview of non-destructive testing methods for integrated circuit packaging inspection". In: *Sensors* 18.7 (2018). DOI: `10.3390/s18071981` (cit. on pp. 81, 82).

[96]   F. Ciampa et al. "Recent advances in active infrared thermography for non-destructive testing of aerospace components". In: *Sensors* 18.2 (2018). DOI: `10.3390/s18020609` (cit. on pp. 81, 83).

[97]   R. A. Lemons and C. F. Quate. "Acoustic microscope—scanning version". In: *Applied Physics Letters* 24.4 (1974), pp. 163–165. DOI: `10.1063/1.1655136` (cit. on p. 82).

[98] E. F. Fleet et al. "Hts scanning squid microscopy of active circuits". In: *IEEE Transactions on Applied Superconductivity* 9.2 (1999), pp. 4103–4106. DOI: `10.1109/77.783928` (cit. on p. 82).

[99] D. P. Vallett. "A comparison of lock-in thermography and magnetic current imaging for localizing buried short-circuits". In: vol. ISTFA 2011: Conference Proceedings from the 37th International Symposium for Testing and Failure Analysis. Nov. 2011, pp. 146–152. DOI: `10.31399/asm.cp.istfa2011p0146` (cit. on p. 82).

[100] E. Marchiori et al. *Technical Review: Imaging weak magnetic field patterns on the nanometer-scale and its application to 2D materials*. 2021. arXiv: `2103.10382 [cond-mat.mes-hall]` (cit. on p. 82).

[101] R. Weigel et al. "Microwave acoustic materials, devices, and applications". In: *IEEE Transactions on Microwave Theory and Techniques* 50.3 (2002), pp. 738–749. DOI: `10.1109/22.989958` (cit. on p. 82).

[102] X. Fang et al. "Research progress of automated visual surface defect detection for industrial metal planar materials". In: *Sensors* 20.18 (2020). DOI: `10.3390/s20185136` (cit. on p. 82).

[103] X. Maldague. *Theory and Practice of Infrared Technology for Nondestructive Testing*. Series in Microwave and Optical Engineering. Wiley, 2001. ISBN: 9780471181903 (cit. on p. 82).

[104] V. Vavilov and D. Burleigh. *Infrared Thermography and Thermal Nondestructive Testing*. Springer International Publishing, 2020. ISBN: 9783030480028 (cit. on p. 82).

[105] Marin E. "On thermal waves". In: *European Journal of Physics* 34.5 (2013), pp. L83–L85. DOI: `10.1088/0143-0807/34/5/l83` (cit. on p. 82).

[106] O. Breitenstein, W. Warta, and M. C. Schubert. *Lock-in Thermography: Basics and Use for Evaluating Electronic Devices and Materials*. 3rd ed. Springer Series in Advanced Microelectronics. Springer International Publishing, 2018. ISBN: 978-3-319-99825-1 (cit. on p. 82).

[107] V. P. Vavilov and D. D. Burleigh. "Review of pulsed thermal ndt: physical principles, theory and data processing". In: *NDT & E International* 73 (2015), pp. 28–52. DOI: `10.1016/j.ndteint.2015.03.003` (cit. on p. 83).

[108] C. Ibarra-Castanedo et al. "Discrete signal transforms as a tool for processing and analyzing pulsed thermographic data". In: vol. 6205. International Society for Optics and Photonics. SPIE, 2006, pp. 359–370. DOI: `10.1117/12.660226` (cit. on p. 83).

[109] C. H. Chen. *Ultrasonic and advanced methods for nondestructive testing and material characterization*. World Scientific, 2007. DOI: `10.1142/6327` (cit. on p. 83).

[110]   R. Marani et al. "Enhancing defects characterization in pulsed ther-
        mography by noise reduction". In: *NDT & E International* 102 (2019),
        pp. 226–233. DOI: `10.1016/j.ndteint.2018.12.009` (cit. on p. 84).

[111]   R. Smallwood et al. "Tomographic imaging and scanning thermal
        microscopy: thermal impedance tomography". In: *Thermochimica Acta*
        385.1 (2002), pp. 19–32. DOI: `10.1016/S0040-6031(01)00705-5`
        (cit. on p. 87).

[112]   P. Dahlberg et al. "Design and construction of an led-based excitation
        source for lock-in thermography". In: *Applied Sciences* 12.6 (2022). DOI:
        `10.3390/app12062940` (cit. on p. 116).

[113]   M. Ziegler, E. Thiel, and S. Ahmadi. "Lock-in thermography using high-
        power laser sources". In: *12th European Conference on Non-Destructive
        Testing (ECNDT 2018)*. 2018 (cit. on p. 116).

[114]   E. Thiel, M. Ziegler, and T. Studemund. "Localization of subsurface
        defects in uncoated aluminum with structured heating using high-power
        VCSEL laser arrays". In: *International Journal of Thermophysics* 40.17
        (2019). DOI: `https://doi.org/10.1007/s10765-018-2478-9`
        (cit. on p. 116).

Personal publication record

Here, an exhaustive list of all publications by the author is given. This includes journal articles, conference proceedings, and patents, which are authored or coauthored by Nils J. Ziegeler, sorted by publication date.

Patents

[1] P. W. Nolte, N. J. Ziegeler, and S. Schweizer. "Verfahren zur Bestimmung der ortsaufgelösten thermischen Strukturfunktion und/oder Zeitkonstantenspektren eines Objekts". Deutsches Patent- und Markenamt Patentschrift DE 10 2019 214 472 B3. Fachhochschule Südwestfalen and Fraunhofer-Gesellschaft zur Förderung der angewandten Forschung e.V. Dec. 17, 2020.

Journal articles and conference proceedings

[1] P. W. Nolte et al. "Suitability of lock-in infrared thermography for luminescent glass development". In: *14th Quantitative InfraRed Thermography Conference*. 2018. DOI: 10.21611/qirt.2018.134.

[2] P. W. Nolte, N. J. Ziegeler, and S. Schweizer. "Temperature profiling of secondary led optics by infrared thermography". In: *LED professional Review* 75 (2019), pp. 38–42.

[3] N. J. Ziegeler, P. W. Nolte, and S. Schweizer. "Application of infrared thermography to thermal transient measurements". In: *25th International Workshop on Thermal Investigations of ICs and Systems (THERMINIC)*. 2019, pp. 1–4. DOI: 10.1109/THERMINIC.2019.8923882.

[4] P. W. Nolte, N. J. Ziegeler, and S. Schweizer. "Transient infrared thermography for thermal conduction path analysis of led modules". In: *LED professional Review* 81 (2020), pp. 64–67.

[5] N. J. Ziegeler, P. W. Nolte, and S. Schweizer. "Transient thermographic heat path analysis using spatially resolved thermal equivalent networks". In: *15th Quantitative InfraRed Thermography Conference*. 2020. DOI: 10.21611/qirt.2020.037.

[6] N. J. Ziegeler, P. W. Nolte, and S. Schweizer. "Thermal equivalence networks for analysis of transient thermographic data". In: *26th International Workshop on Thermal Investigations of ICs and Systems (THERMINIC)*. 2020, pp. 226–231. DOI: 10.1109/THERMINIC49743.2020.9420520.

[7] P. W. Nolte et al. "Suitability of lock-in infrared thermography for luminescent glass development". In: *Quantitative InfraRed Thermography Journal* 17.2 (2020), pp. 96–106. DOI: 10.1080/17686733.2019.1646448.

[8] P. W. Nolte, N. J. Ziegeler, and S. Schweizer. "Analysis of heat paths in led retrofit lamps". In: *LED professional Review* 82 (2020), pp. 54–57.

[9] N. J. Ziegeler, P. W. Nolte, and S. Schweizer. "Optimization-based network identification for thermal transient measurements on LEDs". In: *27th International Workshop on Thermal Investigations of ICs and Systems (THERMINIC)*. 2021, pp. 23–30. DOI: 10.1109/THERMINIC52472.2021.9626491.

[10] N. J. Ziegeler, P. W. Nolte, and S. Schweizer. "Quantitative performance comparison of thermal structure function computations". In: *Energies* 14.21 (2021). DOI: 10.3390/en14217068.

[11] N. J. Ziegeler, P. W. Nolte, and S. Schweizer. "Optimization-based network identification for thermal transient measurements". In: *Energies* 14.22 (2021). DOI: 10.3390/en14227648.

[12] N. J. Ziegeler, P. W. Nolte, and S. Schweizer. "Thermographic network identification for transient thermal heat path analysis". In: *Quantitative InfraRed Thermography Journal* (2022). DOI: 10.1080/17686733.2022.2033529.

[13] P. Dahlberg et al. "Design and construction of an led-based excitation source for lock-in thermography". In: *Applied Sciences* 12.6 (2022). DOI: 10.3390/app12062940.

Erklärungen gemäß §7 der Promotionsordnung vom 6. August 2020

Ich erkläre,

1. dass mir die Promotionsordnung vom 6. August 2020 bekannt ist und von mir anerkannt wird.

2. dass ich weder früher noch gleichzeitig bei einer anderen Hochschule oder in einer anderen Fakultät ein Promotionsverfahren beantragt habe.

3. hiermit an Eides statt, dass ich die vorliegende Arbeit ohne unzulässige Hilfe Dritter und ohne Benutzung anderer, nicht angegebener Hilfsmittel angefertigt habe. Die aus anderen Quellen direkt oder indirekt übernommenen Daten und Konzepte sind unter Angabe der Quelle gekennzeichnet.

   Die Arbeit wurde bisher weder im In- noch im Ausland in gleicher oder ähnlicher Form einer anderen Prüfungsbehörde vorgelegt.

   Es wurden keine Dienste eines Promotionsvermittlers oder einer ähnlichen Organisation in Anspruch genommen.

4. dass zu den vorgeschlagenen Mitgliedern der Promotionskommission keine verwandtschaftlichen Beziehungen, keine Verwandtschaft ersten Grades, Ehe, Lebenspartnerschaft oder eheähnliche Gemeinschaft besteht.

5. dass in meiner Dissertation Forschungsergebnisse verwendet worden sind, die in Zusammenarbeit mit den folgenden Wissenschaftlern gewonnen wurden:

   a) Dr. Peter W. Nolte, Fraunhofer-Anwendungszentrum für Anorganische Leuchtstoffe, Lübecker Ring 2, 59494 Soest, Deutschland,

   b) Prof. Dr. Stefan Schweizer, Fachhochschule Südwestfalen, Lübecker Ring 2, 59494 Soest, Deutschland.

Soest, den 24. August 2022

Nils Jonas Ziegeler